PRIMER

Raman microspectroscopy for microbiology

Kang Soo Lee[1,10]✉, Zachary Landry[1,10], Fátima C. Pereira[2], Michael Wagner[2,3], David Berry[2], Wei E. Huang[4], Gordon T. Taylor[5], Janina Kneipp[6], Juergen Popp[7,8], Meng Zhang[9], Ji-Xin Cheng[9] and Roman Stocker[1]✉

Abstract | Raman microspectroscopy offers microbiologists a rapid and non-destructive technique to assess the chemical composition of individual live microorganisms in near real time. In this Primer, we outline the methodology and potential for its application to microbiology. We describe the technical aspects of Raman analyses and practical approaches to apply this method to microbiological questions. We discuss recent and potential future applications to determine the composition and distribution of microbial metabolites down to subcellular scale; to investigate the host–microorganism, cell–cell and cell–environment molecular exchanges that underlie the structure of microbial ecosystems from the ocean to the human gut microbiomes; and to interrogate the microbial diversity of functional roles in environmental and industrial processes — key themes in modern microbiology. We describe the current technical limitations of Raman microspectroscopy for investigation of microorganisms and approaches to minimize or address them. Recent technological innovations in Raman microspectroscopy will further reinforce the power and capacity of this method for broader adoptions in microbiology, allowing microbiologists to deepen their understanding of the microbial ecology of complex communities at nearly any scale of interest.

Fourier transform infrared (FTIR) spectroscopy
The other prominent method of vibrational spectroscopy, whereby absorption of light by a sample is used to identify the molecular composition of the sample.

Raman microspectroscopy is a form of vibrational spectroscopy that harnesses the inelastic scattering of light, whereby the difference in wavelength between excitation and emission upon interaction with the sample is determined by molecular vibration. This shift in wavelength provides information about the molecular bonds present, and thus the chemical composition of the sample. Since the first experimental observation of this scattering by C. V. Raman in 1928 (REF.[1]), Raman technology has been widely adopted in materials science and engineering and is seeing growing applications in microbiology and microbial ecology. Raman microspectroscopy represents a potentially game-changing technology for our understanding of the diversity of metabolites and molecular interactions underlying microbial ecology. Recent advances now enable in situ interrogation of the chemistry of living microorganisms at sub-micrometre resolution. The technique is non-destructive, requires no sample preparation and the measurement is simple and rapid, on the order of a few seconds per measurement. The door is thus open to applications in microbiology for spatiotemporal probing of a sample at single-cell scale (for typical micrometre-sized bacteria) or even subcellular scale (for larger eukaryotic cells such as phytoplankton).

Raman technology is uniquely flexible compared with alternative methods with similar functionalities. For example, Fourier transform infrared (FTIR) spectroscopy suffers from strong absorption of infrared wavelengths by water, which hinders the use of the system to interrogate microbial cells in situ[2,3]. Nanoscale secondary ion mass spectrometry (nanoSIMS) and cryogenic electron microscopy (cryo-EM) complemented with energy dispersive X-ray spectroscopy (EDS) enable much higher sensitivity and spatial resolution than Raman microspectroscopy — down to a few tens of nanometres — but require vacuum conditions and/or cryogenic temperatures for operation, making live cell imaging impossible[4–9]. Both approaches provide information on the elemental (and isotopic, in the case of nanoSIMS) composition and structure of a sample and not on its molecular composition. For example, the amount of ^{13}C compounds in a sample can be measured with nanoSIMS, yet their distribution among molecules as part of lipids and storage compounds cannot be determined. The ability of Raman systems to interrogate the chemistry of individual cells provides microbiologists with a means to rapidly investigate the ecophysiology of individual live microorganisms, offering, for example, an opportunity to uncover the metabolic roles and contributions of microorganisms within complex communities

✉e-mail: *leeka@ethz.ch; romanstocker@ethz.ch*

https://doi.org/10.1038/s43586-021-00075-6

Author addresses

[1]Institute of Environmental Engineering, Department of Civil, Environmental and Geomatic Engineering, ETH Zurich, Zurich, Switzerland.
[2]Division of Microbial Ecology, Department of Microbiology and Ecosystem Science, Centre for Microbiology and Environmental Systems Science, University of Vienna, Vienna, Austria.
[3]Department of Chemistry and Bioscience, Aalborg University, Aalborg, Denmark.
[4]Department of Engineering Science, University of Oxford, Oxford, UK.
[5]School of Marine and Atmospheric Sciences, Stony Brook University, Stony Brook, NY, USA.
[6]Department of Chemistry, Humboldt-Universität zu Berlin, Berlin, Germany.
[7]Institute of Physical Chemistry and Abbe Center of Photonics (ACP), Friedrich Schiller University Jena, Jena, Germany.
[8]Leibniz Institute of Photonics Technology e.V. Jena and Leibniz Health Technology, Jena, Germany.
[9]Department of Electrical and Computer Engineering & Department of Biomedical Engineering, Boston University, Boston, MA, USA.
[10]These authors contributed equally: Kang Soo Lee, Zachary Landry.

and to track metabolic exchange between microbial symbionts. For instance, monitoring of carotenoids in autotrophic microalgae enables investigation of the photophysiology under ecologically relevant conditions, such as through the diel cycle or under deficiency of inorganic nutrients such as nitrogen, phosphorus or silica[10–17]. Measuring ^{13}C transfer from a host to associated microorganisms (and vice versa) provides a means to interrogate the currency of carbon exchange between the partners[18]. Despite this potential, Raman microspectroscopy is still underused in microbiology.

This Primer aims to provide an overview of Raman technology and its potential applications for microbiologists and bioengineers. We describe the fundamental principle and the advanced technical add-ons of Raman microspectroscopy. Normal and resonance Raman microspectroscopy are the two simplest modes of Raman microspectroscopy and are the main focus in this Primer, although we also briefly discuss extended methods such as surface-enhanced Raman spectroscopy (SERS), hyper-Raman scattering (HRS) and coherent Raman spectroscopy/microscopy. We outline criteria to optimize experimental parameters and strategies to analyse the multivariate data that Raman microspectroscopy provides, to extract accurate chemometric information about the sample. We review applications in microbiology, which is currently maturing from examples in laboratory model systems to the analysis of natural samples. Given that most microorganisms on Earth are still not cultivable, we then provide a roadmap for applying Raman technologies more widely to understand the microbial ecology of complex communities in diverse real-world environments, such as freshwater and oceans, soil, air and host-associated intestinal microbiomes. We discuss the current technical limitations of Raman microspectroscopy for investigations of microorganisms and ways to minimize and address these limitations. Finally, we outline possibilities to reinforce the power and capacity of Raman microspectroscopy and to adopt the technique in underused fields in microbiology.

Normal Raman microspectroscopy
A fundamental form of Raman microspectroscopy that relies on measurement of non-resonant, spontaneous scattering signals in which one out of ~10^6 incoming photons to a sample is scattered.

Wavenumber
A unit of frequency used in vibrational spectroscopy, defined as the frequency divided by the speed of the wave and thus equal to the number of waves within one centimetre.

Resonance Raman scattering
Raman scattering that arises when the wavelength of the incident laser beam matches the electronic transitions of a molecule, which generates much more intense Raman signals than normal Raman scattering.

Experimentation

Raman working principles

When a molecule encounters incident monochromatic light such as that from a coherent laser beam, it emits light as a result of elastic scattering — known as Rayleigh scattering, where no wavelength shift occurs after the interaction — and inelastic scattering — composed of Stokes and anti-Stokes Raman scattering, where the emitted light has longer and shorter wavelengths, respectively, than the incident light (FIG. 1a). These elastic and inelastic types of scattering are the result of excitation of the molecules to virtual states and then a return to lower energy states with subsequent light emission (FIG. 1c). Normal Raman microspectroscopy, the most fundamental Raman system, usually relies on Stokes Raman scattering. The magnitude of the shift in wavelength depends on the molecular vibrational state, thus measuring the light emitted by a sample after excitation provides a means to identify the molecular bonds present and hence the molecular composition of a sample. For example, C–C bonds, the CH_2 group and C double bonds with C or O induce shifts in wavenumber of 1,127, 1,304 and 1,665 cm^{-1}, respectively (FIG. 1b). When the wavelength of the incident laser beam matches the electronic transitions of a molecule, the generated Raman signals are much greater (by a factor of ~10^3) than those from normal Raman microspectroscopy, an effect known as resonance Raman scattering (FIG. 1c). This is distinct from the fluorescence resulting from absorption; fluorescence lifetimes (longer than nanoseconds) are much longer than in Raman scattering (on the order of picoseconds).

Variant Raman systems

There have been various advances in Raman technology, particularly technical breakthroughs that address the limited sensitivity of normal Raman microspectroscopy. Technological advances include, for example, UV and deep-UV resonance Raman spectroscopy, SERS, HRS and coherent Raman scattering microscopy (CRSM). These advances have fostered the adoption of Raman approaches in microbiology and below we briefly describe the underlying working mechanisms, strengths and important features of these technologies. There are also many additional variant systems (such as tip-enhanced Raman spectroscopy[19,20] and spatially offset Raman spectroscopy[21]), for which applications in microbiology have not yet been demonstrated.

UV and deep-UV resonance Raman spectroscopy. A Raman laser with UV or deep-UV wavelengths (down to 200 nm) provides a means to interrogate known metabolites of microorganisms with high sensitivity by virtue of resonance Raman scattering, which does not occur in the visible or infrared wavelength range[22]. Additionally, the use of a short wavelength laser further improves the sensitivity; Raman intensity is inversely proportional to the laser wavelength to the power of four. Short wavelengths also improve diffraction-limited resolution — the spatial resolution is proportional to the laser wavelength — reinforcing the capability of subcellular Raman imaging of small bacterial cells. Despite these advantages[23–27], careful consideration is required before adopting this technique for specific applications in which non-destructive sampling is essential, as this wavelength region has a higher potential risk of laser-induced photo-damage owing to the resonance of the excitation laser with important cellular building blocks[28].

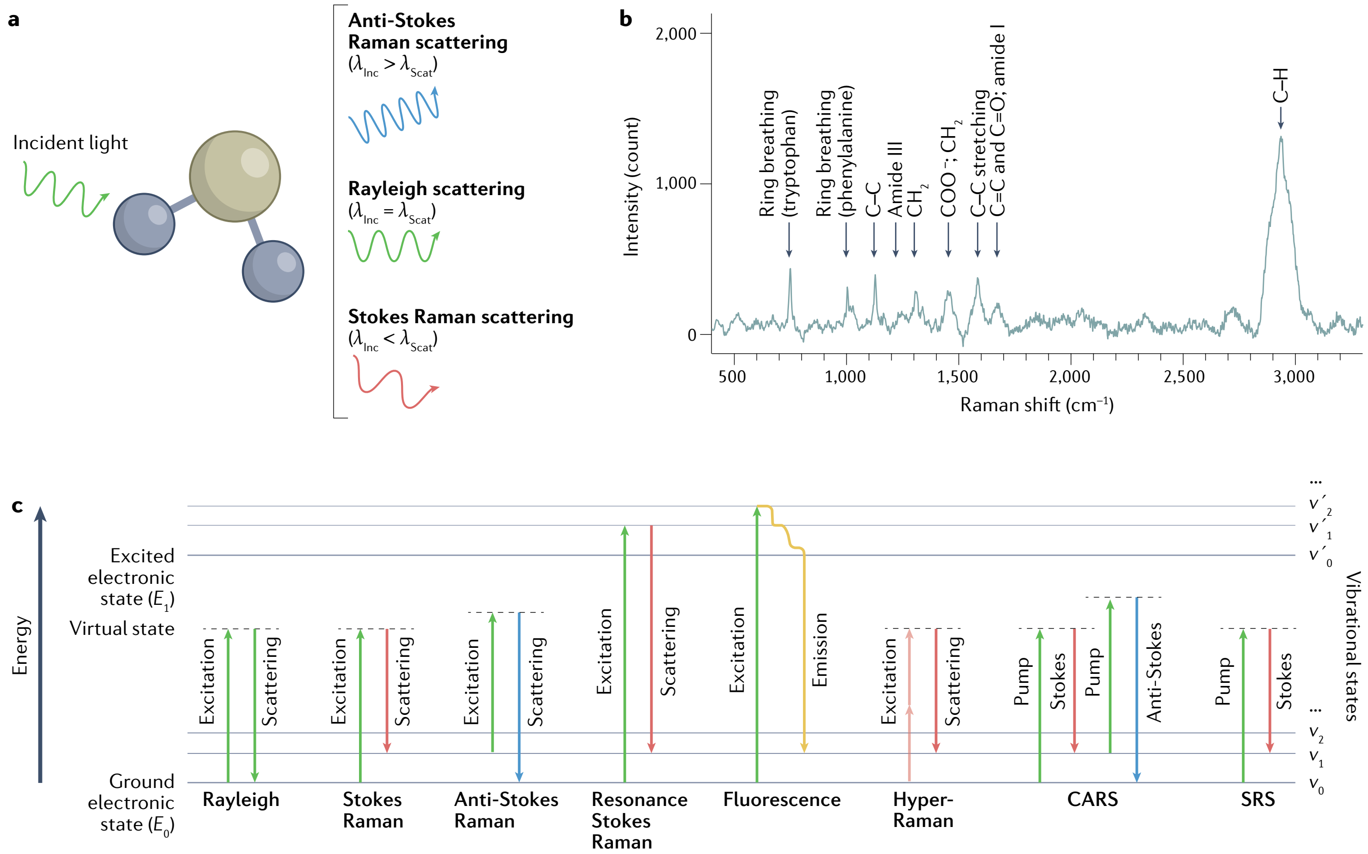

Fig. 1 | **Raman spectroscopy working principles. a** | Three types of scattering signal that are generated as a result of interactions between light and a molecule. Rayleigh scattering does not change the wavelength of the scattered light, relative to the incident light. For Raman scattering, the wavelength of the scattered light is longer (Stokes) or shorter (anti-Stokes) than the incident light. **b** | A processed Raman spectrum of a single bacterium (*Vibrio alginolyticus*). The molecular composition of the cell can be identified from the individual peaks at different wavenumbers (indicated as Raman shift) that correspond to different molecular bonds. **c** | Energy level diagrams representing the generation of emission signals. Colours of the arrows represent the wavelength. For Rayleigh and Raman (Stokes and anti-Stokes) scattering, the molecule is excited to a virtual energy state and then returns to a lower energy level, accompanied by light scattering. In contrast, for resonance Raman scattering and fluorescence emission, the molecule undergoes a transition to a higher electronic state, generating a much stronger emission signal. Hyper-Raman scattering relies on a nonlinear two-photon process. Coherent Raman scattering (CRS, including coherent anti-Stokes scattering (CARS) and stimulated Raman scattering (SRS)) is another type of nonlinear optical process based on the interaction between pump and Stokes lasers.

Surface-enhanced Raman spectroscopy. One can obtain Raman measurements with greatly improved sensitivity and selectivity by virtue of SERS (further details can be found in REFS[29,30]), by bringing the microorganism or molecule of interest into the vicinity of metallic nanoparticle substrates — typically gold or silver with the size of a few tens of nanometres.

Several approaches can be considered when applying SERS to the investigation of microorganisms. First, a plasmonic nanostructure can be designed and used as a SERS substrate. Physical contact or close proximity of the SERS substrate with a cell enables measurement of the molecular composition of the cell itself or of compounds that are secreted from the cell, respectively[31,32] (BOX 1). In the past two decades, several types of such SERS substrates have become commercially available, for example, from Horiba Scientific, SERSitive and many others. Second, metallic nanoparticles can be applied to directly coat the cell surface or infiltrate across the bacterial cell envelope[33–38]. Finally, a SERS tag can be employed when aiming to identify cells with specific phenotypes or genotypes[39]. In one such approach, SERS tags consist of a metallic nanoparticle coated by a Raman reporter and then a layer of polyethylene glycol (PEG) or silica, which protects the Raman reporter layer from surrounding stresses[39]. The PEG or silica layer can be functionalized with antibodies or aptamers that bind to specific microorganisms of interest. In comparison with other SERS approaches, the use of SERS tags is not limited by the need to achieve extremely close proximity of the nanoparticle surface to a cell of interest, but it benefits from an optimized, efficient SERS enhancement: the SERS signals arise from the Raman reporter engineered to be close to the nanoparticle, not from the cell itself.

Hyper-Raman scattering. HRS relies on a nonlinear optical process (FIG. 1c; further details can be found in REF.[40]). A mode-locked laser with a near-infrared wavelength generates HRS signals at visible wavelengths as if the excitation wavelength was half of the de facto excitation wavelength — analogous to other two-photon processes, such as two-photon excited fluorescence[41]. The generation of HRS signals depends on different

Raman reporter
A chemical that generates a known surface-enhanced Raman scattering signal.

Mode-locked laser
A laser that produces ultrashort pulses on the picosecond or femtosecond scale.

Box 1 | Underlying mechanisms for SERS

Surface-enhanced Raman spectroscopy (SERS) relies on electromagnetic and chemical enhancements, increasing Raman signal intensities by up to 10^8–10^{14} orders of magnitude[29]. The former arises from localized surface plasmon resonance (LSPR). When metallic nanoparticles are excited by a laser used to generate Raman scattering, their electrons perform collective oscillations, inducing a dipole in the individual nanoparticles. The field of this induced dipole causes strong enhancement of the electromagnetic field of the excitation, thereby intensifying Raman signals generated from the molecules in this field[232,233]. This electromagnetic enhancement peaks at the nanoparticle surface and exponentially decays with distance r — proportional to r^{-12} (REF.[233]). Care should be taken when applying SERS for the interrogation of microorganisms because the electromagnetic enhancement effect is confined to the proximity of the metallic nanoparticles, leading to potential issues, for example, limited reproducibility arising from variation dependent upon the orientation of the sampled microorganism with respect to the SERS substrate[234]. Additionally, the SERS signal of microorganisms is strongly influenced by the secretion of compounds such as nucleotides or degradation products upon starvation and osmotic stress[37,38].

Chemical enhancement of the signal arises from physico-chemical interaction between molecules and the metallic nanoparticles. The generated Raman signal is intensified when the wavelength of the laser illumination is resonant, for example, with the charge transfer states between the metal and the molecules. This effect occurs only when there is a very short distance between the metal and molecules.

The laser wavelength providing SERS functionality depends on the metallic nanoparticles used. Gold and silver nanoparticles generate SERS effects for 570–1,230 nm and 400–1,000 nm lasers, respectively[235]. The size of the metallic nanoparticles determines the optimal wavelength that generates maximum SERS enhancement. The illustration below show that the electric field intensity can be enhanced in the presence of gold nanoparticles with a size of 32 nm ($|E|^2/|E_0|^2$, where E and E_0 are the electric fields in the presence and absence of gold nanoparticles, respectively) and that the enhancement of the electric field intensity in the vicinity of gold nanoparticles is one to two orders of magnitude greater with the excitation of a 1,064 nm laser than with a 580 nm laser.

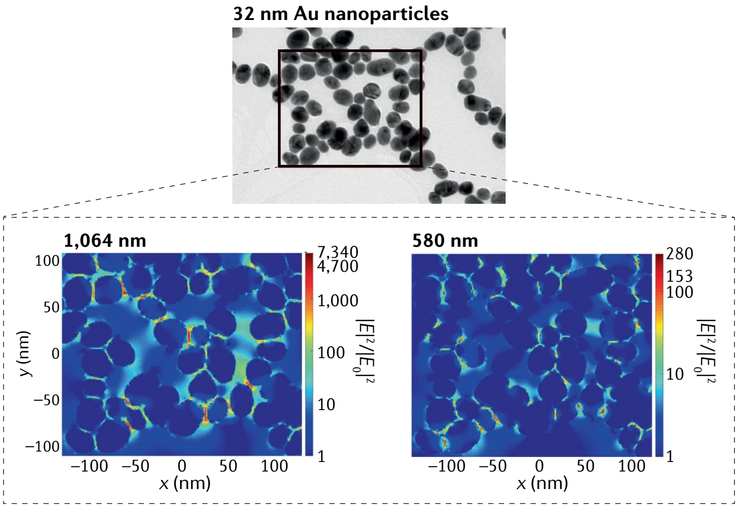

Reprinted with permission from REF.[236], American Chemical Society.

selection rules from other Raman scattering based on one-photon processes, providing complementary molecular information about a sample. For instance, HRS signals can reveal vibrations of molecules that are invisible to other Raman systems. The signal intensity in HRS scattering is not high, and so sensitivity is boosted by combining HRS with other techniques such as SERS (known as surface-enhanced hyper-Raman scattering; SEHRS[42–44]) or two-photon resonance with an electronic transition in a molecule (known as resonance HRS[40]).

Coherent Raman scattering microscopy. CRSM provides the capability of rapid molecular imaging (on the order of ~1 s for 200 × 200 pixels) at a selected wavenumber by virtue of 1,000-fold higher sensitivity than normal Raman scattering (further details can be found in REFS[45,46]). It relies on nonlinear optical processes that arise from the interaction between two lasers: pump and Stokes lasers with frequency ω_p and ω_S, respectively[45–49]. Coherent anti-Stokes scattering (CARS) and stimulated Raman scattering (SRS) result from this interaction. Briefly, CARS with a frequency $2\omega_p - \omega_S$ is generated when the frequency difference between the pump and Stokes laser ($\omega_p - \omega_S$) is resonant with a Raman-active molecular vibration in the sample (FIG. 1c). SRS is a dissipative process in which the photon energy at a beating frequency ($\omega_p - \omega_S$) is transferred from the pump laser photons to the Stokes laser photons and then to a molecule in the sample, causing vibrational excitation (FIG. 1c).

Coherent Raman scattering occurs at a specific wavenumber (at $2\omega_p - \omega_S$ for CARS and ω_p or ω_S for SRS) that can be adjusted by changing the wavelength of the pump laser (using a tuneable laser source), while the wavelength of the Stokes laser is fixed (usually in the infrared region; around 1,045 nm). It is a powerful and sensitive tool enabling selective vibrational imaging of microorganisms within a spatial region of interest with a resolution of ~350 nm, yet, unlike the other Raman systems described above, the conditions generating a signal are specific to a specific wavenumber and thus the technique does not lend itself to a comprehensive investigation of the molecular composition of a sample across a broad Raman spectral window. Recent innovations in the technology are addressing this issue, such as multicolour SRS[50–52], which can simultaneously image several wavenumber regions, and should lead to wider applications in microbiology.

System configuration

Raman systems for measurements of normal Raman scattering can be established on the basis of several essential components: components for bright-field imaging to search for a region of interest within a sample; a laser source to excite molecules within the sample to higher vibrational states; optical components, including an objective, mirrors, beam splitters and a Rayleigh filter, to deliver the laser beam onto the sample and the generated Raman signals back to the microspectroscope system, as well as to separate the polychromatic Raman signal by colour (known as diffraction grating); and a detector to measure Raman signals (FIG. 2a). Selection guidelines for technical components to optimize Raman measurements for specific applications are discussed in BOX 2. To use variant Raman systems, the system design must be adjusted accordingly. As an example, for UV or deep-UV Raman spectroscopy, the optical components must be UV compatible, while HRS requires a mode-locked laser source for the generation of the two-photon process, and CRSM needs a two-colour laser to create the coherence effect and a lock-in amplifier to detect SRS signals.

To operate a Raman system, an imaging camera (camera 1; FIG. 2a), a motorized *xyz* stage and transmitted illumination (for example, bright-field microscopy)

Selection rules
Constraints that govern the likelihood of whether undergoing particular quantum transitions from one state to another is allowed or forbidden.

Beating frequency
Frequency difference between two electromagnetic waves that interfere constructively and destructively.

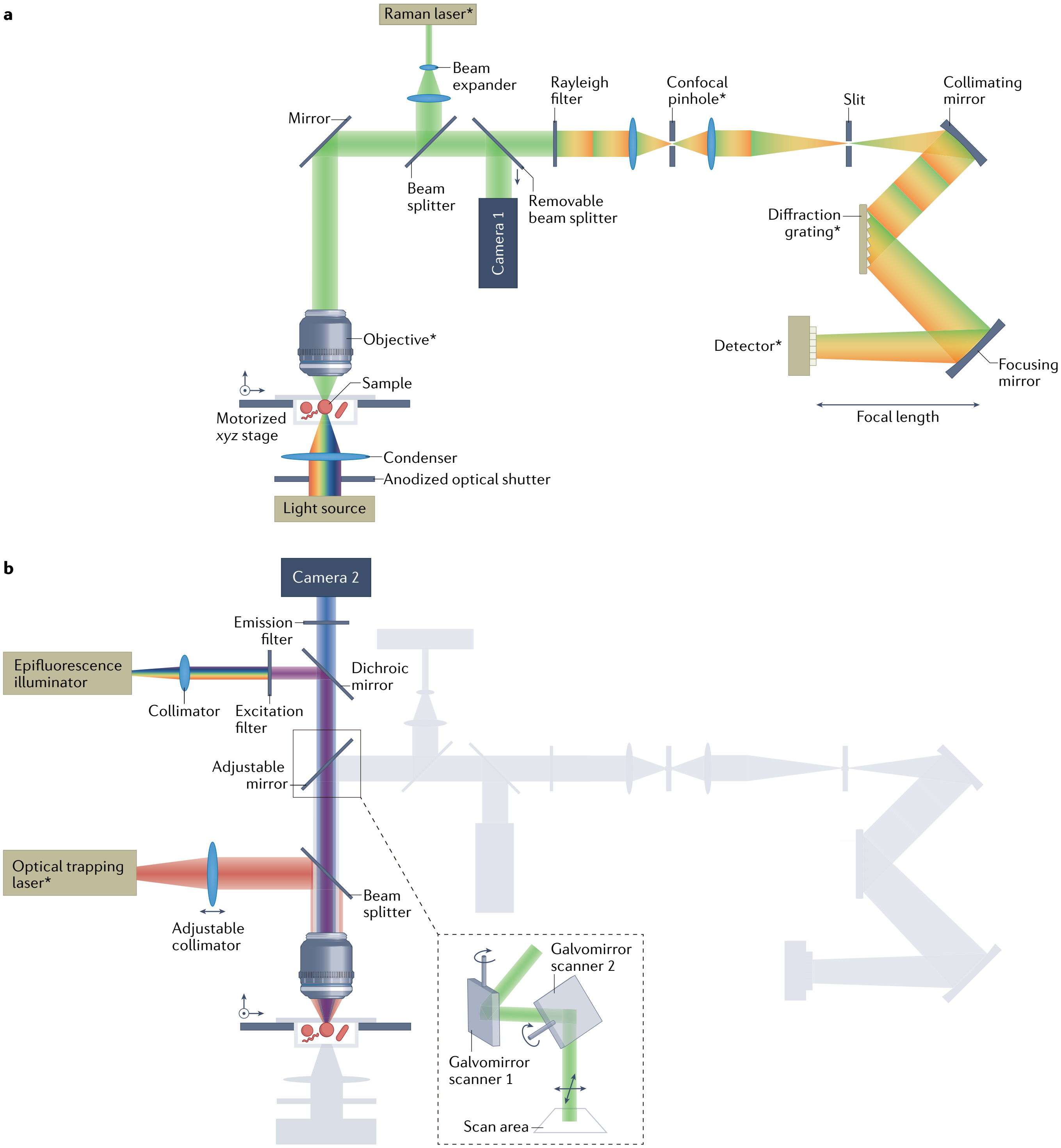

Fig. 2 | **Configuration of a Raman microspectroscopy system. a** | A fundamental Raman set-up consists of components for bright-field light microscopy to select a region of interest for Raman measurements (a light source, a motorized *xyz* stage, an objective and camera 1); a Raman laser to generate Raman signals from the sample (a beam expander is equipped to ensure that the laser beam completely fills the back aperture of the objective); optical components to deliver the generated Raman signals to the Raman system (beam splitters, mirrors, a Rayleigh filter, a confocal pinhole and a slit) and to divide the polychromatic Raman signal with respect to colour (a diffraction grating); and a detector to measure the Raman signal. The components marked with an asterisk (*) require optimization in the choice of hardware and operational parameters to optimize Raman measurement. **b** | Integration of set-ups for epifluorescence detection and optical tweezers for optical trapping that can complement Raman interrogation of microorganisms. Implementation of a set of galvomirrors enables rapid area scanning for the Raman measurement. The components described in part **a** are shown in grey.

Box 2 | Optimization of technical components

Optimization of technical parameters is required to obtain a Raman signal of sufficient intensity to allow reliable and precise measurement. Here, we outline six important aspects to be considered in the set-up of the hardware and the operation of a Raman system. For more detailed information on these, see Supplementary Note 1.

Microscope

Upright or inverted microscopes can be considered depending on the application. Hardware for additional functionalities, such as phase contrast or differential interference contrast microscopy, is compatible with Raman measurement, yet specific optical components for those systems, such as a phase ring at the rear focal plane of an objective, could reduce Raman signals.

Confocality

Specifications of the objective and its combination with a confocal set-up within the Raman system must be chosen so that the interrogation volume is appropriate for the size of the microorganisms of interest. General recommendations are difficult to provide; instead, the confocality should be assessed experimentally.

Detector

An appropriate detector must be chosen on the basis of its quantum efficiency. In general, front-illuminated charge-coupled device (CCD) detectors provide a good price–performance ratio, whereas back-illuminated CCD detectors can be considered for measurements requiring higher sensitivity.

Laser

The wavelength of the laser has a considerable impact on the generated Raman signals. The shorter the wavelength used, the stronger the generated Raman, but also the higher the likelihood of generating fluorescence signals that interfere with measurement of the Raman signals. Given this trade-off, 532 nm is recommended as a starting point.

Substrate

Raman signals from the substrate holding the sample are usually of comparable or higher intensity than those from the sample. Glass slides or coverslips can be used as a starting point for measurements of novel samples. If a substrate with less background in the spectral region of interest is required, another material such as aluminium, calcium fluoride or quartz can be used.

Diffraction grating

A key component in the determination of the spectral resolution of the measured Raman spectra. A grating that can measure a phenylalanine peak at 1,007 cm^{-1}, the sharpest of the peaks among biologically important compounds, can be considered as a default set-up. The higher the grating number, the greater the spectral resolution but the lower the diffraction efficiency.

are first used to search for a spot of interest within a sample and focus an excitation laser onto this spot. The camera is then deactivated by removing a beam splitter during measurement to maximize the collection of generated Raman signals. The transmitted illumination is also inactive during this step to avoid interference with the measurements. In particular, if a light-emitting diode (LED) is used for illumination, an anodized optical shutter should be installed to prevent the Raman laser from travelling through the sample and generating a signal from the LED unit. It is also important to note that the focal plane selected on the basis of visual inspection using camera 1 is usually not identical to that of the Raman laser owing to chromatic aberration. The magnitude of this discrepancy depends on the specifications of the objective. Before measurements of many samples are acquired, a depth profiling in the *z* direction is performed to determine the magnitude of the offset between the two foci for the particular objective used — the position that provides maximum Raman intensities can be considered as the focus of the Raman laser. When performing measurements, the microscope stage should be moved in the *z* direction by the distance of this offset after finding a spot of interest for Raman measurement using bright-field microscopy.

During measurement, the width of the Raman laser beam is expanded using a beam expander to completely fill the back aperture of the objective. The laser is delivered onto the sample, and all backscattered light is collected by the objective and returned to the spectrograph. A Rayleigh filter rejects Rayleigh scattered signals, and the Raman signals generated from out of focus in the *z* direction are blocked by a confocal set-up. Either a notch filter or an edge-pass filter can be used as the Rayleigh filter. We recommend using an edge-pass filter — specifically, a long-pass or short-pass filter for the measurement of Stokes or anti-Stokes Raman scattering, respectively — considering its nearly infinite lifespan. Although a notch filter removes only the Rayleigh scattering and thus both Stokes and anti-Stokes signals can be measured, it has a finite lifetime. In practice, an edge-pass filter often produces wavy backgrounds — a non-zero baseline that is not flat across the spectrum. Measured data should be corrected to separate molecular information about the sample from these backgrounds[53]. To this end, a calibration halogen lamp that generates a known Raman spectrum is used (such as ICS correction using the halogen lamp for instruments from Horiba Scientific).

Raman signals then pass through a slit and are collimated using a collimating mirror. A diffraction grating separates the polychromatic scattered signals according to wavelength along the major axis of the charge-coupled device (CCD) module arrays of a detector — module arrays arranged as a rectangle are usually used for the Raman detector. Each CCD pixel measures the individual signals at a different range of wavelengths. System calibration with respect to the strong Raman peak of a commercial silicon wafer at 520.5 cm^{-1} (REF.[54]) is recommended every 24 h or before every experiment, since Raman measurements are influenced by environmental conditions such as temperature.

For spatiotemporal interrogation of samples, two technical options can be considered: point measurement or raster mapping of area or volume. In point measurement, Raman signals are acquired from a single point at the focus of the Raman laser, such as from a single bacterium. Typically, a point measurement with a high-power objective will have a resolution down to 0.3 μm, depending on laser wavelength. The diffraction-limited spatial resolution is given by $1.22\lambda/\mathrm{NA}$, where λ and NA denote the laser wavelength and numerical aperture of the objective, respectively. Raster mapping is possible through movement of the motorized *xyz* stage, allowing interrogation of a discretized array of points within an area or volume. This approach would allow, for example, the measurement of a region of a biofilm matrix[55,56] or a large microbial cell[57]. To improve the flexibility of area or volume measurements, a pair of scanning galvomirrors (one for the *x* axis and the other for the *y* axis) can be implemented in the position of the adjustable mirror (FIG. 2b). In comparison with point measurement, rapid area scanning provides a means to obtain comprehensive chemical information from a sample that is larger than the spot size of the Raman laser beam.

Spectral window
A spectral region of interest.

Diffraction grating
A glass plate etched with very close parallel lines that produces a spectrum from a coherent light beam by diffraction and interference of light and thus functions as a planar prism.

Chromatic aberration
Discrepancy of focus in axial and transverse directions between rays with different wavelengths after a focusing lens owing to the discordance of their refraction angles.

Galvomirrors
A pair of mirrors, each of which is integrated with a rapidly moving scanning motor, which enables enlargement of a laser beam spot to a small scanning area.

Dichroic mirror
An optical component for fluorescence microscopy by which monochromatic light for the excitation of fluorophores in a sample is separated from generated fluorescence signals.

Integration with other optical systems

A Raman system can be easily integrated with other optical components, thereby providing a means to enhance the reliability and flexibility of Raman measurements and to obtain complementary information (FIG. 2b). For example, optical tweezers[58–60] can be implemented to allow precise and reliable Raman measurement of small microbial cells by immobilizing a cell within the interrogation volume during measurement[61]. Raman microspectroscopy is increasingly being used in combination with epifluorescence microscopy. For example, fluorescence signals are recorded to identify microorganisms of interest within a complex community using fluorescence in situ hybridization (FISH) (BOX 3) and Raman measurements are used to analyse their molecular composition[62]. For measurement of fluorescence signals, light of a specific wavelength is directed onto the sample through a dichroic mirror, and upon interaction with fluorophores within the sample, the generated fluorescence signals travel back through an edge-pass filter to a detector (camera 2). In general, Raman and fluorescence signals can be measured from the same sample using fluorophores that are not excited by the Raman laser[63] or via photobleaching techniques for fluorophores in which the excitation wavelength overlaps with that of the Raman laser[62]. Raman and fluorescence measurements must be taken one after another because the adjustable mirror needs to be withdrawn from the optical path to measure fluorescence signals.

Sample preparation

Samples can be measured in either dry or liquid form. To investigate time-dependent changes in the ecophysiology of microorganisms, one can measure samples of dry cells taken from the population at different time points, but the measurement of dry cells is destructive. To mitigate the risks of physiological changes of the cells before measurement, implementation of chemical fixation and inactivation can be considered. Sodium azide or formaldehyde is recommended over other common fixatives, such as glutaraldehyde or ethanol, which could induce changes in the overall spectral shape[64,65]. Storage of samples below −80°C before measurement can be considered as another option, but its efficacy has not yet been quantitatively analysed. Alternatively, the ecophysiology of individual cells can be tracked through time by measuring the same cells multiple times within a fluidic system engineered to enable patterning of individual cells within an interrogation chamber based on physical stamping of the cells on substrates or external force fields[66,67]. We recommend the use of dry cells for rapid measurements of cells with high sensitivity and cells in liquid for measurements of 'live' cells with high reproducibility. In general, the sensitivity is higher with measurements of dry cells owing to the absence of interference by Raman signals generated from a liquid medium. Additionally, procedures for the preparation and measurement of dry cells are straightforward; an example of these procedures can be found in REF.[68]. However, there is cell-to-cell variation in background noise in measurements of dry cells — even within the same strain. Thus, to allow quantitative comparison, data processing to remove this background is required (FIG. 3a).

Cells in liquid phase generate reproducible Raman signals by virtue of a consistent level of signals from the medium, although sensitivity can wane. Compared with measurements of dry cells, those in liquid phase combined with a cell sorting platform[61,63,69–72] provide an easier means to conduct downstream analyses such as sequencing or cultivation of taxa of interest. Use of a liquid medium provides a cooling effect, which mitigates the heating effect of the laser, and this cooling effect is more pronounced with fluid flow. Dry samples will be more susceptible to laser-induced photo-damage and thus require the use of lower laser power. Signs of damage include a change in colour to black due to combustion, physical disappearance of cells during measurement possibly owing to evaporation or cell lysis and abnormally high or saturated intensities in certain spectral regions, depending on the wavelength of the laser.

When using liquid phase measurements, the choice of a non-photoluminescent medium is important, as signals from the medium could mask cellular signals. Samples incubated in photoluminescent media such as Luria–Bertani medium should be resuspended in an isotonic medium that does not induce osmotic stress (for example, 0.2 M glycerol balanced by Milli-Q), as osmotic stress increases the risk of photo-damage[61,63] (FIG. 3b). Additionally, Raman signals from water should be considered during analysis[61,63]. Specifically, an H_2O symmetrical stretching peak at 1,665 cm^{-1} interferes with measurements of carbohydrate (C=C, C=O) and protein (amide I) signals (Supplementary Table 1) and an OH peak at 3,400 cm^{-1} coincides with strong lipid signals at 2,800–3,300 cm^{-1} (REF.[73]).

Stable isotope probing. In microbiology one often seeks to quantify metabolic activity, growth and chemical transfers from the environment to microbiota or between microorganisms. Incubation of a microbiota sample with isotopically labelled compounds — known as stable

Box 3 | Fluorescence in situ hybridization

Fluorescence in situ hybridization (FISH) with 16S or 23S ribosomal RNA-targeted oligonucleotide probes enables microbiologists to specifically stain microorganisms of interest in complex samples[237] and to quantify their abundance and ribosome content in environmental and medical samples[238]. The signal intensity of FISH reflects the ribosome content of the cells and is thus dependent on their activity. The detection of cells with low ribosome content can be achieved using catalysed reporter deposition (CARD)–FISH, which strongly enhances the FISH signal[239] but requires the application of a more time-consuming protocol.

Several different fluorophores have been used for FISH in microbial communities, allowing for the simultaneous detection of multiple taxa with different probes[240–242]. The combination of FISH and Raman microspectroscopy enables researchers to record Raman spectra of selected microorganisms of interest in a complex community in a targeted manner and has successfully been applied for stable isotope labelling experiments[70] or for the detection of storage compounds[129] in selected taxa. Ideally, for FISH–Raman, fluorophores should be selected that are not excited by the applied Raman laser, yet bleaching the dyes after their measurement provides an alternative[62,81].

It should be kept in mind that the fixation and permeabilization steps as well as the hybridization and wash steps of the FISH protocol can cause loss of biomolecules from the stained cells and thus decrease the Raman signal of storage compounds or lipids. The latter has been shown to slightly reduce the deuterium signal in FISH–Raman experiments after stable isotope probing with heavy water[71].

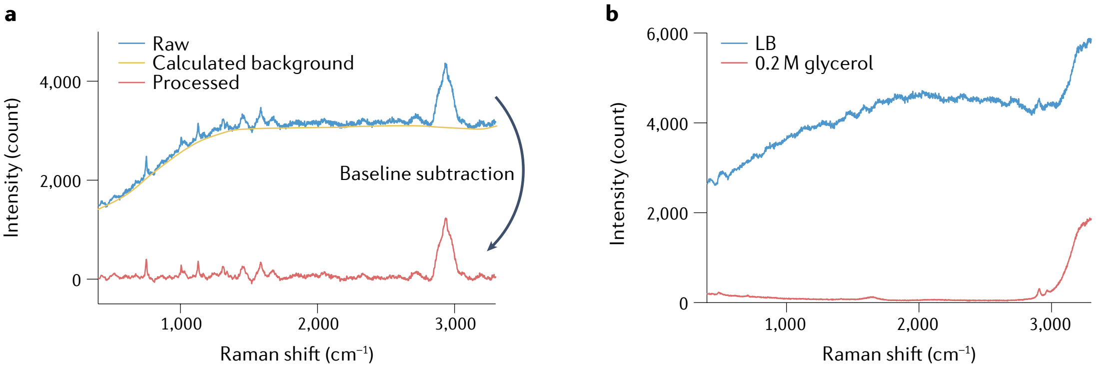

Fig. 3 | **Sample preparation. a** | Measurements of dry cells (*Vibrio alginolyticus*) on an aluminium-coated slide provide greater sensitivity over those in liquid owing to the absence of signals by the liquid medium, yet they usually require data processing to remove intrinsic backgrounds. **b** | For measurements of cells in liquid, use of a non-photoluminescent medium is important, as shown in the difference in intensity between Luria–Bertani (LB) medium and 0.2 M glycerol.

isotope probing (SIP) — coupled to Raman microspectroscopy can address a broad range of dynamical processes on a single-cell basis (reviewed in REF.[74]).

The energy of Raman-scattered photons is largely controlled by the mass of the atoms involved in the molecular vibration. A single additional neutron in an isotopically heavy tracer is sufficient to slow a molecular vibration and lower the frequency of Raman-scattered photons from that of a lighter isotopologue. This phenomenon is observed as a red shift in the position of the peak corresponding to the affected molecular bond. Principles behind spectral red shifts and factors affecting their magnitude are explored in Supplementary Note 2.

Selection of an optimal isotope tracer for an experiment is driven primarily by the biological question (BOX 4). Given that not all atoms in a substrate are necessarily assimilated into biomass, chances of reliable detection and quantification are enhanced with substrates that have a uniformly labelled tracer. In laboratory SIP experiments, media can be engineered such that the tracer is a single carbon source (such as [U-^{13}C]glucose or [^{13}C] bicarbonate), a mixture of substrates (such as ^{13}C cellular hydrolysates), a limiting nutrient (such as $^{15}NH_4^+$) or a nonspecific tracer of activity (such as D_2O, $H_2{}^{18}O$)[62,68,70,75–80]. In this case, tracer concentration and the fractional isotopic abundance of the medium (f_{medium}) can be controlled. Knowing f_{medium} and the time-resolved measurements of fractional isotopic abundance within cells (f_{cell}) enables computation of the absolute magnitude of the assimilation of the substrate of interest into cell biomass, and thereby growth rates of individual cells[68]. In assessing in situ rates in environmental and microbiota samples, the tracer ideally would not stimulate growth. To be detected by Raman microspectroscopy, however, stable isotope substrates usually need to be added at non-tracer concentrations and as the dominant isotopologue of a substrate of interest (for example, ^{13}C-tracer concentration $\gg$ in situ ^{12}C-analogue concentration). Thus, the tracer inflates the native substrate pool size and may stimulate activity[68]. Experimental design and interpretation must account for this potential artefact. In cases for which f_{medium} cannot be determined, valuable information can still be derived on relative activities between individual cells from SIP incubations and also more generally about the flow of metabolites between cells and with the environment.

Results

Raman spectra

A Raman spectrum is a multivariate data set that consists of discretized wavenumbers (*x* axis) and corresponding signal intensities (*y* axis). Wavenumber (cm^{-1}) is the commonly used unit to represent the Raman spectral shift from the laser excitation energy. The Raman shift (in cm^{-1}) is calculated as $\Delta\nu = (1/\lambda_{Inc} - 1/\lambda_{Scat}) \times 10^7$, where λ_{Inc} and λ_{Scat} denote the wavelengths (in nm) of the incident and scattered light, respectively, and the value 10^7 provides the conversion of the units from nm^{-1} into cm^{-1}. The locations of peaks of interest within a Raman spectrum are independent of the wavelength of the laser employed. For instance, the peak resulting from aromatic ring breathing for the amino acid phenylalanine is located at 1,002–1,008 cm^{-1} when a microorganism is measured using either a 488 or 532 nm laser. To interrogate the molecular composition of microorganisms, a spectral window of 700–3,400 cm^{-1} is typically employed. This covers the biomolecular fingerprints of microorganisms (<1,800 cm^{-1}; for example, carbohydrates, proteins, lipids, nucleic acids and carotenoids)[22], a Raman-silent region (1,800–2,700 cm^{-1}) in most (but not all) microorganisms and a carbon–deuterium peak (2,040–2,300 cm^{-1}) for SIP as well as CH stretching and water peaks (>2,700 cm^{-1}).

Raman data are quasi-quantitative. Signal intensity at a given wavenumber is linearly proportional to the concentration of the compound corresponding to that wavenumber; however, signal intensity does not provide an absolute value of the concentration of the compound. Thus, changes in molecular composition in different physiological, metabolic or ecological states can in many cases be directly evaluated by comparing intensities of the peaks[81]. To facilitate such comparisons between samples, relative intensities should be used, taking the intensity of the signal of interest with respect to a reference signal that is invariant with conditions and cell state, as absolute intensity values can vary with variation in cell size and morphology[70], as well as sampled volume, which

Isotopologue
A molecule that is structurally identical yet differs from another by the presence of at least one atom that possesses a different number of neutrons.

Uniformly labelled tracer
A molecule in which all available positions for a given element are occupied by an isotopically heavy or radioactive nuclide, typically noted as [U-^{n}E]compound, where *n* = atomic mass, E = elemental symbol, U = uniformly, followed by chemical form.

Fractional isotopic abundance
The proportion of atoms in a molecular pool populated by the heavy isotope — also referred to as atom% (multiplied by 100).

Biomolecular fingerprint
An indicator in which chemical properties of a biomolecule are encoded; in vibrational spectroscopy, collective vibrational frequencies in wavenumber of chemical bonds within a biomolecule.

Raman-silent
The absence of Raman-active vibrational modes.

Savitzky–Golay filter
A filter algorithm that fits a polynomial of a known order to each point in the spectrum, using a sliding window of a user-defined width, subsequently replacing each point with the fitted value at the centre of the window.

is sensitive to sample opacity, thickness and focal plane. To relate signal intensities to absolute concentrations, independent measurements should be used to generate a calibration curve[68,81,82]. Within a spectrum, a molecule that corresponds to a strong peak cannot be considered to be more abundant than a molecule that corresponds to a weaker peak — a calibration curve must be generated for each peak.

To determine the identity of peaks within Raman spectra, there are currently two approaches. In one approach, published spectra or tables (or a commercial data library such as KnowItAll) listing correspondences of biomolecules with spectral peaks can be used (Supplementary Table 1) — many applications can be covered using this approach. Alternatively, molecular identity can be established using theoretical calculations. There are a number of commercial (OptiFDTD) and open-source (GAMESS, ORCA) tools that can estimate Raman emission values on the basis of quantum mechanics. Although feasible, this has not been widely adopted for analyses of biological samples, as many of these tools were optimized for pure solids. As Raman interrogations of biological samples attract further interest, we expect that this approach will become more widely adopted. Spectral peaks may not exactly match reported or calculated values as the wavelength shift can vary somewhat depending on the precise configuration of the Raman microspectroscope and the presence of side chains on molecules and intermolecular interactions; thus, care should be taken in interpreting measured spectra. It is not straightforward to suggest acceptable margins; instead a comparison with measurement of control samples (lacking in or abundant with chemical of interest) or pure chemical of interest (commercially available or isolated from the sample) could confirm the identity of the peaks of interest.

Box 4 | **Tracer selection**

In designing a stable isotope probing (SIP) experiment, it is ideal to use tracer substrates that are uniformly labelled with one or more of the four small stable isotopes (^{2}H, ^{13}C, ^{15}N, ^{18}O).

Carbon
Carbon is the most commonly chosen isotope because it comprises about 47–50% of cellular mass[243]. Several vibrational modes produce distinctive Raman peaks for different isotopologues that can be used to calculate fractional isotopic abundance ($f_{\mathrm{cell}} = {}^{13}\mathrm{C}/({}^{13}\mathrm{C} + {}^{12}\mathrm{C})$) in a particular moiety or an entire cell. For example, the ring breathing modes of purines, pyrimidines and the essential amino acid phenylalanine, and vibrational modes emanating from carotenoids of photoautotrophs, are all useful reporters of ^{13}C assimilation[62,68,75].

Deuterium
Deuterium is a versatile tracer for SIP–Raman experiments. Deuterated tracers (such as deuterium-labelled dimethylsulfoniopropionate, DMSP) can be used to track substrate assimilation and to unravel biosynthetic pathways[62,125,244–246]. Alternatively, amending the medium with 10–50% (vol/vol) D_2O enables identification of all metabolically active cells after brief incubation. The clear advantage of the D_2O approach is that the investigator need not make any supposition about which substrates support microbial growth. Furthermore, unlabelled substrates or antagonists of interest can be added together with D_2O to screen for substrate-induced stimulation or inhibition of growth of microbial taxa[69]. Addition of D_2O with concentrations up to 50% (vol/vol) reportedly do not strongly inhibit growth of tested bacterial strains[70]. D_2O can have subtle effects on microbial growth even at much lower concentrations[247–249].

Nitrogen
Use of SIP–Raman to track the movement of nitrogen ($^{15}\mathrm{NH}_4^+$, $^{15}\mathrm{NO}_3^-$, $^{15}\mathrm{N}_2$) from dissolved pools through individual cellular pools is challenging because N comprises only about 14–16% of cellular mass[243]. Raman shifts caused by ^{15}N replacement can overlap with neighbouring Raman bands, and maximal spectral shifts between the 100% ^{14}N and 100% ^{15}N isotopologues are only 13–17 cm^{-1} (REFS[78,80]). Surface-enhanced Raman spectroscopy (SERS) has been employed to measure $^{15}\mathrm{N}_2$ fixation by cultured diazotrophs with improved sensitivity[78], yet care should be taken considering the potential limitations of SERS for adoption in microbiology.

Oxygen
Similar to using D_2O, $H_2{}^{18}O$ can be used as a general tracer of anabolic activity. SIP–Raman experiments with a $H_2{}^{18}O$ tracer combined with 2D correlation analysis have been used to track protein synthesis and DNA replication in single cells through all bacterial growth phases[250].

Data processing

Many Raman peaks are specific for a particular chemical moiety; thus, data analysis can often be a simple matter of tracking the magnitude of a peak of interest and can be carried out on the raw spectra (FIG. 4a) or after a mild degree of pre-processing (such as de-noising only or baseline subtraction). Raman spectra are also amenable to multivariate statistical analyses and machine-learning approaches (also reviewed in REFS[83,84]). In the latter, accounting for dimensionality and various sources of noise requires careful pre-processing to ensure high-quality data for repeatable downstream analyses. In particular, for analyses of dry cells, measurements are often accompanied by considerable background; thus, pre-processing is needed to allow quantitative comparisons. It is essential that algorithms and parameters for the pre-processing are identical for all data, otherwise quantitative comparisons are invalidated. Libraries for Raman data processing (particularly pre-processing) can be found in TABLE 1.

De-noising. De-noising includes spectral smoothing and spike removal to prevent electronic noise or artefacts (mainly arising from cosmic rays) from dominating measured Raman signals (FIG. 4b,c). The most established approach to reduce spurious background noise is with application of the Savitzky–Golay filter[85,86]. A related class of noise-reduction techniques relies on the fitting of wavelet functions at each point in the spectrum, followed by subsequent soft thresholding[87]. In contrast to Savitzky–Golay, which uses a single polynomial, wavelet de-noising potentially provides the ability to conduct spectral smoothing and spike removal simultaneously, and to reduce noise at multiple levels of magnitude[88–90]. Dependence of its success on the specific choice of wavelet and threshold parameters represents a potential downside[87].

Baseline subtraction. Although not strictly necessary for many biological applications, baseline subtraction is useful to eliminate large contaminating signals that originate from several sources, including the instrument, the mounting substrate and the sample itself in the form of photoluminescence. The most commonly used approaches involve iteratively shrinking the intensities of the individual columns of the spectrum via comparisons with an approximated curve (FIG. 4d,e). A popular group of algorithms[91,92] rely on the repeated fitting of a

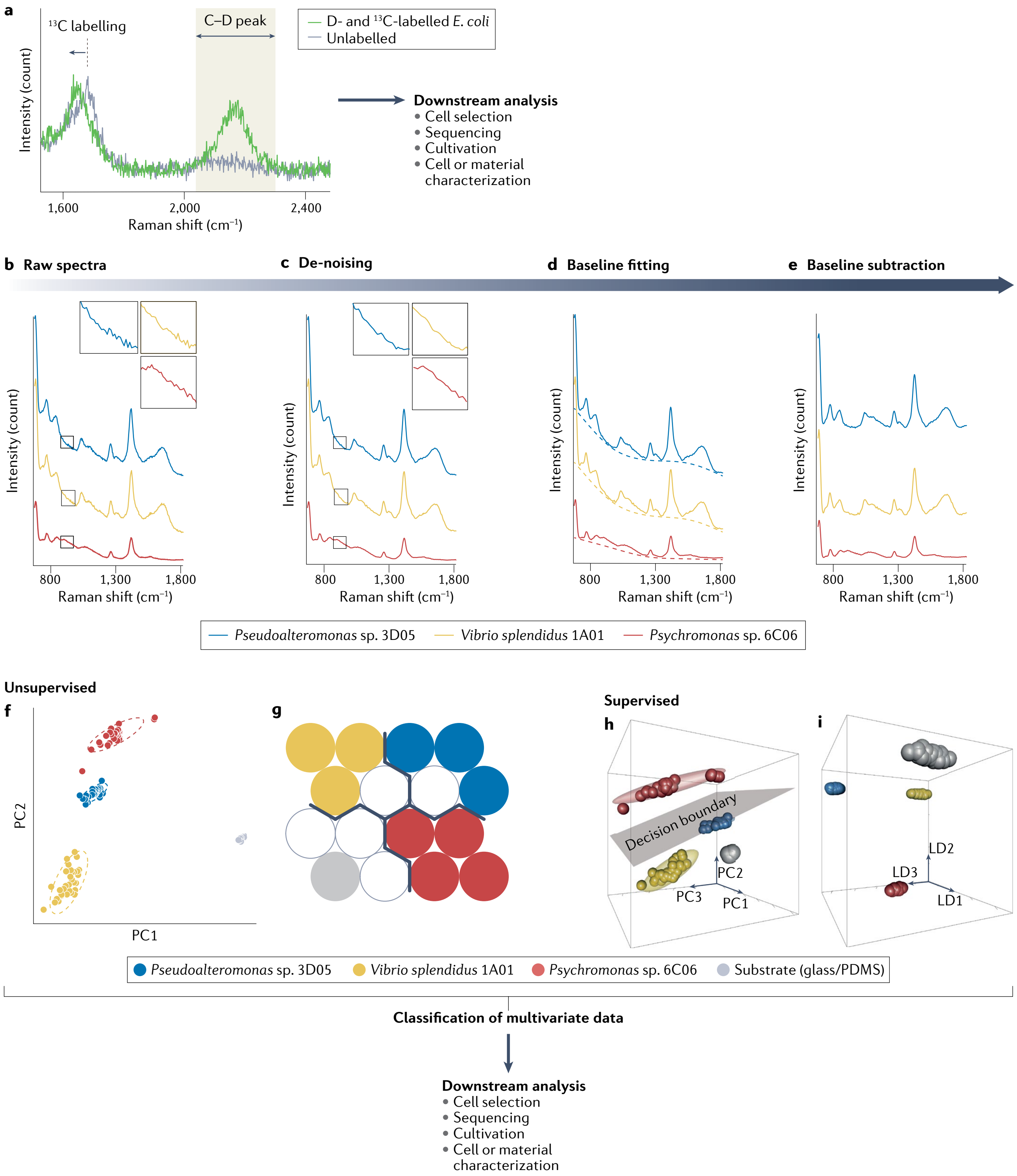

polynomial curve to the spectrum, followed by subsequent clipping of larger peaks until the spectrum falls below a threshold value, then subtracting the fitted polynomial from the original spectrum.

A related class of iterative fitting approaches is that of asymmetrical least squares. This method iteratively compares a spectrum with a version of itself that has been blurred via a sliding window average, using a least squares fit. Each wavenumber is then progressively down-weighted using separate weights for intensities above and below the fitted curve, with a bias against peaks remaining above the blurred baseline[93]. This approach is typically computationally faster and simpler than polynomial fitting, while producing similar

◀ Fig. 4 | **Raman data processing. a** | Raw spectra can be directly used in a number of analyses, such as direct measurement of peaks of interest with stable isotope probing (SIP). Raman spectra following SIP, where the carbon–deuterium peak, indicated as the C–D peak (2,040–2,300 cm^{-1}) and the location shift of the C=C peak (from 1,660 cm^{-1} to 1,618 cm^{-1}) indicate metabolic activity and carbon metabolism of microorganisms, respectively, during the incubation period. **b** | Raw data obtained from real Raman spectra from high-density cultures of three different bacterial strains (*Pseudoalteromonas* sp. 3D05, *Vibrio splendidus* 1A01 and *Psychromonas* sp. 6C06). **c**,**d** | High-frequency noise is removed from the raw spectra using wavelet de-noising (part **c**), followed by fitting of the baseline (part **d**; shown here using asymmetrical least squares; dashed lines). **e** | The calculated baseline, arising from the surrounding medium or substrate is subtracted to provide an approximation of the pure spectra (representing the cells). **f** | The simplest example of an unsupervised multivariate analysis is principal component analysis (PCA), which emphasizes differences between samples by fitting a new set of orthogonal axes along the directions of maximum variance in the data set ($n = 32$ for each species, substrate is a glass/PDMS microfluidic device for panels **f**–**i**). Dashed lines represent 95% confidence intervals for each group. **g** | Self-organizing maps are a slightly more advanced unsupervised technique in which a 2D grid of nodes, each representing an archetypal data point occupying some volume of the underlying multivariate space, is stochastically trained to fit the data set such that closely related nodes group together. Here, the circles indicate nodes ($n = 16$). The colour indicates that the node is substantially occupied by one of the corresponding bacterial species or the substrate. White nodes represent null spaces and bold lines represent borders separating the nodes of each group. **h** | Support vector machines (SVMs) divide a multivariate space into 'is' and 'is not' volumes for a group of interest. In this example, the hyperplane represents the decision boundary of a SVM trained to identify *Psychromonas* sp. 6C06. **i** | Linear discriminant analysis is a straightforward classification technique. Tight clustering of points in the trained space show that the new axes are fitted to simultaneously maximize between-group variance while minimizing within-group variance. PDMS, polydimethylsiloxane.

results, and thus may be better suited to studies with a large number of spectra[93].

Normalization and outlier removal. Normalization of individual spectra is of value for any application where the intent is to compare samples across different experiments, as small differences in instrument setup, substrate and sample preparation can greatly affect the intensity of the signal. Additionally, normalization is useful when the relative intensity of the peaks is of interest for comparison between data sets, as opposed to the absolute intensity. Although there are many methods for normalizing multivariate data[94], a straightforward approach that preserves the characteristic Raman spectral shape is vector normalization[95].

For analyses of large data sets, algorithms for outlier removal provide an efficient means to avoid skewing of statistical results. In many cases, such as data influenced by fluorescence, outliers may be obvious owing to an extremely strong signal and may be discarded on the basis of predetermined thresholds. In other cases, particularly where a large number of measurements are involved, it may be beneficial to implement some form of automated outlier removal. Automated methods based on Mahalanobis distance have been used to successfully eliminate such outliers from large Raman data sets[96].

Classification of multivariate data. Raman spectra are amenable to a variety of exploratory (unsupervised) or directed (supervised) multivariate data analyses. The most familiar example of exploratory data analysis is principal component analysis (PCA; FIG. 4f). PCA can be useful as an exploratory approach in itself or for cursory inspection of major differences between samples. Similarly, the use of hierarchical clustering or other simple clustering methods can also provide a good initial approximation of divisions within the data. Slightly more advanced tools are related linear-decomposition/blind source separation techniques such as non-negative matrix factorization[97] and independent component analysis[98–100] or unsupervised learning approaches such as self-organizing maps[101–103] (FIG. 4g), each of which has been used in applications of Raman microspectroscopy to microbiology.

Supervised approaches can make use of simple classifiers[104,105] or more advanced techniques, such as artificial neural networks or random forest classifiers[106,107]. These approaches are useful when attempting to identify a particular known class of cells, material (such as biofilm) or cellular metabolic state. Simple classifiers such as support vector machines (SVMs) and linear discriminant analysis (LDA) are very effective at separating Raman data. These classifiers represent a good entry point for ones seeking to distinguish between one or more types of cell or biological material. In its simplest incarnation, using a linear kernel, a SVM (FIG. 4h) uses boundary points that are selected from known groups of data to fit a separating hyperplane between classes of interest. In LDA (FIG. 4i), $(n - 1)$ new axes are fitted to maximize the difference between (n) known (presumed Gaussian) groups of data, while minimizing the variance between data within each group. To classify new data points, typically a Bayesian approach[108] is used, assigning an identity to each point according to the prior probabilities of each group along each linear discriminant.

A caveat to all classifier-based approaches is that they are entirely limited by the training data used. As an example, classifiers have proved very successful at differentiating between single cells and colonies for a number of strains of *Staphylococcus*[106,109] based on Raman spectra, but are incapable of making the same distinction for samples that contain new strains — those not reflected within the training data — and would be prone to false positives as prior screening does not ensure that samples fall within the currently defined outputs. Thus, training data need to be carefully chosen beforehand, with regard to the downstream application.

Data interpretation

In this section, we discuss best practice for analysing Raman data. In comparison with the previously described techniques, where the wide spectral region is used as a whole to classify microorganisms or molecules, we focus here on approaches to interpret the measured data on the basis of individual peaks. We outline six methods: identification of biomolecules based on normal Raman microspectroscopy; measurement of resonance-inducing substances; SIP–Raman and FISH–Raman for measurement of phenotypes (such as metabolic activities and functional roles within the community) or identities (using 16S rRNAs) of cells of interest, respectively, from within a complex microbial community; measurements of biomolecules using SERS and SEHRS with increased sensitivity and selectivity;

Vector normalization
A normalization approach in which the intensity at each wavenumber is divided by the square root of the sum of squares of intensities for all wavenumbers within a spectral window, such that the Euclidean distance from the origin in the multidimensional space is equal to 1.

Mahalanobis distance
A measure of the distance between a point and the centroid of a multivariate normal distribution, in units of standard deviation.

Non-negative matrix factorization
A technique that represents each point in a set of mixed spectra as a weighted mixture of a finite number of conserved sub-spectra, with the axes being directly interpretable as Raman sub-spectra.

Independent component analysis
A technique that optimizes a new set of axes to naively capture covariance between variables separately for each of a finite number of independently varying subsets of data.

Table 1 | **Software packages for processing Raman microspectroscopy data in three common programming languages**

Language	Useful libraries	Description	Licence
MATLAB	Raman Processor	A graphical user interface (GUI) platform that was designed in-house (developed by Lee, Landry & Stocker) for de-noising (based on the Savitzky–Golay algorithm) and baseline subtraction (based on polynomial fitting)	MathWork; libraries released here are under the MIT licence
Python	RamPy	Package for Raman data analysis, contains multiple options for pre-processing routines and some functions for downstream analysis	GPL2
	Scipy.signal	Implementation of Savitzky–Golay filtering and other signal processing routines	BSD
	peakutils	Functions for peak finding	MIT
	pywt	Library for wavelet transformations	MIT
	chemospec	Comprehensive package for chemometric data analysis, contains many options for pre-processing (baseline subtraction, smoothing) as well as advanced functions for downstream analysis	GPL3
R	hyperspec	Family of packages for hyperspectral imaging data with a focus on biological applications; also contains several parsers for common Raman data formats	GPL3

and chemical imaging in terms of a specific wavenumber using CRSM.

Identification of biomolecules. A Raman spectrum of a single microbial cell provides a comprehensive biomolecular fingerprint (representing, for example, nucleic acids, protein, lipids, carbohydrates; Supplementary Table 1), reflecting the identity and metabolic physiology of the cell. Overall spectral shape within a broad spectral region (700–3,400 cm^{-1}) can be used to differentiate between strains using supervised machine-learning classifiers[106,110,111].

Alternatively, specific peaks can be used to investigate cells and their phenotypes of interest within a complex microbial community. Here, we illustrate this approach using Raman spectra of *Bacillus cereus*, a member of the phylum Firmicutes. When vegetative cells encounter harsh environmental conditions such as desiccation or lack of nutrients, they create a dormant endospore that germinates when favourable conditions return[112]. The formation of the endospore is accompanied by production of calcium dipicolinic acid (CaDPA) and this can be detected in Raman spectra on the basis of corresponding peaks at 824, 1,017, 1,395, 1,446 and 1,572 cm^{-1} (REF.[113]). Endospores can be distinguished from vegetative cells on the basis of greater overall intensity in the spectrum (FIG. 5a), possibly owing to a denser biomass within the endospore. Alternatively, specific Raman peaks can be used. For example, the height of the peak at 1,572 cm^{-1} becomes greater than the peak at 1,650 cm^{-1} (corresponding to C=C and C=O bonds in diverse biochemicals) for the endospore. Additionally, quantifying the height difference between these two peaks enables the process of entry to or exit from dormancy of the cell to be marked.

Resonance-inducing substances. When microorganisms of interest contain molecules that can generate resonance Raman scattering (such as carotenoids, cytochrome *c*, rhodopsins, haem proteins, flavin nucleotides and vitamin B_{12})[76,114–119], they can be measured with 1,000-fold higher sensitivity than normal Raman microspectroscopy. Here, we use the analysis of carotenoid-containing microorganisms as an example. The carotenoids, common pigments present in photoautotrophic microorganisms (and some heterotrophs[120]), act as a light-harvesting antenna at blue–green wavelengths and protect light-harvesting complexes[121]. Thus, the ability to measure carotenoids provides a means to identify the microorganisms that participate in the global carbon cycle. Carotenoids become resonant with a wide range of excitation wavelengths (from UV to near-infrared) and three Raman peaks can be used to measure them (FIG. 5b): 1,001–1,007, 1,154–1,156 and 1,511–1,517 cm^{-1}, corresponding to C–CH_3 deformation, C–C stretching and C=C stretching, respectively. The peak at 1,511–1,517 cm^{-1} is the strongest, whereas the peak at 1,001–1,007 cm^{-1} is often relatively weak compared with the other two (FIG. 5c). Measuring the intensity at 1,511–1,517 cm^{-1} enables the identification of carotenoid-containing cells from heterotrophs, potentially followed by sorting of the cells for downstream analysis. The position of the peaks varies depending on the type of carotenoid (such as fucoxanthin, β-carotene or astaxanthin); thus, in conjunction with measurements of commercially available pure carotenoids, the identity of carotenoids in the cell can be determined. This approach is useful for many other Raman experiments. Raman measurements of the pure chemicals of interest are necessary to confirm identification and calibrate quantification. A trade-off is that a resonance Raman spectrum is dominated by the resonance-inducing substances, thus optical[12] or chemical[122] techniques bleaching those substances must be considered to detect non-resonant biomolecules.

SIP–Raman. SIP experiments produce easily interpretable Raman spectra, providing an efficient means to quantify microbial phenotypes of interest at single-cell level.

Isotopomers
Isotopomers of a compound have the same number of each isotope, but their positions differ.

Voigt probability distribution profile
A convolution of Gaussian and Lorentzian probability distributions that is widely used in peak-fitting routines to describe the symmetry of peaks in Raman spectroscopy.

For example, growing photoautotrophic microorganisms in [^{13}C]bicarbonate for several hours and then measuring the red shift of Raman signals from carotenoids allows quantification of cell growth rates and photophysiology (such as photosynthetic efficiency) with high sensitivity[66,68]. The three carotenoid peaks are widened first to lower wavenumbers with an increase in the level of ^{13}C labelling and then shifted to lower wavenumbers (FIG. 5d). For instance, the peak at 1,156 cm^{-1} (C–C stretching) moves to 1,133 cm^{-1} and then 1,110 cm^{-1} with the change from ^{12}C–^{12}C to ^{13}C–^{12}C and ^{13}C–^{13}C. The approach for quantification is described in REF.[68]. After bleaching the dominant carotenoid signals, other non-resonant biomolecular signals can be revealed. We focus on the interpretation of red shifts in phenylalanine peaks as a measure of carbon metabolism. Four sets of paired isotopomers of ^{13}C-labelled phenylalanine[77] (0, 2, 4 and 6 out of 6 ^{12}C within the aromatic ring are substituted by ^{13}C) produce peaks at 1,002–1,006, 988–989, 976–977 and 962–966 cm^{-1}, respectively (FIG. 5e). For quantitative data analysis, a peak-fitting approach can be applied using a Voigt probability distribution profile. Assuming that the ^{13}C fractional abundance in the phenyl ring is representative of all cellular pools, then cellular fractional abundance (f_{cell}) can be calculated as $f_{cell} = (I_{966} + 0.67I_{977} + 0.33I_{988})/(I_{966} + I_{977} + I_{988} + I_{1,002})$, where I represents Raman intensity at a wavenumber and weighting factors 0.67 (2/3) and 0.33 (1/3) correspond to the number of ^{13}C atoms per isotopologue.

Limits of detection in SIP–Raman experiments vary between isotopes, tracer substrates and detection mode. For example, an f_{cell} of 0.10 (10 atom%) has been suggested as the limit of detection for bacteria labelled with either ^{13}C or ^{15}N substrates when analysed using normal Raman microspectroscopy[74]. Detection by resonance Raman scattering has been shown to lower limits of detection to an f_{cell} of 0.03 (3 atom%) for ^{13}C assimilated by photoautotrophs[68]. For comparison, nanoSIMS offers a significantly lower limit of detection ($f_{cell} = 0.001$; 0.1 atom%) for assimilated ^{13}C (REF.[123]), but at significantly higher costs and lengthier analysis times as well as sacrificing the ability to perform measurements of live cells.

SIP experiments based on deuterium labelling is another versatile approach to investigate the general metabolic activities of microorganisms of interest from within a complex microbial community. Measurement of f_{cell} in this case is even simpler, involving calculating the ratio of integrated intensities under the C–D$_x$ (2,040–2,300 cm^{-1}) and C–H$_x$ (2,800–3,100 cm^{-1}) peak regions[69,70,78,124–126] (FIG. 4a).

FISH–Raman. FISH with rRNA-targeted oligonucleotide probes (BOX 3) can be used to identify cells of interest within a complex microbial community, and subsequent Raman measurements can quantify functional properties of those cells[62]. Here, we use the example of naphthalene degraders (*Acidovorax* spp. and *Pseudomonas* spp.) in groundwater biofilms[127]. For FISH, probes for *Acidovorax* spp., *Pseudomonas* spp. and all bacterial cells can be labelled using cyanine 3 (Cy3; excitation/emission at 550/570 nm; red emission), fluorescein isothiocyanate (FITC; 495/518 nm; green emission) and cyanine 5 (Cy5; 650/670 nm; purple emission), respectively, to allow them to be differentiated in imaging using fluorescence microscopy (FIG. 5f). Following bleaching of fluorescence to avoid interference with Raman measurement using a 532 nm laser, the level of naphthalene degradation by each group of cells can be quantified using SIP–Raman (after supplementing the medium with [^{13}C]naphthalene), by calculating the intensity ratio $f_{cell} = I_{967}/I_{1,003}$ (FIG. 5g,h).

This FISH–Raman technique has been applied in many other systems, for example, in investigations of polyphosphate accumulating organisms (PAOs) in wastewater treatment plants[81,128] and of the composition of storage compounds in marine microbial consortia that mediate anaerobic oxidation of methane[129].

SERS and SEHRS. Interpretation of SERS spectra requires one to take into account the fact that metallic nanoparticles used for SERS interact with molecules in a sample, which may create discrepancies in the number, location and relative intensities of Raman peaks between normal Raman and SERS signals[130]. For example, adenine has a strong Raman peak at 734 cm^{-1} in SERS measurement[131], whereas this peak can be found at 721 cm^{-1} in normal Raman spectra[132,133]. Unlike in normal Raman spectra, when charge, pH or concentration of an analyte molecule changes, variation in the relative intensities of spectral bands or the absence of vibrations of specific functional groups occurs owing to the strong dependence of the SERS enhancement on these parameters. Thus, care should be taken when generating a calibration curve that is used to relate signal intensities to absolute concentrations of the chemical[134].

SEHRS can complement SERS data. The generation of SEHRS signals is governed by different selection rules; thus, SEHRS can reveal peaks that are relatively weak or not visible in SERS spectra. For example, adenine peaks at 564, 920, 1,141, 1,372 and 1,464 cm^{-1} become intensified and peaks at 1,600 and 1,653 cm^{-1}, which are infrared-active, become visible in SEHRS (FIG. 5i).

CRSM. CRSM imaging provides selective molecular information using an imaging modality that is similar to optical microscopy imaging. To illustrate the approach, we use two SRS images of deuterium-labelled *Pseudomonas aeruginosa* cells in blood (FIG. 5j), visualized using protein (C–H; 2,915 cm^{-1}) and carbon–deuterium (C–D; 2,168 cm^{-1}) peaks. A 1,045 nm Stokes laser is used, and the pump laser is set at 801 and 852 nm, generating SRS signals at $(1/801 - 1/1{,}045) \times 10^7 = 2{,}915$ cm^{-1} and $(1/852 - 1/1{,}045) \times 10^7 = 2{,}168$ cm^{-1}, respectively. The SRS image based on the C–D peak identifies the deuterium-labelled *P. aeruginosa* cells, whereas the blood cells are also visualized in the image for the protein.

Applications

Cellular metabolism and interactions

Cellular metabolism. Measurement of storage compounds (such as lipids, polyhydroxyalkanoates, polyphosphate and glycogen) within microorganisms is a very common application of Raman microspectroscopy in microbiology[81,129,135–144]. For example, this approach

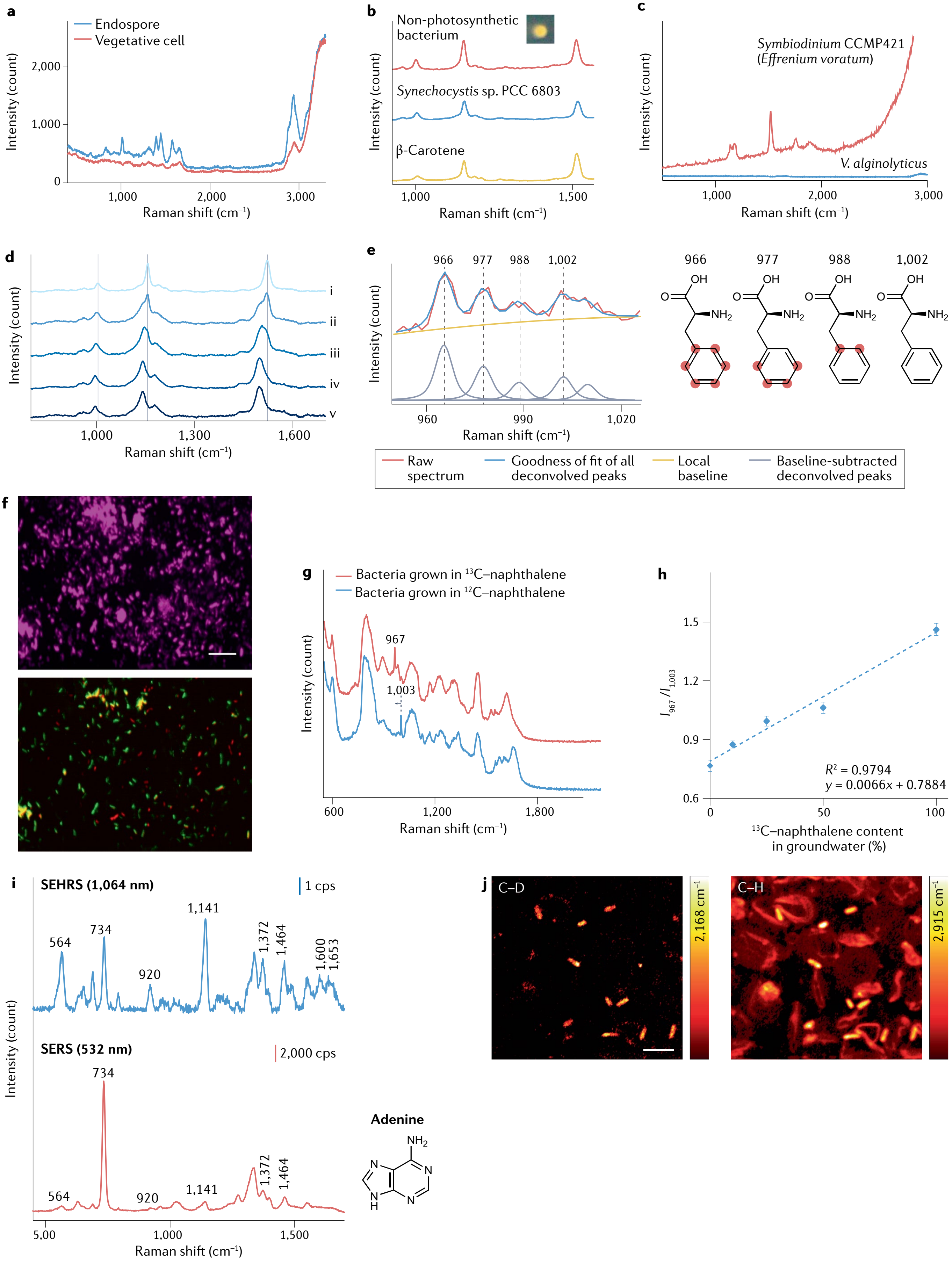
a
Endospore
Vegetative cell
Intensity (count)
0
1,000
2,000
1,000
2,000
3,000
Raman shift (cm⁻¹)
b
Non-photosynthetic bacterium
Synechocystis sp. PCC 6803
β-Carotene
Intensity (count)
1,000
1,500
Raman shift (cm⁻¹)
c
Symbiodinium CCMP421 (Effrenium voratum)
V. alginolyticus
Intensity (count)
1,000
2,000
3,000
Raman shift (cm⁻¹)
d
i
ii
iii
iv
v
Intensity (count)
1,000
1,300
1,600
Raman shift (cm⁻¹)
e
966
977
988
1,002
Intensity (count)
960
990
1,020
Raman shift (cm⁻¹)
966
977
988
1,002
OH
O
NH2
Raw spectrum
Goodness of fit of all deconvolved peaks
Local baseline
Baseline-subtracted deconvolved peaks
f
g
Bacteria grown in 13C–naphthalene
Bacteria grown in 12C–naphthalene
967
1,003
Intensity (count)
600
1,200
1,800
Raman shift (cm⁻¹)
h
I967 /I1,003
0.6
0.9
1.2
1.5
R² = 0.9794
y = 0.0066x + 0.7884
0
50
100
13C–naphthalene content in groundwater (%)
i
SEHRS (1,064 nm)
1 cps
564
734
920
1,141
1,372
1,464
1,600
1,653
SERS (532 nm)
2,000 cps
734
564
920
1,141
1,372
1,464
Intensity (count)
5,00
1,000
1,500
Raman shift (cm⁻¹)
Adenine
NH2
N
N
N
N
H
j
C–D
2,168 cm⁻¹
C–H
2,915 cm⁻¹

◀ Fig. 5 | **Raman data interpretation. a** | Raman spectra of a *Bacillus cereus* endospore and vegetative cell. The peaks at 824, 1,017, 1,395, 1,446 and 1,572 cm^{-1} correspond to calcium dipicolinic acid (CaDPA), which accumulates in the endospore. **b** | Resonance Raman spectra of a non-photosynthetic bacterium (red), *Synechocystis* sp. PCC 6803 (blue) and pure β-carotene (orange). The three peaks at 1,001–1,007, 1,154–1,156 and 1,511–1,517 cm^{-1} correspond to carotenoids. **c** | Comparison of Raman spectra from a carotenoid-containing *Symbiodinium* CCMP421 microalga (red) and a carotenoid-lacking *Vibrio alginolyticus* bacterial cell (blue). The high level of background in the *Symbiodinium* spectrum corresponds to fluorescence signals that accompany the resonance Raman scattering. **d,e** | Stable isotope probing (SIP)–Raman spectral analyses of isotopic signatures of photoautotrophs grown on [^{13}C]bicarbonate. **d** | Resonance Raman spectra of single *Synechococcus* sp. cells from cultures grown on natural ^{13}C abundance (1.1% ^{13}C) (i) and from a culture in 54% ^{13}C medium after 3 (ii), 6 (iii), 12 (iv) and 24 (v) days of growth. Vertical lines indicate major peak positions in the 1.1% ^{13}C culture. **e** | Curve-fitting analysis of isotopic signatures of an *Emiliania huxleyi* cell (Prymnesiophyceae) with a calculated 65 ± 7% ^{13}C content. Raman spectral region around the four isotopologue peaks for the phenylalanine ring breathing mode (red trace, measured using a 633 nm laser after chemiphotobleaching to suppress autofluorescence). After baseline correction and normalization, the contribution of each isotopologue was determined by curve deconvolution and peak fitting (blue trace) to yield the lower spectrum[122]. In the molecular structures, the red dots represent ^{13}C substitutions in the phenyl ring[77]. **f–h** | FISH–Raman for microorganisms in groundwater. **f** | FISH images of bacterial cells hybridized with EUB338 (purple) and specific probes for *Acidovorax* sp. (cyanine 3-labelled probe, red) and *Pseudomonas* sp. (fluorescein isothiocyanate probe, green). Scale bar: 10 µm. **g** | Several bands of Raman spectra of individual bacteria shifted as they integrated [^{13}C]naphthalene upon incubation in minimal medium supplemented by [^{13}C]naphthalene as the sole carbon source (red), in contrast to medium supplemented with [^{12}C]naphthalene (blue). **h** | Correlation between [^{13}C]naphthalene content and red shift of the bacteria ($I_{967}/I_{1,003}$). **i** | Surface-enhanced Raman spectroscopy (SERS) and surface-enhanced hyper-Raman scattering (SEHRS) spectra of adenine (50 µM) obtained using nanoaggregates from hydroxylamine-reduced silver nanoparticles. SERS enabled the measurement with high sensitivity and SEHRS revealed additional peaks that are not visible in SERS or normal Raman scattering. **j** | Stimulated Raman scattering images of deuterium-labelled *Pseudomonas aeruginosa* cells among (unlabelled) blood cells. Images with respect to the C–D (2,168 cm^{-1}) and C–H (2,915 cm^{-1}; representing mainly proteins) peaks represent *P. aeruginosa* only and both types of cell, respectively. Scale bar: 5 µm. cps, counts per second. Panel **b** adapted from REF.[76], Springer Nature Limited. Panel **c** adapted from REF.[61], Springer Nature Limited. Panel **d** adapted from REF.[68], CC BY 4.0 (https://creativecommons.org/licenses/by/4.0/). Panels **f–h** reprinted with permission from REF.[127], American Society for Microbiology. Panel **i** adapted with permission from REF.[131], American Chemical Society. Panel **j** adapted from REF.[135], CC BY 4.0 (https://creativecommons.org/licenses/by/4.0/).

has been used to better understand mechanisms of enhanced biological phosphorus removal in wastewater treatment plants[81,137,138] and the ecophysiology of uncultivated, subsurface-living ammonia-oxidizing archaea[139,140] as well as consortia that mediate the anaerobic oxidation of methane[129].

Measurement of a wide variety of functional biomolecules (such as carotenoids and cytochromes that participate in photosynthesis, photoprotection and electron transfer within microorganisms; reviewed in REF.[145]) and their states is another common use of Raman microspectroscopy. For instance, cytochrome *c* and its oxidation state can be measured with high sensitivity by leveraging resonance Raman scattering. This has been used to understand the metabolism of cable bacteria, a unique group of multicellular, filamentous bacteria that inhabit sediments at the anoxic–oxic boundary[146]. Raman measurements have revealed that they have evolved a unique lifestyle by which they perform sulfide oxidation and oxygen reduction at each end of their centimetre-long filaments in the anoxic and oxic zones, respectively, based on the transport of electrons over this long distance[147].

The Raman spectrum of a cell reflects its physiological state. For example, measurement of [^{13}C]phenylalanine uptake by extracellular *Chlamydia* revealed that extracellular elementary bodies are in fact metabolically active and synthesize proteins when they are transmitted between hosts. This overturned an old dogma by which they were believed to be in a spore-like dormant state[148].

Raman microspectroscopy has also been used for measurements of the germination of dormant endospores in situ[149]. Time-resolved Raman measurements of individual endospore-forming Firmicutes (in particular, *Bacillus thuringiensis*) have been achieved by trapping cells using optical tweezers. Upon suspending the endospore powder in fresh, nutrient-rich medium, cells germinated after 30 min of lag phase and rapidly released CaDPA into the surrounding medium (FIG. 5a). Single-cell Raman measurements revealed cell-to-cell heterogeneity in time to germination, which may be an important strategy at the population level that promotes survival when favourable conditions are transient.

Host–microorganism, cell–cell and cell–environment interactions. In addition to the investigation of cellular metabolism, Raman measurements allow tracking of host–microorganism and intercellular interactions, providing insights into the functioning of these systems. One example is the symbiosis between the flatworm *Paracatenula* and its alphaproteobacterial endosymbiont, '*Candidatus* Riegeria'[57,150]. It was long unclear how *Paracatenula*, a host that lacks a mouth and a digestive system, obtains energy. Raman imaging of '*Ca*. Riegeria' revealed a large quantity of sulfur inclusions within the cell biomass, and metagenomics suggested that it gains energy via sulfur oxidation, fuelling the bacteria and their host[57]. Subsequent work using Raman microspectroscopy showed that '*Ca*. Riegeria' also harbours polyhydroxyalkanoates and carbohydrates that are transferred to the host via extracellular vesicles, serving as a primary energy storage in the host[150].

Raman imaging provides a powerful and non-invasive means to understand spatiotemporal and metabolic interactions within complex microbial communities that determine community function and macroscale processes in nature. For example, degradation of hyphae of the fungus *Mucor fragilis* by the soil bacterium *Bacillus subtilis* has been investigated using SIP–Raman (in conjunction with fluorescence imaging) based on ^{13}C and deuterium labelling, imaged within a microfluidic device containing a transparent soil microcosm[151]. Both planktonic cells and fungus-attached cells were metabolically active when the system was hydrated, whereas fungus-attached cells were more active under a dry-down–rewetting cycle, underlining the important role of fungi for the survival of bacteria under fluctuating environmental conditions.

Raman imaging of the structure, chemical composition and development of the biofilm matrix provides another good example[152]. Spectra can also be used to differentiate between colocalized cells of the same species in multi-species consortia[153–155]. For instance, measurements of the spatial distribution of carotenoid-containing bacteria within a pink multi-species biofilm (commonly found in household environments) revealed mutually exclusive distributions of different strains[156]. The pink biofilm is a potential pathogenic reservoir for immunocompromised patients, and Raman imaging could provide an efficient means to characterize this resistant matrix in situ.

Technical advances now enable visualizition of the chemical structure of biofilms with higher spatial resolution and throughput than previously possible. Chemical imaging of calcium alginate fibres (a model system for the biofilm matrix) with resolution of 20–50 nm has been achieved using tip-enhanced Raman spectroscopy (TERS)[130], and CRSM has allowed high-speed imaging (~7 s per frame of 256 × 256 pixels) of biosynthesis of phenazines, which promote antibiotic tolerance, within a *P. aeruginosa* biofilm[157].

Linking microbial functions to genes

Integrating Raman microspectroscopy and a cell sorting method is a powerful approach to link the phenotypes of microorganisms with their genotypes (BOX 5). In this approach, Raman microspectroscopy is used to identify cells of interest with a specific phenotype (such as metabolism or function) within a complex community, often in conjunction with SIP, and a chip-based device such as a microfluidic device is used to situate cells within the Raman interrogation volume during measurement and subsequently sort them on the basis of their spectra. The collected cells can be sequenced and the recovered genomes used to link the identities and genetic make-ups of the sorted cells to their phenotypes. Samples can be kept in liquid media throughout this analysis process and thus the cells of interest remain viable, enabling downstream cultivation for further ecological evaluation (reviewed in REFS[158–160]).

The first application of Raman-based cell sorting combined with single-cell genomics revealed the identity and gene content of uncultivated phototrophic bacteria from the ocean, part of what is known as microbial dark matter[116]. Marine microorganisms were probed by Raman microspectroscopy for the presence of carotenoid-containing chlorophyll or rhodopsin complexes, and target cells were sorted using Raman-activated cell ejection (RACE; BOX 5). Despite the low number of sorted cells (27 cells) and low genome coverage (4.17–19.29%), this method enabled the identification of novel carotenoid-containing bacteria, as well as novel functional genes involved in carotenoid and isoprenoid biosynthesis[116]. In another study, RACE was used to identify microorganisms that contribute to carbon fixation in the oceans[117]. Seawater samples from the sunlit ocean were spiked with isotopically labelled [^{13}C]bicarbonate and cells were ejected on the basis of resonant Raman bands corresponding to carotenoids that displayed ^{13}C-induced shifts (FIG. 5d). By sequencing groups of approximately 30 ejected cells that were sorted and pooled together, complete genomes and pathways for carotene synthesis were identified and reconstructed, and evidence for photosynthetic and anaplerotic CO_2 fixation was recovered in two previously unknown *Synechococcus* sp. and *Pelagibacter* sp.[117] (FIG. 6a). In recent development of Raman-activated gravity-driven encapsulation and sequencing (RAGE–Seq; BOX 5), high-quality single-cell genomes (>93% genome coverage) could be retrieved using between a few and a hundred cells that were sorted from clinical (urogenital tract infection) and soil microbiome samples[71,161].

Raman-based cell sorting has also been employed to study host-associated microbial communities and to identify microorganisms of interest for therapeutic applications[63,69,70] (FIG. 6b). To this end, D_2O was used as a tracer to follow metabolically active cells from mouse gut communities that were stimulated by supplementation with host-derived compounds, such as mucin or mucin-derived mucosal sugars (BOX 4; FIG. 4a). Two different Raman-activated cell sorting (RACS) methods (BOX 5) were then used to detect and sort D-labelled cells based on the presence of the specific C–D Raman peak. In the first approach, cells were manually sorted, and the collected cells were lysed and identified by 16S rRNA gene-targeted sequencing[70]. With the recent development of high-throughput RACS, it became possible to sort hundreds of cells of interest in a fully automated manner and to retrieve near-complete genomes of functionally active microorganisms, for example, from gut communities[63,69]. This revealed the identity of foragers of mucin and mucosal sugars, such as *Akkermansia*, *Allobaculum*, *Bacteroides*, *Barnesiella*, Clostridiales and

Box 5 | RACE, RACS and RADS

Raman-based cell sorting systems consist of hardware for Raman measurement of individual microorganisms and for sorting cells of interest based on mechanical, optical, electrical or magnetic force (reviewed in REFS[145,251]). The system configuration determines two key features: sorting throughput and the type of microorganisms that the system can handle. Here, we outline three designs: Raman-activated cell ejection (RACE), Raman-activated cell sorting (RACS) and Raman-activated droplet sorting (RADS).

RACE

Microorganisms are immobilized on a slide and cells of interest are identified on the basis of Raman measurements. The slide is inverted and transferred to a laser microdissection system so that cells of interest can be ejected towards a collection chip below[252]. The device has been engineered such that the sample is loaded at the bottom surface of the slide, so that identification and ejection of cells of interest can be performed without moving the slide[117]. RACE enables sorting of ~200–300 cells per day without limitations on the type of microorganism for sorting.

RACS

Integration of optical tweezers into a fluidic system provides a means to immobilize cells within the Raman interrogation volume during measurement, boosting the precision of Raman measurement, and then translocate those cells for collection. Raman and optical tweezers were operated manually within a glass capillary in which one end was filled with a sample and then cells of interest were translocated to buffer medium at the other end[70]. In a new version, an automated fluidic system is integrated, increasing sorting throughput from 1–2 cells per hour to up to 500 cells per hour and reducing the need for human intervention[61,63,69].

RADS

Encapsulating single cells of interest within individual droplets allows spatial isolation of those cells, facilitating a pipeline for single-cell genomics[253]. Cells of interest are searched and identified in still fluid based on Raman measurement, individually encapsulated and sorted, and then used for genomics. This process is known as Raman-activated gravity-driven encapsulation and sequencing (RAGE–Seq)[71]. Encapsulation of individual cells also facilitates rapid dielectrophoretic sorting of the single-cell droplets in conjunction with a fluidic device[72]. The former approach[71] is applicable for sorting of diverse types of microorganism (with throughput of 2 cells per minute), whereas the latter[72] has been demonstrated using relatively large cells (10 μm fungi and throughput of 40–120 cells per minute).

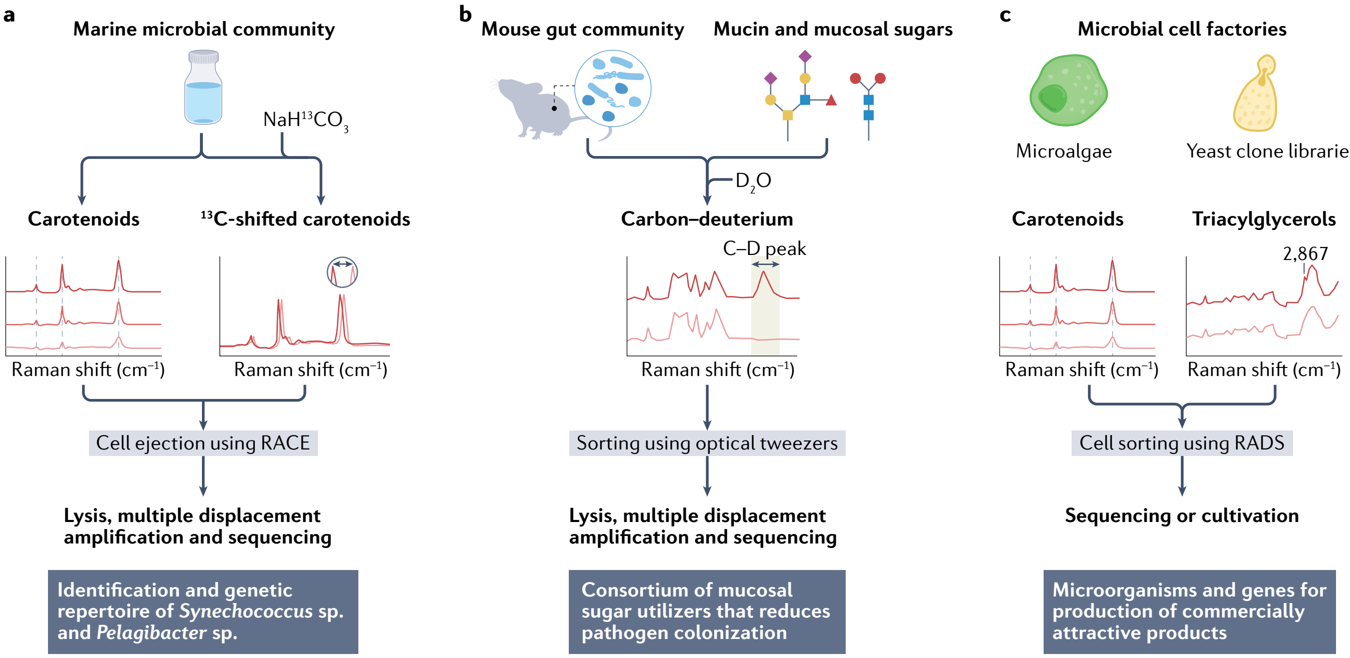

Fig. 6 | **Applications of Raman-based cell sorting to link ecological roles of microorganisms to their genomic identities. a** | Marine microbial cells displaying resonant carotenoid Raman bands (or ^{13}C-induced shifts in carotenoid bands due to incorporation of [^{13}C]bicarbonate) were sorted and their genomes amplified and sequenced. This led to the identification of novel organisms involved in carbon fixation in the ocean, as well as novel genes for carotene synthesis[116,117]. **b** | Mouse gut bacteria that are metabolically active when supplemented with mucin or mucosal sugars were labelled using D_2O and sorted based on the carbon–deuterium (C–D) peak (2,040–2,300 cm^{-1}) using optical tweezers, enabling the identification of a consortium of mucosal sugar utilizers able to counteract the pathogen *Clostridioides difficile*[63,69,70]. **c** | Microalgal or yeast cells accumulating large amounts of commercially attractive compounds such as the carotenoid astaxanthin or triacylglycerols were sorted based on characteristic Raman peaks, after encapsulation into individual droplets[72,163]. This allowed rapid screening and retrieval of microbial cell factories hyper-producing compounds of interest, as well as to the identification of novel genes encoding key enzymes in their synthesis[72]. RACE, Raman-activated cell ejection; RADS, Raman-activated droplet sorting.

Parabacteroides[69,70]. These results were used to assemble a probiotic mixture with potential to counteract the gut pathogen *Clostridioides difficile* through depletion of these sugars[69] (FIG. 6b). This example underscores the value of RACS to identify microorganisms that perform key functions within complex communities such as those in the gut and how this information can be used to manipulate community functions.

Recent technological advances, such as the development of droplet-based sorters, have drastically increased the throughput of Raman-based cell sorting, making it an attractive tool for biotechnological applications[72,162,163]. Rapid screening and selection of microbial cell factories that efficiently produce compounds of interest is now performed using Raman-activated droplet sorting[72,163] (RADS; BOX 5; FIG. 6c). This approach has enabled sorting of cells of the alga *Haematococcus pluvialis* able to produce large amounts of the commercially relevant antioxidant carotenoid astaxanthin, with a throughput of 260 cells per minute and >98% sorting accuracy[163]. A modified version of this platform (known as pDEP–RADS) allowed the rapid screening (120 cells per minute; unlike RADS, this does not rely on measurements of resonance Raman scattering generated from carotenoids) of cells of the yeast *Saccharomyces cerevisiae* accumulating microalgal triacylglycerols, which are regarded as a potential renewable alternative to fossil fuels. The further screening of a *S. cerevisiae* library expressing microalgal diacylglycerol acyltransferases followed by sequencing of sorted cells led to identification of previously unknown enzymes able to produce the monounsaturated fatty acid (MUFA)-rich triacylglycerols[72] (FIG. 6c). Raman-based sorting can thus streamline the selection of desirable microbial cell factories and, for example, contribute to achieving the high productivity required for microalgal biofuels to become economically feasible.

Multiplexed identification of microorganisms

Raman microspectroscopy has great potential in applications requiring the classification of a large number of taxa, phenotypes or pathotypes based on chemical fingerprinting. We outline two approaches: a label-free method (largely relying on machine learning) and barcoding of individual microorganisms using SERS tags.

A label-free approach. Innovations in machine learning (in particular, supervised approaches) for the analysis of multivariate data make this a useful means to classify taxa, phenotypes or pathotypes on the basis of detection of small variations in their Raman spectra. Most biomolecules that are measurable using Raman microspectroscopy are shared among taxa and thus the overall Raman spectra are usually very similar with respect to the locations and number of peaks[106,164]. Classification is rarely possible by eye based on the spectral shape[165]; thus, software tools with high discriminant ability are required. Supervised classifiers enable the detection of these small variations and have been used to identify pathogens[166–170], to differentiate between pathogenic and non-pathogenic *Escherichia coli* strains[171], to discriminate between antibiotic-resistant *E. coli* strains[172,173] and to differentiate between species in situ within biofilm communities[97,174].

Two aspects must be considered in the use of supervised classifiers. First, Raman spectra are greatly affected by the physiology of the microorganisms within a strain, such as heterogeneity in the metabolism (for example, respiration versus fermentation), growth state and biochemistry (such as the ratio of proteins to DNA)[164,175,176]. Second, the measurements are influenced by the biotic and abiotic surroundings. For instance, measurements of the same strain in urine, ascites, blood and soil are not identical. To take these aspects into account, we make the following recommendations: standardize conditions during sample preparation, including medium, culture time, pH, CO_2 concentration and diel cycle; establish a training database containing strains identical to those that will be used in real measurements and cross-validate it using an independent test data set; and where necessary, isolate cells of interest from peripheral biotic and abiotic neighbours to minimize artefacts[177].

Barcoding using SERS tags. Use of a SERS tag that is conjugated with an antibody or aptamer enables selective attachment of the tag to the targeted strain. Based on adoption of the technique in biomedical imaging (for example, in vivo imaging of tumour cells[178]), applications are expanding to biomedical microbiology, in particular, for the detection of pathogens using immunoassay platforms — devices that rely on an antigen–antibody reaction[179,180]. For example, *Staphylococcus aureus* and *E. coli* O157:H7, pathogens that cause clinical diseases (such as skin and respiratory infections) and foodborne poisoning, have been detected in liquid samples using this approach (FIG. 7), and with enhanced sensitivity by using device designs that enable spatial enrichment of the tagged cells based on dielectrophoresis or magnetophoresis[181–186].

In comparison with other technologies providing similar functionality (such as cultivation-based diagnosis methods, PCR and MALDI-TOF mass spectrometry[187]), SERS tags provide a rapid (on the order of a few minutes) and cultivation-free means for the multiplexed detection of microorganisms of interest. The use of SERS tags that are synthesized using different chemicals for the Raman reporter layer and then conjugated with different antibodies or aptamers enables targeted binding of these tags to different strains and thereby multiplexed detection. In comparison with the fluorescence-based tags that are commonly used, SERS peaks have an at least ten times narrower bandwidth, and, thus, the number of resolvable tags is increased accordingly. Despite this advantage, the technology has not yet reached its full potential for multiplexing. SERS tags are potentially applicable in microbiology as an alternative to fluorescence-based tags, for example, in genome-inferred antibody engineering — known as reverse genomics[188]. However, care should be taken in applying SERS tags for measurement of intracellular compounds of some microorganisms as their relatively large size (typically a few tens of nanometres) makes it difficult for them to penetrate cell walls or membranes.

Reproducibility and data deposition

There is currently no central, actively maintained repository for Raman spectra of biological and organic compounds. To accompany this Primer, we are in the process of establishing a web-based portal for the deposition of biological Raman data in a collaborative effort with the European Molecular Biology Laboratory (EMBL) as part of the BioStudies initiative — novel data sets can be submitted via the BioRaman template in the BioStudies data submission tool. This platform will provide a means to accumulate Raman data from diverse communities in microbiology and other fields of biology, and give full open access to these data, along with the metadata necessary to facilitate reproducibility. We hope this portal will provide an integrated and interactive resource similar to other established repositories for biological data, enabling community access to data and the measurement procedures to plan future research, and thereby stimulating wider adoption of Raman technology in microbiology and biology as a whole.

Minimum reporting standards

Details of the spectra and their acquisition, including wavelength and power of the laser, laser exposure time, the number of accumulations (for example, three, if a measured spectrum was averaged over three independent measurements), spectral resolution, specifications of the objective, the Raman system used and measurement type (for example, normal Raman, resonance Raman or SERS) are necessary. Other aspects of data treatment, as well as details concerning sample preparation and mounting are also crucial. As a starting point, we have deposited five examples of Raman data (formatted on the basis of this minimum reporting standard) in the repository (also included in Supplementary Data 1): bacterial pure cultures of *E. coli* (measurements of three samples in liquid: ^{13}C- and deuterium-labelled, ^{13}C-labelled and not labelled) and *Vibrio alginolyticus* (measurements of two dry samples: deuterium-labelled and not labelled; data used in FIGS 1b; 3a); a xenic microalga culture of *Chaetoceros affinis* (measurements of two samples in liquid: ^{13}C-labelled and not labelled); a SRS image of deuterium-labelled *P. aeruginosa* cells in blood (data used in FIG. 5j[135]); and a spectrum of the pure compound polyhydroxybutyrate.

Limitations and optimizations

Sensitivity

Normal Raman scattering has an inherently low quantum efficiency. To illustrate, laser-irradiated samples scatter most photons elastically by Rayleigh scattering with no frequency shift (FIG. 1a,c). Only about 1 in 10^6 of the laser's photons produces a Raman-scattered photon with frequency shifts. Therefore, optimization of the instrument and sample preparation are

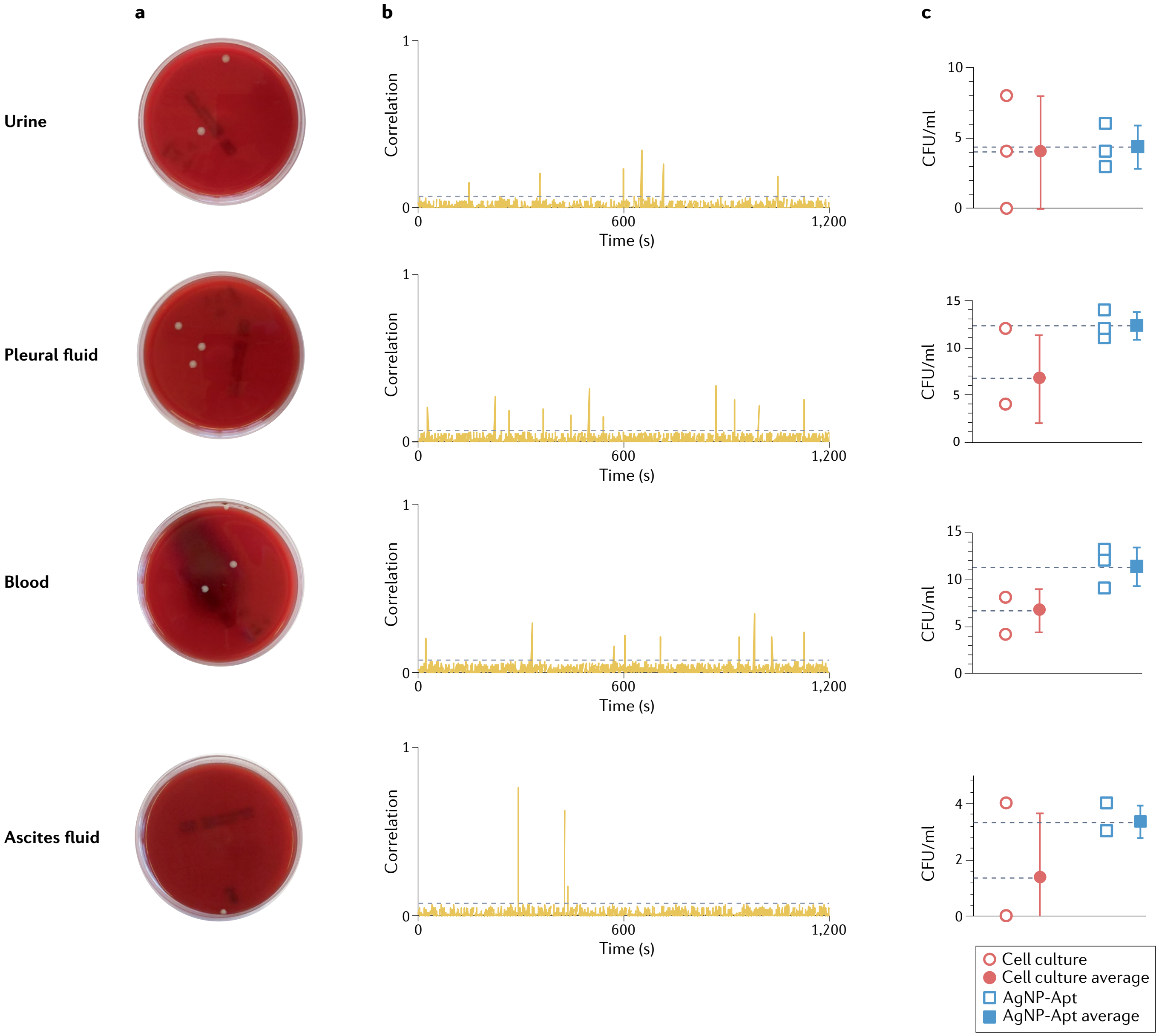

Fig. 7 | **Use of SERS tags for the quantification of the pathogen *Staphylococcus aureus* in various biofluids.** **a** | Illustrations of the conventional method whereby samples from different fluids are spread on blood agar plates and cultured before quantification of the number of colony-forming units (CFU). **b** | Quantification of the pathogen for 20 min using surface-enhanced Raman spectroscopy (SERS) tags (silver nanoparticles encoded with 4-mercaptobenzoic acid (MBA) and then conjugated with aptamers) in an engineered microfluidic device. The SERS signals were measured in the middle of a straight channel where the sample fluid was introduced. The measured SERS spectra were normalized by a reference SERS spectrum. **c** | Comparison between estimates of pathogen concentration based on cell culture (red circles) and based on SERS tags (blue squares). Filled symbols show the averages over three replicates. AgNP-Apt, silver nanoparticle with aptamer. Adapted with permission from REF.[182], Wiley.

essential to capture these relatively rare scattering events. Recommendations for optimization and alternative methods for signal amplification are presented above and in Supplementary Note 1. Efficient and reproducible spectral processing is just as crucial.

Specificity

Raman microspectroscopy is an incredibly powerful tool that provides structural fingerprints to identify many specific molecules in compositionally simple samples such as pure or nearly pure liquids, crystals or gases. However, microorganisms are anything but compositionally simple and thus the Raman spectra of cells often reveal little more than the presence of general classes of biomolecules. A subset of specific compounds can routinely be identified from a single-cell spectrum, for example, phenylalanine, adenine and thymine. When present in relatively high concentrations, storage products[189], such as polyhydroxyalkanoates, polysaccharides, polyphosphates, sulfur inclusions and fatty acids, can also be easily identified from cellular Raman spectra[12,189,190]. If highly abundant, their spectral features may mask fingerprints of other cellular constituents of interest, thereby complicating spectral interpretation. Recognition of many specific molecules within a cell is beyond the reach of Raman microspectroscopy, because many different compounds share the same chemical bond types and consequently share a vibrational mode. In addition, different bonds within the complex cellular matrix can have overlapping vibrational energy distributions, resulting in broad hybrid peaks that are challenging to disentangle. Therefore, careful selection of diagnostic molecules and experimental conditions is essential to ensure meaningful and reproducible results, as amply demonstrated in studies described above.

Fluorescence

When present, laser-induced fluorescence produced by cellular chromophores can overwhelm normal Raman emissions, because fluorescence quantum efficiencies exceed those of normal Raman scattering by orders of magnitude. Thus, Raman spectral features can be masked by broad and intense fluorescence emissions over the entire Raman spectral range (see REF.[122]). This issue can be resolved by multiple approaches, some of which require specific instrumentation or multiple lasers. Most fluorescence avoidance or compensation methods capitalize on differences in the optical behaviours of Raman and fluorescence excitation and emission radiation and are reviewed elsewhere[122,191].

To address this issue using a standard confocal Raman microspectrophotometer, fluorescence can be suppressed at a single spot or cell by exposure to a focused laser beam for a few minutes before spectral acquisition[62]. However, using this approach for surveys of multiple targets in a single sample can lead to unacceptably long data acquisition times. Prolonged data acquisition increases the likelihood of both sample degradation and instrumental instabilities while hampering data throughput and increasing analytical costs. Preparatory protocols (for example, chemiphotobleaching[122,192,193]) that irreversibly suppress fluorescence in an entire biological sample can accelerate data acquisition.

Outlook

In this Primer, we outline approaches in contemporary Raman microspectroscopy, from fundamental and advanced technical configurations, experimental considerations for successful measurement of samples, to methodology for the handling and analysis of Raman data. We also provide an overview of the scope of potential applications in microbiology and microbial ecology, such as interrogation of microbial metabolites, the biochemical currency of interactions between coexisting partners and identification of microorganisms performing functions of interest. We anticipate that, by providing microbiologists with chemometric information at a scale relevant to microorganisms, Raman microspectroscopy will become a breakthrough technology, opening a myriad of avenues of study that will deepen our understanding of the physiology and ecology of the microorganisms that populate the complex microbial tree of life. With a growing community of microbiologists applying these approaches to their work, we predict that Raman microspectroscopy may soon become the tool of choice for certain aspects of microbiology.

There is of course significant room for further improvements. We here outline three directions that hold promise in the near future.

Increasing sensitivity

There are further opportunities to leverage recent innovations in Raman technology and apply them as a way to interrogate cell ecophysiology and metabolic exchange between symbionts. The ability to perform label-free, non-destructive and in situ measurements of samples is a unique and extremely valuable feature of Raman microspectroscopy over alternative techniques such as nanoSIMS[4–7], cryo-EM[8,9] and fluorescence-based methods[194–197]. Raman measurements suffer from a lack of sensitivity that stems directly from the nature of Raman scattering. To overcome this limitation, measurement of dry samples has been used to enhance sensitivity, but with the loss of functionality from live cell measurements. Advances in sensitivity resulting from improved detectors and resolution from the super-resolution concept[198–200] hold promise to enable investigation of extremely dilute bio-analytes.

State-of-the-art Raman systems can also contribute to resolving this issue. For example, time-gated Raman spectroscopy[201] holds great potential, particularly for investigations of photoautotrophic microorganisms and heterotrophs that contain resonance-inducing pigments, such as carotenoids. In the presence of resonance-inducing substances, measurements of other cellular components are typically masked by fluorescence signals that often accompany the resonance Raman scattering (FIG. 5c). Use of laser wavelengths that do not induce resonance is not always possible, and bleaching techniques such as hydrogen peroxide[122] sacrifice the ability to perform live cell interrogations. Time-gated Raman microspectroscopy, by taking advantage of the time difference in the generation of Raman and fluorescence signals[202,203], enables simultaneous measurements of resonance-inducing substances via the accompanying fluorescence, as well as other non-resonant cellular compounds, providing comprehensive molecular information for any type of microorganism.

Intelligent Raman

In many fields, artificial intelligence is proving to be a game changer for handling data[204]. This is also true in Raman microspectroscopy. Machine learning can provide an efficient means to detect slight variation in spectral shape in series of time-resolved measurements or between measurements of different species[106,205–210]. Machine learning can also improve the precision and sensitivity of conventional convolution/deconvolution methods to identify individual microorganisms or chemicals within a spectrum in which multiple cells or compounds are simultaneously measured[106,205–210].

Comprehensive measurements of molecular composition of samples and identification of unknown biochemical compounds may eventually become feasible.

Chromophore
A region of a molecule where the energy difference between two molecular orbitals is within the visible spectrum, thus determining the colour of the molecule.

For example, there have been a few case studies in which machine-learning platforms have been trained using Raman spectra of diverse types of pathogenic bacteria and were then able to successfully assign newly measured data to closely related groups[106,211,212]. By contrast, Raman microspectroscopy has rarely been applied in microbiology for naive identification or measurement of unknown biochemical compounds. A likely reason might be a lack of comparative data for biological Raman measurements, and may be partly due to limited sensitivity. In this regard, a central data repository should develop into a comprehensive database, laying the foundations for improvement of identification techniques for diverse applications.

Adoption in unexploited fields

The greatest strength of Raman microspectroscopy lies not in any specific aspect of the technology itself, but in its versatile and robust nature. Bacteria live in a world in which chemical signals have a predominant role in their ecology, and any approach that allows microbiologists to probe this world in a dynamic fashion has enormous implications. There is huge potential for adoption of Raman microspectroscopy in underexploited areas of environmental microbiology. For instance, biomineralization is a prime field for widespread adoption, as crystalline solids are often sources of strong Raman scattering. Within this field, Raman has been used to profile several mineralization processes[213–215] with consequences for nano- and biotechnology. Electro-microbiology, an emerging field, has already applied Raman microspectroscopy in a unique and beautiful way to confirm the ability of cable bacteria to couple the oxidation of sulfide to the reduction of oxygen over long distances[147] and we expect more studies to follow. The study of environmental microplastics is also especially well suited to Raman microspectroscopic analyses[216], and cross-disciplinary research that addresses the role of microorganisms in the degradation of microplastics in the environment should see further adoption[217,218].

Although much microbiological research is currently limited to the laboratory, in the near future Raman microspectroscopy could help establish coherent links between in situ field monitoring and more closely controlled laboratory studies. Raman field samplers have already been successfully deployed in diverse — and sometimes quite extreme — environments of microbial relevance. Automated Raman profilers have been integrated into advanced oceanographic sampling equipment, such as remotely operated vehicles[219] and deployed to hydrothermal vents[220]. Raman profilers are now standard equipment on unmanned space probes, with the technology currently integrated into the European Space Agency's Rosalind Franklin and NASA's Perseverance Mars rovers[22,221–225]. These devices are being deployed with the express intent of looking for signatures of past or present biological life in the form of cellular biomass[22], large carbon deposits or high enantiomeric and isotopic ratios in possible biogenic compounds, as one justification for their inclusion[221]. Use of these types of sensor in environmental monitoring applications is likely to greatly accelerate the widespread adoption of Raman microspectroscopy by environmental microbiologists.

Additional biotechnological applications are already emerging in the booming field of synthetic biology. As many synthetic biology approaches now rely, to some degree, on directed evolution[226,227], rapid screening of new cell lines for production of natural products or enhanced enzymatic activity is increasingly important[228]. Much of this screening is currently being performed using labour-intensive methods such as mass spectrometry. Owing to its easy integration with other laboratory approaches, in particular droplet microfluidics[229–231], Raman microspectroscopy provides distinct advantages in methodology and cost.

Conclusion

Despite its long and established history in the physical sciences, it is possible that the age of utility for Raman microspectroscopy is only just beginning. The continuing boom in new omics technologies has given us the tools to map or identify nearly any latent feature potentially effecting microbially controlled processes but there remains a dearth of techniques that allow us to investigate the actualization of these processes without destructive sampling or violent disruption of the sample. Raman microspectroscopy is unique not only in its broad utility as a tool for investigating chemical aspects of microbial metabolism, it stands (nearly) alone in its ability to do so in situ. From this standpoint alone, we predict that Raman microspectroscopy should see widespread adoption in the near future, particularly as technical aspects of the approach improve.

1. Raman, C. V. & Krishnan, K. S. A new type of secondary radiation. *Nature* **121**, 501–502 (1928).
2. Baker, M. J. et al. Using Fourier transform IR spectroscopy to analyze biological materials. *Nat. Protoc.* **9**, 1771–1791 (2014).
3. Movasaghi, Z., Rehman, S. & Rehman, I. U. Fourier transform infrared (FTIR) spectroscopy of biological tissues. *Appl. Spectrosc. Rev.* **43**, 134–179 (2008).
4. Wagner, M. Single-cell ecophysiology of microbes as revealed by Raman microspectroscopy or secondary ion mass spectrometry imaging. *Annu. Rev. Microbiol.* **63**, 411–429 (2009).
5. Li, T. et al. Simultaneous analysis of microbial identity and function using NanoSIMS. *Environ. Microbiol.* **10**, 580–588 (2008).
6. Nuñez, J., Renslow, R., Cliff, J. B. & Anderton, C. R. NanoSIMS for biological applications: current practices and analyses. *Biointerphases* **13**, 03B301 (2018).
7. Musat, N., Foster, R., Vagner, T., Adam, B. & Kuypers, M. M. M. Detecting metabolic activities in single cells, with emphasis on nanoSIMS. *FEMS Microbiol. Rev.* **36**, 486–511 (2012).
8. Weissenberger, G., Henderikx, R. J. M. & Peters, P. J. Understanding the invisible hands of sample preparation for cryo-EM. *Nat. Methods* **18**, 463–471 (2021).
9. Oikonomou, C. M., Chang, Y.-W. & Jensen, G. J. A new view into prokaryotic cell biology from electron cryotomography. *Nat. Rev. Microbiol.* **14**, 205–220 (2016).
10. Wakisaka, Y. et al. Probing the metabolic heterogeneity of live *Euglena gracilis* with stimulated Raman scattering microscopy. *Nat. Microbiol.* **1**, 16124 (2016).
11. Barletta, R. E., Krause, J. W., Goodie, T. & El Sabae, H. The direct measurement of intracellular pigments in phytoplankton using resonance Raman spectroscopy. *Mar. Chem.* **176**, 164–173 (2015).
12. Moudříková, Š. et al. Raman and fluorescence microscopy sensing energy-transducing and energy-storing structures in microalgae. *Algal Res.* **16**, 224–232 (2016).
13. Heraud, P., Beardall, J., McNaughton, D. & Wood, B. R. *In vivo* prediction of the nutrient status of individual microalgal cells using Raman microspectroscopy. *FEMS Microbiol. Lett.* **275**, 24–30 (2007).
14. Rüger, J. et al. Assessment of growth phases of the diatom *Ditylum brightwellii* by FT-IR and Raman spectroscopy. *Algal Res.* **19**, 246–252 (2016).
15. Alexandre, M. T. A. et al. Probing the carotenoid content of intact *Cyclotella* cells by resonance Raman spectroscopy. *Photosynth. Res.* **119**, 273–281 (2014).
16. Premvardhan, L., Bordes, L., Beer, A., Büchel, C. & Robert, B. Carotenoid structures and environments in trimeric and oligomeric fucoxanthin chlorophyll a/c_2

proteins from resonance Raman spectroscopy. *J. Phys. Chem. B* **113**, 12565–12574 (2009).

17. Büchel, C. How diatoms harvest light. *Science* **365**, 447–448 (2019).
18. Dolinšek, J., Lagkouvardos, I., Wanek, W., Wagner, M. & Daims, H. Interactions of nitrifying bacteria and heterotrophs: identification of a *Micavibrio*-like putative predator of *Nitrospira* spp. *Appl. Environ. Microbiol.* **79**, 2027–2037 (2013).
19. Shao, F. & Zenobi, R. Tip-enhanced Raman spectroscopy: principles, practice, and applications to nanospectroscopic imaging of 2D materials. *Anal. Bioanal. Chem.* **411**, 37–61 (2019).
20. Yeo, B.-S., Stadler, J., Schmid, T., Zenobi, R. & Zhang, W. Tip-enhanced Raman Spectroscopy–Its status, challenges and future directions. *Chem. Phys. Lett.* **472**, 1–13 (2009).
21. Mosca, S., Conti, C., Stone, N. & Matousek, P. Spatially offset Raman spectroscopy. *Nat. Rev. Methods Prim.* **1**, 21 (2021).
22. Sapers, H. M. et al. The cell and the sum of its parts: patterns of complexity in biosignatures as revealed by deep UV Raman spectroscopy. *Front. Microbiol.* **10**, 679 (2019).
23. Nelson, W. H., Manoharan, R. & Sperry, J. F. UV resonance Raman studies of bacteria. *Appl. Spectrosc. Rev.* **27**, 67–124 (1992).
24. Wu, Q. et al. UV Raman spectral intensities of *E. coli* and other bacteria excited at 228.9, 244.0, and 248.2 nm. *Anal. Chem.* **73**, 3432–3440 (2001).
25. Jarvis, R. M. & Goodacre, R. Ultra-violet resonance Raman spectroscopy for the rapid discrimination of urinary tract infection bacteria. *FEMS Microbiol. Lett.* **232**, 127–132 (2004).
26. Žukovskaja, O. et al. UV-Raman spectroscopic identification of fungal spores important for respiratory diseases. *Anal. Chem.* **90**, 8912–8918 (2018).
27. Boustany, N. N., Manoharan, R., Dasari, R. R. & Feld, M. S. Ultraviolet resonance Raman spectroscopy of bulk and microscopic human colon tissue. *Appl. Spectrosc.* **54**, 24–30 (2000).
28. Kumamoto, Y., Taguchi, A., Smith, N. I. & Kawata, S. Deep ultraviolet resonant Raman imaging of a cell. *J. Biomed. Opt.* **17**, 076001 (2012).
29. Kneipp, J., Kneipp, H. & Kneipp, K. SERS — a single-molecule and nanoscale tool for bioanalytics. *Chem. Soc. Rev.* **37**, 1052–1060 (2008).
30. Langer, J. et al. Present and future of surface-enhanced Raman scattering. *ACS Nano* **14**, 28–117 (2020).
31. Lussier, F. et al. Dynamic-SERS optophysiology: a nanosensor for monitoring cell secretion events. *Nano Lett.* **16**, 3866–3871 (2016).
32. Caprettini, V. et al. Enhanced Raman investigation of cell membrane and intracellular compounds by 3D plasmonic nanoelectrode arrays. *Adv. Sci.* **5**, 1800560 (2018).
33. Efrima, S. & Bronk, B. V. Silver colloids impregnating or coating bacteria. *J. Phys. Chem. B* **102**, 5947–5950 (1998).
34. Zhou, H. et al. SERS detection of bacteria in water by in situ coating with Ag nanoparticles. *Anal. Chem.* **86**, 1525–1533 (2014).
35. Drescher, D., Traub, H., Büchner, T., Jakubowski, N. & Kneipp, J. Properties of *in situ* generated gold nanoparticles in the cellular context. *Nanoscale* **9**, 11647–11656 (2017).
    Demonstration of the fabrication of SERS substrates in a cellular environment in situ.
36. Palanco, M. E. et al. Templated green synthesis of plasmonic silver nanoparticles in onion epidermal cells suitable for surface-enhanced Raman and hyper-Raman scattering. *Beilstein J. Nanotechnol.* **7**, 834–840 (2016).
37. Weiss, R. et al. Surface-enhanced Raman spectroscopy of microorganisms: limitations and applicability on the single-cell level. *Analyst* **144**, 943–953 (2019).
38. Premasiri, W. R. et al. The biochemical origins of the surface-enhanced Raman spectra of bacteria: a metabolomics profiling by SERS. *Anal. Bioanal. Chem.* **408**, 4631–4647 (2016).
39. Wang, Y., Yan, B. & Chen, L. SERS tags: novel optical nanoprobes for bioanalysis. *Chem. Rev.* **113**, 1391–1428 (2013).
40. Kelley, A. M. Hyper-Raman scattering by molecular vibrations. *Annu. Rev. Phys. Chem.* **61**, 41–61 (2010).
41. Helmchen, F. & Denk, W. Deep tissue two-photon microscopy. *Nat. Methods* **2**, 932–940 (2005).
42. Madzharova, F., Heiner, Z. & Kneipp, J. Surface enhanced hyper Raman scattering (SEHRS) and its applications. *Chem. Soc. Rev.* **46**, 3980–3999 (2017).
43. Kneipp, J., Kneipp, H. & Kneipp, K. Two-photon vibrational spectroscopy for biosciences based on surface-enhanced hyper-Raman scattering. *Proc. Natl Acad. Sci. USA* **103**, 17149–17153 (2006).
    Application of HRS for the detection of complementary peaks of biomolecules and cells.
44. Heiner, Z., Gühlke, M., Živanović, V., Madzharova, F. & Kneipp, J. Surface-enhanced hyper Raman hyperspectral imaging and probing in animal cells. *Nanoscale* **9**, 8024–8032 (2017).
45. Zhang, C., Zhang, D. & Cheng, J.-X. Coherent Raman scattering microscopy in biology and medicine. *Annu. Rev. Biomed. Eng.* **17**, 415–445 (2015).
46. Min, W., Freudiger, C. W., Lu, S. & Xie, X. S. Coherent nonlinear optical imaging: Beyond fluorescence microscopy. *Annu. Rev. Phys. Chem.* **62**, 507–530 (2011).
47. Zhang, D., Wang, P., Slipchenko, M. N. & Cheng, J.-X. Fast vibrational imaging of single cells and tissues by stimulated Raman scattering microscopy. *Acc. Chem. Res.* **47**, 2282–2290 (2014).
48. Freudiger, C. W. et al. Label-free biomedical imaging with high sensitivity by stimulated Raman scattering microscopy. *Science* **322**, 1857–1861 (2008).
49. Yue, S. & Cheng, J.-X. Deciphering single cell metabolism by coherent Raman scattering microscopy. *Curr. Opin. Chem. Biol.* **33**, 46–57 (2016).
50. Suzuki, Y. et al. Label-free chemical imaging flow cytometry by high-speed multicolor stimulated Raman scattering. *Proc. Natl Acad. Sci. USA* **116**, 15842–15848 (2019).
    Development of a high-throughput Raman-based flow cell counter for microalgae based on multicolour-SRS microscopy and deep learning.
51. De la Cadena, A., Valensise, C. M., Marangoni, M., Cerullo, G. & Polli, D. Broadband stimulated Raman scattering microscopy with wavelength-scanning detection. *J. Raman Spectrosc.* **51**, 1951–1959 (2020).
52. Lu, F.-K. et al. Multicolor stimulated Raman scattering microscopy. *Mol. Phys.* **110**, 1927–1932 (2012).
53. Choquette, S. J., Etz, E. S., Hurst, W. S., Blackburn, D. H. & Leigh, S. D. Relative intensity correction of Raman spectrometers: NIST SRMs 2241 through 2243 for 785 nm, 532 nm, and 488 nm/514.5 nm excitation. *Appl. Spectrosc.* **61**, 117–129 (2007).
54. Sui, Z., Leong, P. P., Herman, I. P., Higashi, G. S. & Temkin, H. Raman analysis of light-emitting porous silicon. *Appl. Phys. Lett.* **60**, 2086–2088 (1992).
55. Ivleva, N. P., Wagner, M., Horn, H., Niessner, R. & Haisch, C. Raman microscopy and surface-enhanced Raman scattering (SERS) for in situ analysis of biofilms. *J. Biophotonics* **3**, 548–556 (2010).
56. Ivleva, N. P., Kubryk, P. & Niessner, R. Raman microspectroscopy, surface-enhanced Raman scattering microspectroscopy, and stable-isotope Raman microspectroscopy for biofilm characterization. *Anal. Bioanal. Chem.* **409**, 4353–4375 (2017).
57. Gruber-Vodicka, H. R. et al. *Paracatenula*, an ancient symbiosis between thiotrophic Alphaproteobacteria and catenulid flatworms. *Proc. Natl Acad. Sci. USA* **108**, 12078–12083 (2011).
58. Bustamante, C. J., Chemla, Y. R., Liu, S. & Wang, M. D. Optical tweezers in single-molecule biophysics. *Nat. Rev. Methods Prim.* **1**, 25 (2021).
59. Ashkin, A. & Dziedzic, J. M. Optical trapping and manipulation of viruses and bacteria. *Science* **235**, 1517–1520 (1987).
60. Ashkin, A. Forces of a single-beam gradient laser trap on a dielectric sphere in the ray optics regime. *Biophys. J.* **61**, 569–582 (1992).
61. Lee, K. S. et al. Optofluidic Raman-activated cell sorting for targeted genome retrieval or cultivation of microbial cells with specific functions. *Nat. Protoc.* **16**, 634–676 (2021).
62. Huang, W. E. et al. Raman-FISH: combining stable-isotope Raman spectroscopy and fluorescence *in situ* hybridization for the single cell analysis of identity and function. *Environ. Microbiol.* **9**, 1878–1889 (2007).
    First demonstration of the combination of FISH, SIP and Raman microspectroscopy.
63. Lee, K. S. et al. An automated Raman-based platform for the sorting of live cells by functional properties. *Nat. Microbiol.* **4**, 1035–1048 (2019).
    Sorting of microbial cells in terms of their functional properties (phenotypes) using confocal Raman microspectroscopy, optical tweezers, SIP and microfluidics, which enables linking of cell function to their genome through downstream DNA analysis, as well as cultivation for further ecological evaluation.
64. Read, D. S. & Whiteley, A. S. Chemical fixation methods for Raman spectroscopy-based analysis of bacteria. *J. Microbiol. Methods* **109**, 79–83 (2015).
65. García-Timermans, C. et al. Label-free Raman characterization of bacteria calls for standardized procedures. *J. Microbiol. Methods* **151**, 69–75 (2018).
66. Behrendt, L. et al. PhenoChip: a single-cell phenomic platform for high-throughput photophysiological analyses of microalgae. *Sci. Adv.* **6**, eabb2754 (2020).
67. Collins, D. J. et al. Two-dimensional single-cell patterning with one cell per well driven by surface acoustic waves. *Nat. Commun.* **6**, 8686 (2015).
68. Taylor, G. T. et al. Single-cell growth rates in photoautotrophic populations measured by stable isotope probing and resonance Raman microspectrometry. *Front. Microbiol.* **8**, 1449 (2017).
    Growth rate measurements of photoautotrophic microorganisms (*Synechococcus* sp. and *Thalassiosira pseudonana*) by coupling ^{13}C SIP and single-cell resonance Raman microspectroscopy.
69. Pereira, F. C. et al. Rational design of a microbial consortium of mucosal sugar utilizers reduces *Clostridioides difficile* colonization. *Nat. Commun.* **11**, 5104 (2020).
    Application of a high-throughput optofluidic RACS platform and mini-metagenomics to identify mucosal sugar degraders within gut microbiota and use of this information to rationally design a probiotic mixture of microorganisms that could reduce pathogen colonization.
70. Berry, D. et al. Tracking heavy water (D_2O) incorporation for identifying and sorting active microbial cells. *Proc. Natl Acad. Sci. USA* **112**, E194–E203 (2015).
    First study combining deuterium labelling, RACS and 16S ribosomal RNA gene sequencing, which together led to the identification of novel glucosamine- and mucin-utilizing bacteria from mouse gut microbiota.
71. Xu, T. et al. Phenome–genome profiling of single bacterial cell by Raman-activated gravity-driven encapsulation and sequencing. *Small* **16**, 2001172 (2020).
72. Wang, X. et al. Positive dielectrophoresis-based Raman-activated droplet sorting for culture-free and label-free screening of enzyme function in vivo. *Sci. Adv.* **6**, eabb3521 (2020).
73. Czamara, K. et al. Raman spectroscopy of lipids: a review. *J. Raman Spectrosc.* **46**, 4–20 (2015).
74. Wang, Y., Huang, W. E., Cui, L. & Wagner, M. Single cell stable isotope probing in microbiology using Raman microspectroscopy. *Curr. Opin. Biotechnol.* **41**, 34–42 (2016).
75. Li, M., Ashok, P. C., Dholakia, K. & Huang, W. E. Raman-activated cell counting for profiling carbon dioxide fixing microorganisms. *J. Phys. Chem. A* **116**, 6560–6563 (2012).
76. Li, M. et al. Rapid resonance Raman microspectroscopy to probe carbon dioxide fixation by single cells in microbial communities. *ISME J.* **6**, 875–885 (2012).
77. Li, M., Huang, W. E., Gibson, C. M., Fowler, P. W. & Jousset, A. Stable isotope probing and Raman spectroscopy for monitoring carbon flow in a food chain and revealing metabolic pathway. *Anal. Chem.* **85**, 1642–1649 (2013).
78. Wang, Y. et al. Reverse and multiple stable isotope probing to study bacterial metabolism and interactions at the single cell level. *Anal. Chem.* **88**, 9443–9450 (2016).
79. Cui, L., Butler, H. J., Martin-Hirsch, P. L. & Martin, F. L. Aluminium foil as a potential substrate for ATR-FTIR, transflection FTIR or Raman spectrochemical analysis of biological specimens. *Anal. Methods* **8**, 481–487 (2016).
80. Cui, L., Yang, K., Zhou, G., Huang, W. E. & Zhu, Y.-G. Surface-enhanced Raman spectroscopy combined with stable isotope probing to monitor nitrogen assimilation at both bulk and single-cell level. *Anal. Chem.* **89**, 5793–5800 (2017).
81. Fernando, E. Y. et al. Resolving the individual contribution of key microbial populations to enhanced biological phosphorus removal with Raman–FISH. *ISME J.* **13**, 1933–1946 (2019).
    Application of FISH–Raman to quantify the amount of polyphosphate in various microbial taxa in wastewater treatment plants, showing that *Tetrasphaera* have a more important role in enhanced biological phosphorus removal than previously thought.
82. Grosser, K. et al. Disruption-free imaging by Raman spectroscopy reveals a chemical sphere with antifouling metabolites around macroalgae. *Biofouling* **28**, 687–696 (2012).

83. Gautam, R., Vanga, S., Ariese, F. & Umapathy, S. Review of multidimensional data processing approaches for Raman and infrared spectroscopy. *EPJ Tech. Instrum.* **2**, 8 (2015).
84. Byrne, H. J., Knief, P., Keating, M. E. & Bonnier, F. Spectral pre and post processing for infrared and Raman spectroscopy of biological tissues and cells. *Chem. Soc. Rev.* **45**, 1865–1878 (2016).
85. Savitzky, A. & Golay, M. J. E. Smoothing and differentiation of data by simplified least square procedures. *Anal. Chem.* **36**, 1627–1639 (1964).
86. Schafer, R. W. What is a Savitzky-Golay filter? *IEEE Signal. Process. Mag.* **28**, 111–117 (2011).
87. Quintero, L., Matthäus, C., Hunt, S. & Diem, M. Denoising of single scan Raman spectroscopy signals. *Imaging, Manip., Anal., Biomol., Cells, Tissues VIII* **7568**, 756817 (2010).
88. Ehrentreich, F. & Sümmchen, L. Spike removal and denoising of Raman spectra by wavelet transform methods. *Anal. Chem.* **73**, 4364–4373 (2001).
89. Ehrentreich, F. Wavelet transform applications in analytical chemistry. *Anal. Bioanal. Chem.* **372**, 115–121 (2002).
90. Silveira, L., Bodanese, B., Zangaro, R. A. & Pacheco, M. T. T. Discrete wavelet transform for denoising Raman spectra of human skin tissues used in a discriminant diagnostic algorithm. *Instrum. Sci. Technol.* **38**, 268–282 (2010).
91. Lieber, C. A. & Mahadevan-Jansen, A. Automated method for subtraction of fluorescence from biological Raman spectra. *Appl. Spectrosc.* **57**, 1363–1367 (2003).
92. Zhao, J., Lui, H., McLean, D. I. & Zeng, H. Automated autofluorescence background subtraction algorithm for biomedical Raman spectroscopy. *Appl. Spectrosc.* **61**, 1225–1232 (2007).
93. Eilers, P. H. C. & Boelens, H. F. M. Baseline correction with asymmetric least squares smoothing. *Leiden. Univ. Med. Cent. Rep.* **1**, 1–5 (2005).
94. Lasch, P. Spectral pre-processing for biomedical vibrational spectroscopy and microspectroscopic imaging. *Chemom. Intell. Lab. Syst.* **117**, 100–114 (2012).
95. Afseth, N. K., Segtnan, V. H. & Wold, J. P. Raman spectra of biological samples: a study of preprocessing methods. *Appl. Spectrosc.* **60**, 1358–1367 (2006).
96. de Groot, P. J. et al. Application of principal component analysis to detect outliers and spectral deviations in near-field surface-enhanced Raman spectra. *Anal. Chim. Acta* **446**, 71–83 (2001).
97. Liu, X.-Y. et al. Spatiotemporal organization of biofilm matrix revealed by confocal Raman mapping integrated with non-negative matrix factorization analysis. *Anal. Chem.* **92**, 707–715 (2020).
98. Schumacher, W., Stöckel, S., Rösch, P. & Popp, J. Improving chemometric results by optimizing the dimension reduction for Raman spectral data sets. *J. Raman Spectrosc.* **45**, 930–940 (2014).
99. Shashilov, V. A., Xu, M., Ermolenkov, V. V. & Lednev, I. K. Latent variable analysis of Raman spectra for structural characterization of proteins. *J. Quant. Spectrosc. Radiat. Transf.* **102**, 46–61 (2006).
100. Lee, T.-W. *Independent Component Analysis: Theory and Applications* (Springer, 1998).
101. Piraino, P., Ricciardi, A., Salzano, G., Zotta, T. & Parente, E. Use of unsupervised and supervised artificial neural networks for the identification of lactic acid bacteria on the basis of SDS-PAGE patterns of whole cell proteins. *J. Microbiol. Methods* **66**, 336–346 (2006).
102. Schmid, U. et al. Gaussian mixture discriminant analysis for the single-cell differentiation of bacteria using micro-Raman spectroscopy. *Chemom. Intell. Lab. Syst.* **96**, 159–171 (2009).
103. Prochazka, D. et al. Combination of laser-induced breakdown spectroscopy and Raman spectroscopy for multivariate classification of bacteria. *Spectrochim. Acta B At. Spectrosc.* **139**, 6–12 (2018).
104. Kloβ, S. et al. Destruction-free procedure for the isolation of bacteria from sputum samples for Raman spectroscopic analysis. *Anal. Bioanal. Chem.* **407**, 8333–8341 (2015).
105. Hlaing, M. M., Dunn, M., Stoddart, P. R. & McArthur, S. L. Raman spectroscopic identification of single bacterial cells at different stages of their lifecycle. *Vib. Spectrosc.* **86**, 81–89 (2016).
106. Ho, C.-S. et al. Rapid identification of pathogenic bacteria using Raman spectroscopy and deep learning. *Nat. Commun.* **10**, 4927 (2019).
    Application of Raman spectroscopy and deep learning to identify 30 common bacterial pathogens with high accuracy (up to 97%).
107. Živanović, V. et al. Optical nanosensing of lipid accumulation due to enzyme inhibition in live cells. *ACS Nano* **13**, 9363–9375 (2019).
108. van de Schoot, R. et al. Bayesian statistics and modelling. *Nat. Rev. Methods Prim.* **1**, 1 (2021).
109. Rebrošová, K. et al. Rapid identification of staphylococci by Raman spectroscopy. *Sci. Rep.* **7**, 14846 (2017).
110. Gaus, K. et al. Classification of lactic acid bacteria with UV-resonance Raman spectroscopy. *Biopolymers* **82**, 286–290 (2006).
111. Rösch, P. et al. Chemotaxonomic identification of single bacteria by micro-Raman spectroscopy: application to clean-room-relevant biological contaminations. *Appl. Environ. Microbiol.* **71**, 1626–1637 (2005).
    First study identifying single bacteria without cultivation using Raman spectroscopy.
112. Errington, J. Regulation of endospore formation in *Bacillus subtilis*. *Nat. Rev. Microbiol.* **1**, 117–126 (2003).
113. Huang, S.-S. et al. Levels of Ca^{2+}-dipicolinic acid in individual *Bacillus* spores determined using microfluidic Raman tweezers. *J. Bacteriol.* **189**, 4681–4687 (2007).
114. Xu, J., Webb, I., Poole, P. & Huang, W. E. Label-free discrimination of rhizobial bacteroids and mutants by single-cell Raman microspectroscopy. *Anal. Chem.* **89**, 6336–6340 (2017).
115. Ng, C. K. et al. Elevated intracellular cyclic-di-GMP level in *Shewanella oneidensis* increases expression of *c*-type cytochromes. *Microb. Biotechnol.* **13**, 1904–1916 (2020).
116. Song, Y. et al. Single-cell genomics based on Raman sorting reveals novel carotenoid-containing bacteria in the Red Sea. *Microb. Biotechnol.* **10**, 125–137 (2017).
117. Jing, X. et al. Raman-activated cell sorting and metagenomic sequencing revealing carbon-fixing bacteria in the ocean. *Environ. Microbiol.* **20**, 2241–2255 (2018).
118. Song, Y. et al. Proteorhodopsin overproduction enhances the long-term viability of *Escherichia coli*. *Appl. Environ. Microbiol.* **86**, e02087-19 (2020).
119. Carey, P. R. *Biochemical Applications of Raman and Resonance Raman Spectroscopies* (Academic Press, 1982).
120. Takano, H. The regulatory mechanism underlying light-inducible production of carotenoids in nonphototrophic bacteria. *Biosci. Biotechnol. Biochem.* **80**, 1264–1273 (2016).
121. Wang, W. et al. Structural basis for blue-green light harvesting and energy dissipation in diatoms. *Science* **363**, eaav0365 (2019).
122. Yakubovskaya, E., Zaliznyak, T., Martínez Martínez, J. & Taylor, G. T. Tear down the fluorescent curtain: a new fluorescence suppression method for Raman microspectroscopic analyses. *Sci. Rep.* **9**, 15785 (2019).
123. Vogt, C. et al. Stable isotope probing approaches to study anaerobic hydrocarbon degradation and degraders. *J. Mol. Microbiol. Biotechnol.* **26**, 195–210 (2016).
124. van Manen, H.-J., Lenferink, A. & Otto, C. Noninvasive imaging of protein metabolic labeling in single human cells using stable isotopes and Raman microscopy. *Anal. Chem.* **80**, 9576–9582 (2008).
125. Xu, J. et al. Raman deuterium isotope probing reveals microbial metabolism at the single-cell level. *Anal. Chem.* **89**, 13305–13312 (2017).
126. Olaniyi, O. O., Yang, K., Zhu, Y.-G. & Cui, L. Heavy water-labeled Raman spectroscopy reveals carboxymethylcellulose-degrading bacteria and degradation activity at the single-cell level. *Appl. Microbiol. Biotechnol.* **103**, 1455–1464 (2019).
127. Huang, W. E. et al. Resolving genetic functions within microbial populations: In situ analyses using rRNA and mRNA stable isotope probing coupled with single-cell Raman–fluorescence in situ hybridizationδ. *Appl. Environ. Microbiol.* **75**, 234–241 (2009).
128. Singleton, C. M. et al. Connecting structure to function with the recovery of over 1000 high-quality metagenome-assembled genomes from activated sludge using long-read sequencing. *Nat. Commun.* **12**, 2009 (2021).
129. Milucka, J. et al. Zero-valent sulphur is a key intermediate in marine methane oxidation. *Nature* **491**, 541–546 (2012).
130. Schmid, T., Messmer, A., Yeo, B.-S., Zhang, W. & Zenobi, R. Towards chemical analysis of nanostructures in biofilms II: tip-enhanced Raman spectroscopy of alginates. *Anal. Bioanal. Chem.* **391**, 1907–1916 (2008).
131. Madzharova, F., Heiner, Z., Gühlke, M. & Kneipp, J. Surface-enhanced hyper-Raman spectra of adenine, guanine, cytosine, thymine, and uracil. *J. Phys. Chem. C.* **120**, 15415–15423 (2016).
132. Kim, S. K., Joo, T. H., Suh, S. W. & Kim, M. S. Surface-enhanced Raman scattering (SERS) of nucleic acid components in silver sol: adenine series. *J. Raman Spectrosc.* **17**, 381–386 (1986).
133. Feng, F. et al. SERS detection of low-concentration adenine by a patterned silver structure immersion plated on a silicon nanoporous pillar array. *Nanotechnology* **20**, 295501 (2009).
134. Bell, S. E. J. et al. Towards reliable and quantitative surface-enhanced Raman scattering (SERS): from key parameters to good analytical practice. *Angew. Chem. Int. Ed.* **59**, 5454–5462 (2020).
135. Zhang, M. et al. Rapid determination of antimicrobial susceptibility by stimulated Raman scattering imaging of D_2O metabolic incorporation in a single bacterium. *Adv. Sci.* **7**, 2001452 (2020).
    Rapid antimicrobial susceptibility testing based on femtosecond SRS imaging of deuterium incorporation into cells of interest.
136. Karanja, C. W. et al. Stimulated Raman imaging reveals aberrant lipogenesis as a metabolic marker for azole-resistant *Candida albicans*. *Anal. Chem.* **89**, 9822–9829 (2017).
137. Majed, N., Chernenko, T., Diem, M. & Gu, A. Z. Identification of functionally relevant populations in enhanced biological phosphorus removal processes based on intracellular polymers profiles and insights into the metabolic diversity and heterogeneity. *Environ. Sci. Technol.* **46**, 5010–5017 (2012).
138. Li, Y. et al. Toward better understanding of EBPR systems via linking Raman-based phenotypic profiling with phylogenetic diversity. *Environ. Sci. Technol.* **52**, 8596–8606 (2018).
139. Spang, A. et al. The genome of the ammonia-oxidizing *Candidatus* Nitrososphaera gargensis: insights into metabolic versatility and environmental adaptations. *Environ. Microbiol.* **14**, 3122–3145 (2012).
140. Probst, A. J. et al. Biology of a widespread uncultivated archaeon that contributes to carbon fixation in the subsurface. *Nat. Commun.* **5**, 5497 (2014).
141. Hong, W. et al. *In situ* detection of a single bacterium in complex environment by hyperspectral CARS imaging. *ChemistrySelect* **1**, 513–517 (2016).
142. Petrov, G. I. et al. Comparison of coherent and spontaneous Raman microspectroscopies for noninvasive detection of single bacterial endospores. *Proc. Natl Acad. Sci. USA* **104**, 7776–7779 (2007).
143. Arora, R., Petrov, G. I., Yakovlev, V. V. & Scully, M. O. Detecting anthrax in the mail by coherent Raman microspectroscopy. *Proc. Natl Acad. Sci. USA* **109**, 1151–1153 (2012).
144. Hong, W. et al. Antibiotic susceptibility determination within one cell cycle at single-bacterium level by stimulated Raman metabolic imaging. *Anal. Chem.* **90**, 3737–3743 (2018).
145. He, Y., Wang, X., Ma, B. & Xu, J. Ramanome technology platform for label-free screening and sorting of microbial cell factories at single-cell resolution. *Biotechnol. Adv.* **37**, 107388 (2019).
146. Kjeldsen, K. U. et al. On the evolution and physiology of cable bacteria. *Proc. Natl Acad. Sci. USA* **116**, 19116–19125 (2019).
147. Bjerg, J. T. et al. Long-distance electron transport in individual, living cable bacteria. *Proc. Natl Acad. Sci. USA* **115**, 5786–5791 (2018).
    Resonance Raman measurements of cytochrome demonstrates long-distance electron transport over micrometres in cable bacteria.
148. Haider, S. et al. Raman microspectroscopy reveals long-term extracellular activity of chlamydiae. *Mol. Microbiol.* **77**, 687–700 (2010).
    By using Raman microspectroscopy to differentiate developmental stages of chlamydiae and to investigate the physiological activity of these stages by single-cell SIP it could be demonstrated that in contrast to textbook knowledge elementary bodies of *Chlamydia* are physiologically active outside of their host cells — a feature that has important implications for our understanding of the biology of these pathogens.
149. Chen, D., Huang, S.-S. & Li, Y.-Q. Real-time detection of kinetic germination and heterogeneity of single *Bacillus* spores by laser tweezers Raman spectroscopy. *Anal. Chem.* **78**, 6936–6941 (2006).
150. Jäckle, O. et al. Chemosynthetic symbiont with a drastically reduced genome serves as primary energy storage in the marine flatworm *Paracatenula*. *Proc. Natl Acad. Sci. USA* **116**, 8505–8514 (2019).

151. Sharma, K., Palatinszky, M., Nikolov, G., Berry, D. & Shank, E. A. Transparent soil microcosms for live-cell imaging and non-destructive stable isotope probing of soil microorganisms. *eLife* **9**, e56275 (2020).
152. Bodelón, G. et al. Detection and imaging of quorum sensing in *Pseudomonas aeruginosa* biofilm communities by surface-enhanced resonance Raman scattering. *Nat. Mater.* **15**, 1203–1211 (2016). **In situ, label-free identification of the structure of growing biofilms, and of their metabolites involved in intercellular signaling (quorum sensing)**.
153. Sandt, C., Smith-Palmer, T., Pink, J., Brennan, L. & Pink, D. Confocal Raman microspectroscopy as a tool for studying the chemical heterogeneities of biofilms in situ. *J. Appl. Microbiol.* **103**, 1808–1820 (2007).
154. Ivleva, N. P. et al. Label-free in situ SERS imaging of biofilms. *J. Phys. Chem. B* **114**, 10184–10194 (2010).
155. Ivleva, N. P., Wagner, M., Horn, H., Niessner, R. & Haisch, C. Towards a nondestructive chemical characterization of biofilm matrix by Raman microscopy. *Anal. Bioanal. Chem.* **393**, 197–206 (2009).
156. Horiue, H., Sasaki, M., Yoshikawa, Y., Toyofuku, M. & Shigeto, S. Raman spectroscopic signatures of carotenoids and polyenes enable label-free visualization of microbial distributions within pink biofilms. *Sci. Rep.* **10**, 7704 (2020).
157. Schiessl, K. T. et al. Phenazine production promotes antibiotic tolerance and metabolic heterogeneity in *Pseudomonas aeruginosa* biofilms. *Nat. Commun.* **10**, 762 (2019).
158. Singer, E., Wagner, M. & Woyke, T. Capturing the genetic makeup of the active microbiome *in situ*. *ISME J.* **11**, 1949–1963 (2017).
159. Hong, J.-K., Kim, S. B., Lyou, E. S. & Lee, T. K. Microbial phenomics linking the phenotype to fonction: the potential of Raman spectroscopy. *J. Microbiol.* **59**, 249–258 (2021).
160. Hatzenpichler, R., Krukenberg, V., Spietz, R. L. & Jay, Z. J. Next-generation physiology approaches to study microbiome function at single cell level. *Nat. Rev. Microbiol.* **18**, 241–256 (2020).
161. Jing, X. et al. One-cell metabolic phenotyping and sequencing of soil microbiome by Raman-activated gravity-driven encapsulation (RAGE). *mSystems* **6**, e00181–21 (2021).
162. Kim, H. S. et al. Raman spectroscopy compatible PDMS droplet microfluidic culture and analysis platform towards on-chip lipidomics. *Analyst* **142**, 1054–1060 (2017).
163. Wang, X. et al. Raman-activated droplet sorting (RADS) for label-free high-throughput screening of microalgal single-cells. *Anal. Chem.* **89**, 12569–12577 (2017).
164. Lorenz, B., Wichmann, C., Stöckel, S., Rösch, P. & Popp, J. Cultivation-free Raman spectroscopic investigations of bacteria. *Trends Microbiol.* **25**, 413–424 (2017).
165. Rösch, P. et al. Online monitoring and identification of bioaerosols. *Anal. Chem.* **78**, 2163–2170 (2006).
166. Locke, A., Fitzgerald, S. & Mahadevan-Jansen, A. Advances in optical detection of human-associated pathogenic bacteria. *Molecules* **25**, 5256 (2020).
167. Maruthamuthu, M. K., Raffiee, A. H., De Oliveira, D. M., Ardekani, A. M. & Verma, M. S. Raman spectra-based deep learning: a tool to identify microbial contamination. *Microbiologyopen* **9**, e1122 (2020).
168. de Siqueira E Oliveira, F. S. A., da Silva, A. M., Pacheco, M. T. T., Giana, H. E. & Silveira, L. Biochemical characterization of pathogenic bacterial species using Raman spectroscopy and discrimination model based on selected spectral features. *Lasers Med. Sci.* **36**, 289–302 (2021).
169. Wang, K. et al. *Arcobacter* identification and species determination using Raman spectroscopy combined with neural networks. *Appl. Environ. Microbiol.* **86**, e00924–20 (2020).
170. Yu, S., Li, H., Li, X., Fu, Y. V. & Liu, F. Classification of pathogens by Raman spectroscopy combined with generative adversarial networks. *Sci. Total. Environ.* **726**, 138477 (2020).
171. Lorenz, B., Ali, N., Bocklitz, T., Rösch, P. & Popp, J. Discrimination between pathogenic and non-pathogenic *E. coli* strains by means of Raman microspectroscopy. *Anal. Bioanal. Chem.* **412**, 8241–8247 (2020).
172. Verma, T., Annappa, H., Singh, S., Umapathy, S. & Nandi, D. Profiling antibiotic resistance in *Escherichia coli* strains displaying differential antibiotic susceptibilities using Raman spectroscopy. *J. Biophotonics* **14**, e202000231 (2021).
173. Götz, T. et al. Automated and rapid identification of multidrug resistant *Escherichia coli* against the lead drugs of acylureidopenicillins, cephalosporins, and fluoroquinolones using specific Raman marker bands. *J. Biophotonics* **13**, e202000149 (2020).
174. Kriem, L. S., Wright, K., Ccahuana-Vasquez, R. A. & Rupp, S. Confocal Raman microscopy to identify bacteria in oral subgingival biofilm models. *PLoS ONE* **15**, e0232912 (2020).
175. Kochan, K. et al. Vibrational spectroscopy as a sensitive probe for the chemistry of intra-phase bacterial growth. *Sensors* **20**, 3452 (2020).
176. Stöckel, S., Kirchhoff, J., Neugebauer, U., Rösch, P. & Popp, J. The application of Raman spectroscopy for the detection and identification of microorganisms. *J. Raman Spectrosc.* **47**, 89–109 (2016).
177. Pahlow, S. et al. Isolation and identification of bacteria by means of Raman spectroscopy. *Adv. Drug Deliv. Rev.* **89**, 105–120 (2015).
178. Qian, X. et al. *In vivo* tumor targeting and spectroscopic detection with surface-enhanced Raman nanoparticle tags. *Nat. Biotechnol.* **26**, 83–90 (2008).
179. Porter, M. D., Lipert, R. J., Siperko, L. M., Wang, G. & Narayanan, R. SERS as a bioassay platform: fundamentals, design, and applications. *Chem. Soc. Rev.* **37**, 1001–1011 (2008).
180. Yakes, B. J., Lipert, R. J., Bannantine, J. P. & Porter, M. D. Detection of *Mycobacterium avium* subsp. *paratuberculosis* by a sonicate immunoassay based on surface-enhanced Raman scattering. *Clin. Vaccine Immunol.* **15**, 227–234 (2008).
181. Wang, C., Madiyar, F., Yu, C. & Li, J. Detection of extremely low concentration waterborne pathogen using a multiplexing self-referencing SERS microfluidic biosensor. *J. Biol. Eng.* **11**, 9 (2017).
182. Catala, C. et al. Online SERS quantification of *Staphylococcus aureus* and the application to diagnostics in human fluids. *Adv. Mater. Technol.* **1**, 1600163 (2016).
183. Pazos-Perez, N. et al. Ultrasensitive multiplex optical quantification of bacteria in large samples of biofluids. *Sci. Rep.* **6**, 29014 (2016).
184. Shi, L. et al. Rapid, quantitative, high-sensitive detection of *Escherichia coli* O157:H7 by gold-shell silica-core nanospheres-based surface-enhanced Raman scattering lateral flow immunoassay. *Front. Microbiol.* **11**, 596005 (2020).
185. You, S.-M. et al. Gold nanoparticle-coated starch magnetic beads for the separation, concentration, and SERS-based detection of *E. coli* O157:H7. *ACS Appl. Mater. Interfaces* **12**, 18292–18300 (2020).
186. Hong, W.-E. et al. Assembled growth of 3D Fe_3O_4@Au nanoparticles for efficient photothermal ablation and SERS detection of microorganisms. *J. Mater. Chem. B* **6**, 5689–5697 (2018).
187. Opota, O., Croxatto, A., Prod'hom, G. & Greub, G. Blood culture-based diagnosis of bacteraemia: state of the art. *Clin. Microbiol. Infect.* **21**, 313–322 (2015).
188. Cross, K. L. et al. Targeted isolation and cultivation of uncultivated bacteria by reverse genomics. *Nat. Biotechnol.* **37**, 1314–1321 (2019).
189. Samek, O. et al. Quantitative Raman spectroscopy analysis of polyhydroxyalkanoates produced by *Cupriavidus necator* H16. *Sensors* **16**, 1808 (2016).
190. Berg, J. S., Schwedt, A., Kreutzmann, A.-C., Kuypers, M. M. M. & Milucka, J. Polysulfides as intermediates in the oxidation of sulfide to sulfate by *Beggiatoa* spp. *Appl. Environ. Microbiol.* **80**, 629–636 (2014).
191. Taylor, G. T. Windows into microbial seascapes: advances in nanoscale imaging and application to marine sciences. *Ann. Rev. Mar. Sci.* **11**, 465–490 (2019).
192. Cohen, A. B. et al. Applying fluorescence in situ hybridization to aquatic systems with cyanobacteria blooms: autofluorescence suppression and high-throughput image analysis. *Limnol. Oceanogr. Methods* **19**, 457–475 (2021).
193. Zeller, P., Ploux, O. & Méjean, A. A simple protocol for attenuating the auto-fluorescence of cyanobacteria for optimized fluorescence in situ hybridization (FISH) imaging. *J. Microbiol. Methods* **122**, 16–19 (2016).
194. Woyke, T. et al. Assembling the marine metagenome, one cell at a time. *PLoS ONE* **4**, e5299 (2009).
195. Ben-Amor, K. et al. Genetic diversity of viable, injured, and dead fecal bacteria assessed by fluorescence-activated cell sorting and 16S rRNA gene analysis. *Appl. Environ. Microbiol.* **71**, 4679–4689 (2005).
196. Hatzenpichler, R. et al. Visualizing in situ translational activity for identifying and sorting slow-growing archaeal–bacterial consortia. *Proc. Natl Acad. Sci. USA* **113**, E4069–E4078 (2016).
197. Grieb, A. et al. A pipeline for targeted metagenomics of environmental bacteria. *Microbiome* **8**, 21 (2020).
198. Gong, L., Zheng, W., Ma, Y. & Huang, Z. Higher-order coherent anti-Stokes Raman scattering microscopy realizes label-free super-resolution vibrational imaging. *Nat. Photonics* **14**, 115–122 (2020).
199. Xiong, H. et al. Super-resolution vibrational microscopy by stimulated Raman excited fluorescence. *Light. Sci. Appl.* **10**, 87 (2021).
200. Watanabe, K. et al. Structured line illumination Raman microscopy. *Nat. Commun.* **6**, 10095 (2015). **Super-resolution Raman microscopy — structured line illumination to increase the spatial resolution below the Rayleigh limit**.
201. Kögler, M., Itkonen, J., Viitala, T. & Casteleijn, M. G. Assessment of recombinant protein production in *E. coli* with time-gated surface enhanced Raman spectroscopy (TG-SERS). *Sci. Rep.* **10**, 2472 (2020).
202. Kögler, M. et al. Comparison of time-gated surface-enhanced Raman spectroscopy (TG-SERS) and classical SERS based monitoring of *Escherichia coli* cultivation samples. *Biotechnol. Prog.* **34**, 1533–1542 (2018).
203. Shkolyar, S. et al. Detecting kerogen as a biosignature using colocated UV time-gated Raman and fluorescence spectroscopy. *Astrobiology* **18**, 431–453 (2018).
204. Yu, S., Piao, X. & Park, N. Machine learning identifies scale-free properties in disordered materials. *Nat. Commun.* **11**, 4842 (2020).
205. Zhong, M., Girolami, M., Faulds, K. & Graham, D. Bayesian methods to detect dye-labelled DNA oligonucleotides in multiplexed Raman spectra. *J. R. Stat. Soc. Ser. C. Appl. Stat.* **60**, 187–206 (2011).
206. Astle, W., De Iorio, M., Richardson, S., Stephens, D. & Ebbels, T. A. Bayesian model of NMR spectra for the deconvolution and quantification of metabolites in complex biological mixtures. *J. Am. Stat. Assoc.* **107**, 1259–1271 (2012).
207. Han, N. & Ram, R. J. Bayesian modeling and computation for analyte quantification in complex mixtures using Raman spectroscopy. *Comput. Stat. Data Anal.* **143**, 106846 (2020).
208. Rubtsov, D. V. et al. Application of a Bayesian deconvolution approach for high-resolution ^{1}H NMR spectra to assessing the metabolic effects of acute phenobarbital exposure in liver tissue. *Anal. Chem.* **82**, 4479–4485 (2010).
209. Weljie, A. M., Newton, J., Mercier, P., Carlson, E. & Slupsky, C. M. Targeted pofiling: quantitative analysis of ^{1}H NMR metabolomics data. *Anal. Chem.* **78**, 4430–4442 (2006).
210. Hao, J., Astle, W., De Iorio, M. & Ebbels, T. M. D. Batman — an R package for the automated quantification of metabolites from nuclear magnetic resonance spectra using a Bayesian model. *Bioinformatics* **28**, 2088–2090 (2012).
211. Goodacre, R. Explanatory analysis of spectroscopic data using machine learning of simple, interpretable rules. *Vib. Spectrosc.* **32**, 33–45 (2003).
212. Goodacre, R. et al. Rapid identification of urinary tract infection bacteria using hyperspectral whole-organism fingerprinting and artificial neural networks. *Microbiology* **144**, 1157–1170 (1998).
213. Nims, C., Cron, B., Wetherington, M., Macalady, J. & Cosmidis, J. Low frequency Raman Spectroscopy for micro-scale and in vivo characterization of elemental sulfur in microbial samples. *Sci. Rep.* **9**, 7971 (2019).
214. Eder, S. H. K., Gigler, A. M., Hanzlik, M. & Winklhofer, M. Sub-micrometer-scale mapping of magnetite crystals and sulfur globules in magnetotactic bacteria using confocal Raman micro-spectrometry. *PLoS ONE* **9**, e107356 (2014).
215. Zhu, T.-T., Tian, L.-J., Yu, S.-S. & Yu, H.-Q. Roles of cation efflux pump in biomineralization of cadmium into quantum dots in *Escherichia coli*. *J. Hazard. Mater.* **412**, 125248 (2021).
216. Choy, C. A. et al. The vertical distribution and biological transport of marine microplastics across the epipelagic and mesopelagic water column. *Sci. Rep.* **9**, 7843 (2019).
217. Jiang, P., Zhao, S., Zhu, L. & Li, D. Microplastic-associated bacterial assemblages in the intertidal zone of the Yangtze Estuary. *Sci. Total. Environ.* **624**, 48–54 (2018).
218. Frère, L. et al. Microplastic bacterial communities in the Bay of Brest: influence of polymer type and size. *Environ. Pollut.* **242**, 614–625 (2018).
219. Brewer, P. G. et al. Development of a laser Raman spectrometer for deep-ocean science. *Deep-Sea Res. Pt. I* **51**, 739–753 (2004).

220. White, S. N. Laser Raman spectroscopy as a technique for identification of seafloor hydrothermal and cold seep minerals. *Chem. Geol.* **259**, 240–252 (2009).
221. Rull, F. et al. The Raman laser spectrometer for the ExoMars Rover Mission to Mars. *Astrobiology* **17**, 627–654 (2017).
222. NASA. NASA Mars Scanning Habitable Environments with Raman & Luminescence for Organics & Chemicals (SHERLOC). *NASA* https://mars.nasa.gov/mars2020/spacecraft/instruments/sherloc/ (2020).
223. Veneranda, M. et al. ExoMars Raman Laser Spectrometer (RLS): development of chemometric tools to classify ultramafic igneous rocks on Mars. *Sci. Rep.* **10**, 16954 (2020).
224. Veneranda, M. et al. ExoMars Raman laser spectrometer: a tool for the potential recognition of wet-target craters on Mars. *Astrobiology* **20**, 349–363 (2020).
225. Messmer, M. W., Dieser, M., Smith, H. J., Parker, A. E. & Foreman, C. M. Investigation of Raman spectroscopic signatures with multivariate statistics: an approach for cataloguing microbial biosignatures. *Astrobiology* **22**, 1–11 (2022).
226. Arnold, F. H. & Georgiou, G. *Directed Enzyme Evolution: Screening and Selection Methods* (Humana Press, 2003).
227. Markel, U. et al. Advances in ultrahigh-throughput screening for directed enzyme evolution. *Chem. Soc. Rev.* **49**, 233–262 (2020).
228. Peng, L. et al. Intracellular ethanol accumulation in yeast cells during aerobic fermentation: a Raman spectroscopic exploration. *Lett. Appl. Microbiol.* **51**, 632–638 (2010).
229. Cecchini, M. P. et al. Ultrafast surface enhanced resonance Raman scattering detection in droplet-based microfluidic systems. *Anal. Chem.* **83**, 3076–3081 (2011).
230. März, A., Henkel, T., Cialla, D., Schmitt, M. & Popp, J. Droplet formation via flow-through microdevices in Raman and surface enhanced Raman spectroscopy-concepts and applications. *Lab. Chip* **11**, 3584–3592 (2011).
231. Moore, B. D. et al. Rapid and ultra-sensitive determination of enzyme activities using surface-enhanced resonance Raman scattering. *Nat. Biotechnol.* **22**, 1133–1138 (2004).
232. Hutter, E. & Fendler, J. H. Exploitation of localized surface plasmon resonance. *Adv. Mater.* **16**, 1685–1706 (2004).
233. Pilot, R. et al. A review on surface-enhanced Raman scattering. *Biosensors* **9**, 57 (2019).
234. Cui, L., Zhang, D. D., Yang, K., Zhang, X. & Zhu, Y.-G. Perspective on surface-enhanced Raman spectroscopic investigation of microbial world. *Anal. Chem.* **91**, 15345–15354 (2019).
235. Sharma, B., Frontiera, R. R., Henry, A.-I., Ringe, E. & Van Duyne, R. P. SERS: materials, applications, and the future. *Mater. Today* **15**, 16–25 (2012).
236. Madzharova, F., Heiner, Z., Simke, J., Selve, S. & Kneipp, J. Gold nanostructures for plasmonic enhancement of hyper-Raman scattering. *J. Phys. Chem. C.* **122**, 2931–2940 (2018).
237. Wagner, M. & Haider, S. New trends in fluorescence *in situ* hybridization for identification and functional analyses of microbes. *Curr. Opin. Biotechnol.* **23**, 96–102 (2012).
238. Daims, H., Lücker, S. & Wagner, M. Daime, a novel image analysis program for microbial ecology and biofilm research. *Environ. Microbiol.* **8**, 200–213 (2006).
239. Hoshino, T., Yilmaz, L. S., Noguera, D. R., Daims, H. & Wagner, M. Quantification of target molecules needed to detect microorganisms by fluorescence in situ hybridization (FISH) and catalyzed reporter deposition-FISH. *Appl. Environ. Microbiol.* **74**, 5068–5077 (2008).
240. Amann, R., Snaidr, J., Wagner, M., Ludwig, W. & Schleifer, K. H. In situ visualization of high genetic diversity in a natural microbial community. *J. Bacteriol.* **178**, 3496–3500 (1996).
241. Lukumbuzya, M., Schmid, M., Pjevac, P. & Daims, H. A multicolor fluorescence *in situ* hybridization approach using an extended set of fluorophores to visualize microorganisms. *Front. Microbiol.* **10**, 1383 (2019).
242. Valm, A. M. et al. Systems-level analysis of microbial community organization through combinatorial labeling and spectral imaging. *Proc. Natl Acad. Sci. USA* **108**, 4152–4157 (2011).
243. Heldal, M., Norland, S. & Tumyr, O. X-ray microanalytic method for measurement of dry matter and elemental content of individual bacteria. *Appl. Environ. Microbiol.* **50**, 1251–1257 (1985).
244. Wei, L., Yu, Y., Shen, Y., Wang, M. C. & Min, W. Vibrational imaging of newly synthesized proteins in live cells by stimulated Raman scattering microscopy. *Proc. Natl Acad. Sci. USA* **110**, 11226–11231 (2013).
245. Li, J. & Cheng, J.-X. Direct visualization of de novo lipogenesis in single living cells. *Sci. Rep.* **4**, 6807 (2014).
246. Gao, C. et al. Single-cell bacterial transcription measurements reveal the importance of dimethylsulfoniopropionate (DMSP) hotspots in ocean sulfur cycling. *Nat. Commun.* **11**, 1942 (2020).
247. Kopf, S. H. et al. Heavy water and ^{15}N labelling with NanoSIMS analysis reveals growth rate-dependent metabolic heterogeneity in chemostats. *Environ. Microbiol.* **17**, 2542–2556 (2015).
248. Crespi, H. L., Conrad, S. M., Uphaus, R. A. & Katz, J. J. Cultivation of microorganisms in heavy water. *Ann. N. Y. Acad. Sci.* **84**, 648–666 (1960).
249. Kselíková, V., Vítová, M. & Bišová, K. Deuterium and its impact on living organisms. *Folia Microbiol.* **64**, 673–681 (2019).
250. Matanfack, G. A., Pistiki, A., Rösch, P. & Popp, J. Raman ^{18}O-labeling of bacteria in visible and deep UV-ranges. *J. Biophotonics* **14**, e202100013 (2021).
251. Yan, S. et al. Development overview of Raman-activated cell sorting devoted to bacterial detection at single-cell level. *Appl. Microbiol. Biotechnol.* **105**, 1315–1331 (2021).
252. Wang, Y. et al. Raman activated cell ejection for isolation of single cells. *Anal. Chem.* **85**, 10697–10701 (2013).
253. Sidore, A. M., Lan, F., Lim, S. W. & Abate, A. R. Enhanced sequencing coverage with digital droplet multiple displacement amplification. *Nucleic Acids Res.* **44**, e66 (2016).

Acknowledgements

R.S. acknowledges support from a Gordon and Betty Moore Foundation Symbiosis in Aquatic Systems Initiative Investigator Award (GBMF9197; https://doi.org/10.37807/GBMF9197), a grant from the Simons Foundation (542395) as part of the Principles of Microbial Ecosystems (PriME) Collaborative, a grant (315230_176189) from the Swiss National Science Foundation and support from the National Centre of Competence in Research (NCCR) *Microbiomes* (51NF40_180575). F.C.P. was supported by a Young Independent Research Group grant from the Austrian Science Fund (FWF; ZK-57). D.B. was supported by the Austrian Science Fund (FWF; P26127-B20 and P27831-B28), the United States Department of Energy (DE-SC0019012) and the European Research Council (ERC; Starting Grant: FunKeyGut 741623). Research in the lab of M.W. on Raman microspectroscopy and its application in microbial ecology was supported by an ERC Advanced Grant (Nitricare; 294343) and the Wittgenstein Award of the FWF (Z-383-B). W.E.H. acknowledges financial and instrumental support from EPSRC (EP/M002403/1, EP/M02833X/1) and NERC (NE/M002934/1). G.T.T. acknowledges support from NSF-MRI grant OCE-1336724 and a Gordon and Betty Moore Foundation Grant no. 5064. J.K. acknowledges funding by ERC Starting Grant 259432 Multibiophot. J.-X.C. acknowledges support from NIH (R35 GM136223 and R01AI141439). The Stocker group thanks R. Naisbit for scientific editing.

Author contributions

Introduction (R.S., K.S.L. and Z.L.); Experimentation (R.S., K.S.L., Z.L., M.W., G.T.T., J.K., M.Z. and J.-X.C.); Results (R.S., K.S.L., Z.L., M.W., W.E.H., G.T.T., J.K., M.Z. and J.-X.C.); Applications (R.S., K.S.L., Z.L., F.C.P., M.W., D.B. and J.P.); Reproducibility and data deposition (R.S., K.S.L. and Z.L.); Limitations and optimizations (R.S., K.S.L., Z.L. and G.T.T.); Outlook (R.S., K.S.L. and Z.L.); Overview of the Primer (R.S., K.S.L. and Z.L.).

Competing interests

The authors declare no competing interests.

Peer review information

Nature Reviews Methods Primers thanks C. Garcia-Timmermans, A. Locke, G. Pezzotti and the other, anonymous, reviewer(s) for their contribution to the peer review of this work.

Publisher's note

Supplementary information

The online version contains supplementary material available at https://doi.org/10.1038/s43586-021-00075-6.

RELATED LINKS

Biostudies: http://www.ebi.ac.uk/biostudies
GAMESS: https://www.msg.chem.iastate.edu/gamess/capabilities.html
Horiba Scientific: https://static.horiba.com/fileadmin/Horiba/Products/Scientific/Molecular_and_Microanalysis/ACC_SERS_Subtrate/SERS_Substrate_Raman_MM_Brochure_Fr.pdf
KnowItAll: https://sciencesolutions.wiley.com/knowitall-spectroscopy-software/
OptiFDTD: https://optiwave.com/optifdtd-overview/
ORCA: https://www.orcasoftware.de/tutorials_orca/spec/IR.html#predicting-raman-spectra
Raman processor: https://github.com/harubang2/Raman_processor
SERSitive: https://sersitive.eu/about-substrates/?gclid=Cj0KCQjw24qHBhCnARIsAPbdtlIvxejBMIy2YjTc0L7kMLgjrAc6F97lVsLj_stqb32zoPx47PUIb2QaAhjsEALw_wcB

Glossary

Fourier transform infrared (FTIR) spectroscopy

The other prominent method of vibrational spectroscopy, whereby absorption of light by a sample is used to identify the molecular composition of the sample.

Normal Raman microspectroscopy

A fundamental form of Raman microspectroscopy that relies on measurement of non-resonant, spontaneous scattering signals in which one out of ~10^6 incoming photons to a sample is scattered.

Wavenumber

A unit of frequency used in vibrational spectroscopy, defined as the frequency divided by the speed of the wave and thus equal to the number of waves within one centimetre.

Resonance Raman scattering

Raman scattering that arises when the wavelength of the incident laser beam matches the electronic transitions of a molecule, which generates much more intense Raman signals than normal Raman scattering.

Raman reporter

A chemical that generates a known surface-enhanced Raman scattering signal.

Mode-locked laser

A laser that produces ultrashort pulses on the picosecond or femtosecond scale.

Selection rules

Constraints that govern the likelihood of whether undergoing particular quantum transitions from one state to another is allowed or forbidden.

Beating frequency

Frequency difference between two electromagnetic waves that interfere constructively and destructively.

Spectral window

A spectral region of interest.

Diffraction grating

A glass plate etched with very close parallel lines that produces a spectrum from a coherent light beam by diffraction and interference of light and thus functions as a planar prism.

Chromatic aberration

Discrepancy of focus in axial and transverse directions between rays with different wavelengths after a focusing lens owing to the discordance of their refraction angles.

Galvomirrors

A pair of mirrors, each of which is integrated with a rapidly moving scanning motor, which enables enlargement of a laser beam spot to a small scanning area.

Dichroic mirror

An optical component for fluorescence microscopy by which monochromatic light for the excitation of fluorophores in a sample is separated from generated fluorescence signals.

Isotopologue

A molecule that is structurally identical yet differs from another by the presence of at least one atom that possesses a different number of neutrons.

Uniformly labelled tracer

A molecule in which all available positions for a given element are occupied by an isotopically heavy or radioactive nuclide, typically noted as [U-^{n}E]compound, where n = atomic mass, E = elemental symbol, U = uniformly, followed by chemical form.

Fractional isotopic abundance

The proportion of atoms in a molecular pool populated by the heavy isotope — also referred to as atom% (multiplied by 100).

Biomolecular fingerprint

An indicator in which chemical properties of a biomolecule are encoded; in vibrational spectroscopy, collective vibrational frequencies in wavenumber of chemical bonds within a biomolecule.

Raman-silent

The absence of Raman-active vibrational modes.

Savitzky–Golay filter

A filter algorithm that fits a polynomial of a known order to each point in the spectrum, using a sliding window of a user-defined width, subsequently replacing each point with the fitted value at the centre of the window.

Vector normalization

A normalization approach in which the intensity at each wavenumber is divided by the square root of the sum of squares of intensities for all wavenumbers within a spectral window, such that the Euclidean distance from the origin in the multidimensional space is equal to 1.

Mahalanobis distance

A measure of the distance between a point and the centroid of a multivariate normal distribution, in units of standard deviation.

Non-negative matrix factorization

A technique that represents each point in a set of mixed spectra as a weighted mixture of a finite number of conserved sub-spectra, with the axes being directly interpretable as Raman sub-spectra.

Independent component analysis

A technique that optimizes a new set of axes to naively capture covariance between variables separately for each of a finite number of independently varying subsets of data.

Isotopomers

Isotopomers of a compound have the same number of each isotope, but their positions differ.

Voigt probability distribution profile

A convolution of Gaussian and Lorentzian probability distributions that is widely used in peak-fitting routines to describe the symmetry of peaks in Raman spectroscopy.

Chromophore

A region of a molecule where the energy difference between two molecular orbitals is within the visible spectrum, thus determining the colour of the molecule.

nature portfolio

https://doi.org/10.1038/s43586-021-00075-6

Supplementary information

Raman microspectroscopy for microbiology

Supplementary Information for

Raman microspectroscopy for microbiology

Lee *et al.*

Supplementary Notes

Supplementary Table

Supplementary Notes

Supplementary Note 1: Optimization of technical components

Microscope

An upright or inverted microscope system can be employed. An upright system brings advantages for measurements of samples in still fluid setups or dry samples on substrates due to easy microscope access for the user. In contrast, an inverted system is practical for measurements in fluidic devices (e.g., microfluidics) because it leaves space for flexible handling of the setup from above, for example, for the arrangement of tubing or access for tweezers (**Supplementary Fig. 1a**).

Phase contrast or differential interference contrast (DIC) microscopy is compatible with Raman measurement, yet specific optical components for those setups such as phase rings or polarizers could reduce Raman signals, in comparison to the setup for bright-field microscopy. For example, in our experience (Lee, pers. obs.), a ~30% reduction in Raman signal intensity can arise due to the presence of a phase ring, for samples measured using a 532-nm Raman laser and a 60×, 0.95 NA objective.

For long-term time-series measurements of samples, it is possible to use commercial hardware focus modules that enable an interrogation area to be maintained in focus in the *z*-direction (e.g., perfect focus system (PFS) and TruFocus from Nikon and Olympus, respectively; CRISP from ASI may be more suitable for customized systems). As these modules depend on infrared light sources, a module that does not interfere with Raman measurement must be chosen. For instance, a unit that uses an 870-nm LED is not compatible with Raman measurement using a 785-nm laser. Alternatively, it is possible to selectively deactivate the autofocus during measurement.

Confocality

The Raman interrogation volume (i.e., confocal volume) is determined by the combination of the specifications of the objective (in particular, its magnification and numerical aperture) and the confocal setup[1] – here, we focus on a confocal pinhole (**Supplementary Fig. 1b**). Adjusting the Raman interrogation volume does not linearly change the generated Raman intensities from a sample, as lasers that are commonly used have a Gaussian-shaped intensity profile (i.e., TEM_{00}). Thus, reduction of the size of the laser spot generally results in a disproportionate concentration of the laser power and a stronger signal generated from the beam centre axis. However, there is a trade-off with the risk of laser-induced photophoretic damage to the microbial cell, as this depends on the laser power density (i.e., watts per unit area), rather than the laser power itself.

In general, the higher the power of the objective and the smaller the opening of the confocal pinhole, the greater the axial (*z*-directional) confocality (i.e., signals that arrive at the detector mostly come from the focus plane). In contrast, the dimensions of the Raman interrogation volume in lateral directions (*x*–*y* plane), directly correlate with the size of the laser spot, which mainly depends on the specifications of the objective. The higher the numerical aperture of the objective, the tighter the confinement of the laser beam. The spot size of a laser beam focused using an objective is given by $d = 1.22\lambda / \mathrm{NA}$, where λ is the wavelength of the laser and NA is the numerical aperture of the objective. For example, when a 532-nm laser is focused using a 60×, 1.2 NA objective, a laser spot with a diameter of 541 nm is expected when in focus. Spatial resolution is limited to the radius of the laser beam spot (i.e., $0.61\lambda / \mathrm{NA}$).

Calculating the interrogation volume is not straightforward, as it is also affected by the optical configuration of the microspectrometer and the wavelength of the excitation laser, although for a given experimental setup, the Raman interrogation volume can be empirically evaluated. The focus of the Raman laser can be identified using a depth profiling in the *z*-direction (it does not simply correspond to the focus of the bright-field imaging, as described in main text; see 'Experimentation – System configuration'). To choose an appropriate axial confocality, a sample is measured using a range of pinhole openings (e.g., 50–300 µm), and the opening for which the Raman signals of interest are maximised over those from the surroundings (e.g., glass substrate; see below 'Substrate') can be used for real measurements of the sample. To determine the lateral resolution, line scanning is used, by scanning across the edge of a material that generates high Raman intensity (e.g., a rectangular piece of silicon wafer). The lateral resolution can be defined by the distance at which the Raman intensity of the silicon wafer (at wavenumber 520.5 cm^{-1}) changes from 10% to 90% of the maximum[2] – in practice, the resulting value is comparable to that calculated theoretically.

Laser

The selection of laser wavelength and power has considerable impact on the success of Raman measurements. The generated Raman intensity is inversely proportional to λ^4 (where λ is the wavelength of the laser), thus a laser with a shorter wavelength brings advantages for measurement. However, this is accompanied by a greater likelihood of a fluorescence background, and also a greater risk of laser-induced photophoretic damage due to the stronger absorption of shorter wavelength light by biological samples[3–7].

To measure Raman spectra of biological samples, a laser with one of four wavelengths (blue at 488 nm; green at 532 nm; red at 660 nm; near-infrared at 785 nm) is most commonly used, and a laser with a longer wavelength (e.g., 785 nm or infrared at 1,064 nm) is used for optical trapping to minimize photophoretic damage[3,4] (**Supplementary Fig. 1c**). The 785-nm laser can be used for both Raman measurements and optical trapping[8]. As the laser exposure for Raman measurement is typically short, UV wavelengths (e.g., 350 nm) have also been used for analyses of living bacterial cells[9], although in this case, all optical components must be compatible with the use of UV wavelengths. Deep UV (~248 nm) excitation sources are also coming into use – they are well suited to interrogate specific known metabolites of microorganisms that generate resonance effects with these short wavelengths[10–13]. General guidelines for the selection of a laser are not easy to provide, but a 532-nm laser, an intermediate wavelength within the visible range that can potentially provide a good compromise between Raman and fluorescence background intensities, can be considered a versatile starting point.

The presence of resonance-inducing biomolecules within microorganisms must be taken into account. For instance, cytochrome *c* can be measured with the resonance effect using a 532-nm laser. Carotenoids, ubiquitous pigments in photoautotrophs[14] (e.g., microalgae, cyanobacteria) and some non-photoautotrophs[15], can be measured using resonance over a broad range of wavelengths (from 350 nm to 785 nm). However, to measure other compounds in these organisms, these resonance effects should be avoided as they dominate other cellular signals – the intensity of resonance Raman scattering is typically 1,000-fold greater than that of normal Raman scattering. To this end, three techniques can be employed: (i) use of laser wavelengths that do not induce the resonance effect (e.g., a 785-nm laser for measurements of cytochrome *c*-containing microbes); (ii) bleaching of those compounds using a laser before measurements[16]; and (iii) bleaching using chemicals such as hydrogen peroxide (H_2O_2)[17].

Detector

An appropriate detector must be chosen on the basis of its quantum efficiency (**Supplementary Fig. 1d**). In general, front-illuminated charge-coupled device (CCD) detectors are widely used because of their good price–performance ratio. Back-illuminated CCD detectors can measure samples with a higher sensitivity (quantum efficiency), but are generally expensive. If ultraviolet (UV) wavelengths are the spectral region of interest, a UV-coated detector can be used. Similarly, for measurements using Raman lasers with long wavelengths (e.g., 785 nm), back-illuminated deep-depletion CCD detectors provide an improved quantum efficiency in the near-infrared (NIR) region.

The spectral resolution of a Raman system is determined by the pixel size of the detector, in conjunction with the density of grooves in the grating (a key component in determining the spectral resolution; see below 'Diffraction grating'), the focal length (**FIG. 2a**), the wavelength of the Raman laser, and the size of the slit (**FIG. 2a**). A higher spectral resolution can be obtained with a smaller pixel size, a higher density of grooves, a longer wavelength, and a narrower size of the slit. In general, current detectors have pixel size between 13 µm × 13 µm and 26 µm × 26 µm. As in light microscopy, binning (combining the signal of adjacent pixels) can be used to improve the sensitivity of measurements, although this is achieved at the expense of spectral resolution.

Substrate

Even for confocal Raman microspectroscopy, in practice, Raman signals from the substrate holding the sample are of similar intensity to those from the sample, as the substrates are often better Raman scatterers than biological samples. Most relevant peaks for biological samples are located in the 700–3,400 cm^{-1} range, and the majority of substrates scatter in the lower part of this same range (**Supplementary Fig. 1e**). This interference becomes greater relative to the signal of interest for measurements of minute samples like microbes, and thus the choice of an appropriate substrate is particularly important.

Glass slides or coverslips can be used as a starting point for measurements of novel samples and, if a substrate with less background is needed, other materials can be considered. Alternatives include aluminium-coated slides for measurements of dry cells (reflecting generated signals back to the

Raman system; a silver- or gold-coated slide can also be used, enabling measurement of surface-enhanced Raman scattering) or CaF_2 or quartz slides for measurements of cells within a medium. The choice of laser wavelength enters into this decision, as the background signal from a particular substrate depends strongly on the laser wavelength. In addition, the intensity of the background can vary according to the manufacturer of the substrate, even for supposedly identical material (**Supplementary Fig. 1e**).

Diffraction grating

A grating, dividing the Raman signal according to wavelength (**Supplementary Fig. 1f**), is a key component in the determination of the spectral resolution of the measured Raman spectra. Ruled and holographic gratings are commonly used and we here focus on the use of a ruled grating because this can provide a higher efficiency, diffracting a greater proportion of light in the required direction.

The specifications of a ruled grating concern the number of grooves within a unit length (grooves per mm; $1/L$ in **Supplementary Fig. 1f**) and the blaze angle. Gratings with 300–2,400 grooves/mm are commonly used, and this parameter determines the spectral resolution. The lower the number of grooves, the lower the spectral resolution, but also the higher the throughput of the signals diffracted. For applications in microbiology and microbial ecology, very high spectral resolution is not necessary because the Raman peaks of interest are typically not sharp, unlike those of measurements in materials science. In general, a grating yielding a spectral resolution of *c.* 1.5 cm^{-1} is sufficient, thereby allowing the phenylalanine peak at 1,002–1,006 cm^{-1}, the sharpest of the peaks among biologically important compounds, to be differentiated from its nearest neighbour within a spectrum. As an additional consideration, the use of a grating with a lower spectral resolution enables more rapid measurement (due to the higher signal throughput). The blaze angle of the grating should be optimized with respect to the wavelength of the Raman laser, because it affects the efficiency of the grating. For instance, for Raman measurements using a 532-nm laser, a grating that is blazed around 532 nm (e.g., 500 nm) should be used to maximize the sensitivity (**Supplementary Fig. 1f**).

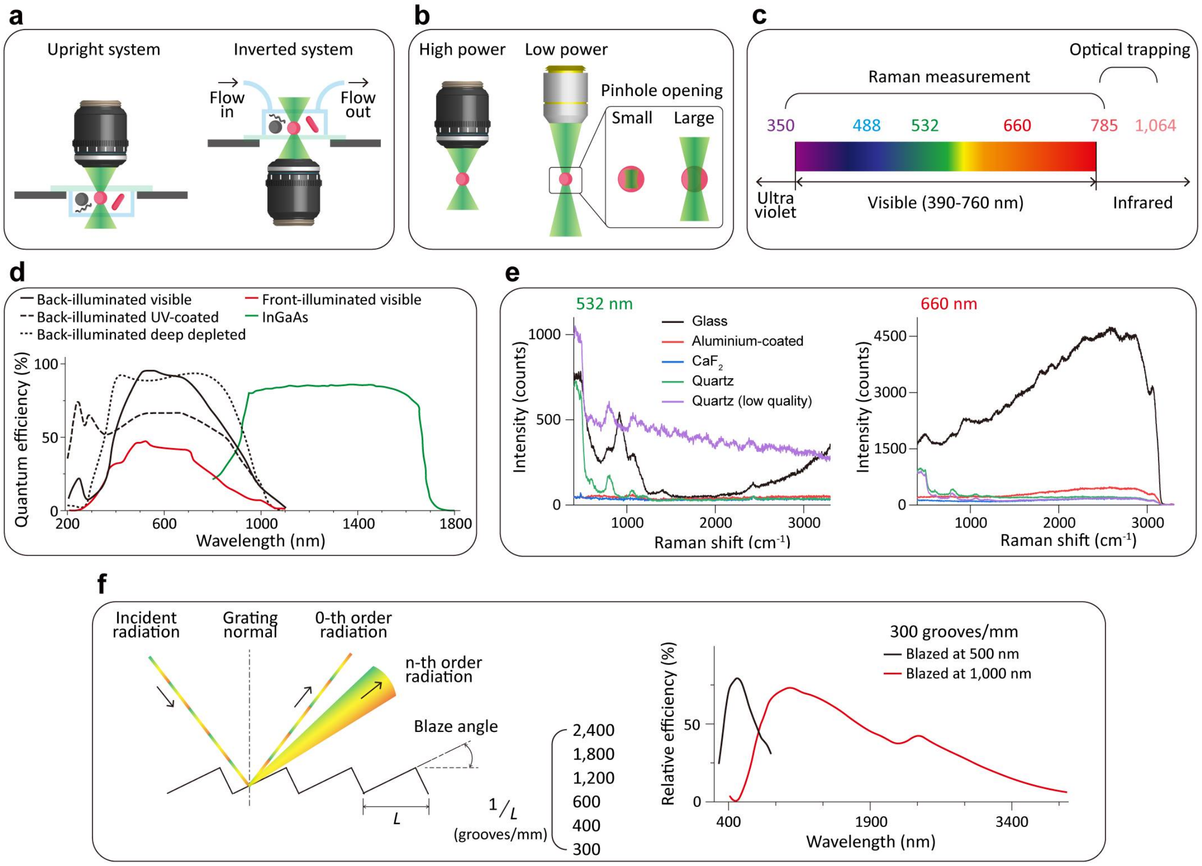

Supplementary Fig. 1 | **Optimization of technical components. a** | Microscope: in general, an upright system can be considered for measurement of dry cells, and an inverted system for samples in liquid phase. **b** | Objective and confocal pinhole: the higher the power and numerical aperture of the objective and the smaller the opening of the confocal pinhole, the greater the confocality in 3D. **c** | Laser: in general, 350–785 nm lasers are used for Raman measurements and 785–1,064 nm lasers are used for optical trapping. For the Raman measurement, an appropriate laser wavelength should be chosen considering the trade-off between the generated Raman intensities (inversely proportional to the laser wavelength to the power of four) and the likelihood of generation of fluorescence (greater with shorter laser wavelength). **d** | Detector: in general, a front-illuminated visible light CCD detector can be used, but if higher sensitivity is required, other types of detectors are available. **e** | Substrate: every substrate produces an inherent background signal that is dependent on the wavelength of the Raman laser. Glass and aluminium-coated slides can be used as a starting point for measurement of samples in liquid phase and dry cells, respectively. If less interference by the substrate is required, use of CaF$_2$ or quartz provides a potential solution. Additionally, background signals that are generated from substrates are highly influenced by the quality of the substrate (e.g., purity). **f** | Diffraction grating: a key component that determines the spectral resolution of the Raman measurement. The higher the number of grooves per mm, the higher the spectral resolution but the lower the throughput of the Raman signals diffracted. A grating that is blazed at an appropriate wavelength (e.g., blazed around 532 nm for measurement using a 532-nm laser) should be used to maximize the measurement of the generated Raman signals.

Supplementary Note 2: Isotope mass effect in stable isotope probing (SIP)–Raman

In SIP–Raman experiments, the magnitude of spectral red shifts depends on heavy and light isotope masses and to what element(s) it is bound (see **Supplementary Box 1** for mathematical explanation). For example, introduction of a single deuterium atom (^{2}H or D) will slow vibrational frequencies by ~13% when bound to a hydrogen atom and by ~27% when bound to a carbon atom (**Supplementary Fig. 2b**). The red shift's magnitude also varies inversely with elemental mass (**Supplementary Fig. 2b**).

Supplementary Box 1 | **Atomic mass effect on vibrational frequency.**

The diatomic molecular vibration is modelled as a harmonic oscillator where two masses vibrate as if joined by a spring, as illustrated in **Supplementary Fig. 2a**. Vibrational frequency of the oscillation is directly related to masses of the bound atoms in wavenumbers ($\tilde{\nu}$, cm^{-1})

$$\tilde{\nu} = \frac{1}{2\pi c}\sqrt{\frac{k}{\mu}}, \tag{1}$$

where c is speed of light (cm/sec), k is a force constant (erg/cm^2), and μ is the reduced mass (gm). The atomic partners will have reduced masses, μ_l and μ_h, in the light and heavy pairs, respectively, each is described by

$$\mu = \frac{m_1\, m_2}{m_1 + m_2}, \tag{2}$$

where, m_1 and m_2 are the masses of atoms 1 and 2 bound together. On the assumption that k is the same between the μ_l and μ_h because neutrons are uncharged and because other terms cancel out, the fractional reduction factor for frequency can be computed by

$$\frac{\tilde{\nu}_\mathrm{h}}{\tilde{\nu}_\mathrm{l}} = \sqrt{\frac{\mu_\mathrm{l}}{\mu_\mathrm{h}}}. \tag{3}$$

This reduction factor is then multiplied by $\tilde{\nu}_\mathrm{l}$ of the light isotopologue to predict red-shifted $\tilde{\nu}_\mathrm{h}$. For example, the ^{12}C–^{12}C pair has a reduced mass (μ_l) of 6.00 (12×12/(12+12)) and its symmetrical bond stretching has a $\tilde{\nu}_\mathrm{l}$ of ~1,157 cm^{-1}. If one atom is replaced with a ^{13}C, then the reduced mass becomes 6.24 (12×13/(12+13)) and hence the reduction factor ($\tilde{\nu}_\mathrm{h}/\tilde{\nu}_\mathrm{l}$) is 0.981 and the predicted red-shifted frequency ($\tilde{\nu}_\mathrm{h}$) is 1,135 cm^{-1}.

In theory, red shifts shown in **Supplementary Fig. 2b** can be resolved by a Raman microspectrophotometer capable of 1 cm^{-1} spectral resolution. However, diagnostic peaks may overlap with other bands that are often broadened by interactions among neighbouring molecules[18]. Thus discerning isotopologues can be challenging, but detectability sometimes can be improved by selecting the heaviest of multiple stable isotopes. Clearly, higher resolution diffraction gratings available on a dispersive spectrophotometer should be used to detect red shifts, e.g., 1,200 or 1,800 grooves/mm.

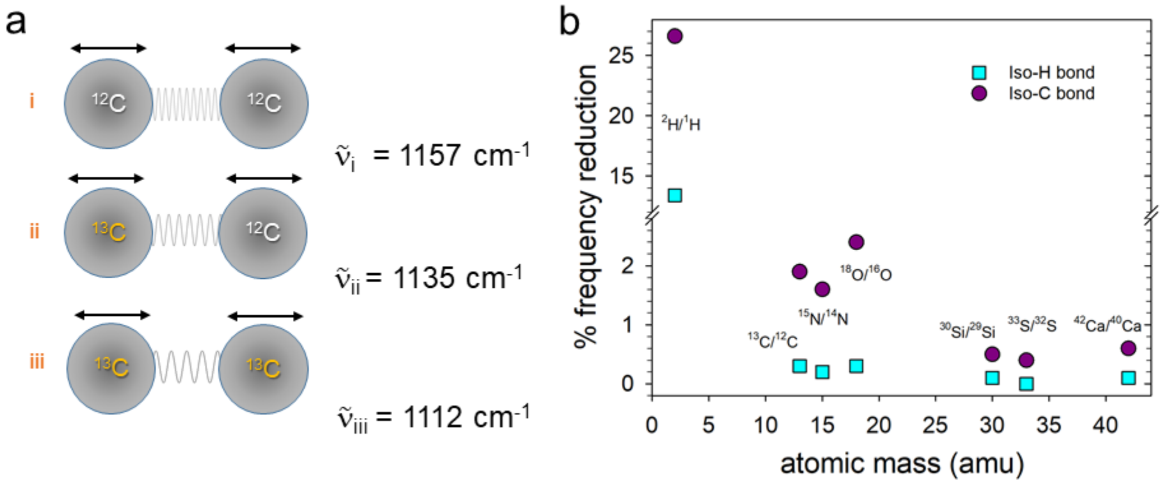

Supplementary Fig. 2 | **The neutron factor.** Effects of isotopic substitutions on molecular vibrational frequencies (*f*) and consequently on Raman wavenumbers ($\tilde{\nu}$). **a** | Diatomic harmonic oscillator model of the mass effect on symmetrical bond stretching frequencies. **b** | Mass effect on the magnitude of isotope-induced red shifts on isotopes bound to either light hydrogen (□) or light carbon (○) atoms, expressed as % reduction in *f* or $\tilde{\nu}$ from the light isotopologue. In all but ^{18}O and ^{42}Ca, a single additional neutron accounts for the vibrational deceleration.

Supplementary Table

Supplementary Table 1 | **Assignment of Raman peaks to common cell constituents.** Raman peaks for substances that commonly accompany measurements of biological samples (e.g., water and substrates where the sample is placed for measurement) are also listed. Care should be taken when matching measured data with peaks in this table, as the peaks of the molecules may overlap with others.

Biomolecules/substance	**Wavenumber (cm^{-1})**	**Reference**
Cholesterols	430; 548; 608; 700; 742; 960; 1,176; 1,438; 1,672	19
Fatty acids	1,100; 1,262; 1,438; 1,655; 2,850; 2,935	20
Starch	478; 866; 940; 1,083; 1,127; 1,340; 1,459; 2,911	21
Lipids	1,050–1,200; 1,250–1,300; 1,400–1,500; 2,800–3,000	22
DNA	540; 728; 785; 1,092; 1,480; 1,575; 1,660	23–25
RNA	580; 724; 784; 886; 1,092; 1,254; 1,326; 1,408; 1,560; 1,606; 1,686	19
Protein	1,257; 1,340; 1,453; 1,660	26
Amino acids	Various	19,25,27
Bicarbonate	683; 1,043; 1,266	*
Carotenoids	960–1,005; 1,100–1,250; 1,500–1,535	28–31
Ca-dipicolinic acid (CaDPA)	662; 824; 1,017; 1,395; 1,572	32,33
Chlorophyll	733–773; 900–986; 1,173–1,186; 1,325–1,371; 1,437–1,445; 1,554–1,640	29
Collagen	760–770; 818; 856; 928–938; 1,246; 1,440–1,452; 1,666–1,670	19
Cytochrome *c*	750; 1,128; 1,311; 1,583	34–36
polyhydroxybutyrate (PHB)	840; 1,055; 1,453; 1,725	34,37,38
Glycogen	480; 850; 940; 1,046; 1,082; 1,123; 1,260; 1,335; 1,380; 1,460	19,34
Glucose	406; 543; 775; 843; 915; 1,022; 1,074; 1,121; 1,151; 1,271; 1,348; 1,460; 2,879; 2,892; 2,948; 2,962	25,*
Lignin	Various	39
phenylalanine	486; 622; 1,003; 1,032; 1,206; 1,586; 1,606	19,25
Polyphosphate	700; 1,178	34,40
Polysulfide	152; 218; 473	41
Proteorhodopsins	1,530	42
Riboflavin	1,225; 1,346; 1,401; 1,463; 1,534	25
Triacylglycerol	1,066; 1,080; 1,125; 1,264; 1,203; 1,441; 1,656; 1,746; 2,851; 2,889	43
Water	1,665; 2,100; 3,400	**
Glass	442; 800; 920; 1,066; 1,400; 2,430	**
Quartz	474; 595; 800; 1,066; 1,200; 2,430	**
CaF_2	474; 1,030; 2,430	**

*Huang, pers. obs.

**Lee, pers. obs.

Supplementary References

1. De Grauw, C. J., Sijtsema, N. M., Otto, C. & Greve, J. Axial resolution of confocal raman microscopes: Gaussian beam theory and practice. *J. Microsc.* **188**, 273–279 (1997).
2. Jasco - Application Note Booklet. https://www.jasco.hu/wp-content/uploads/2012/11/JASCO_Raman_ApplBook.pdf.
3. Neuman, K. C., Chadd, E. H., Liou, G. F., Bergman, K. & Block, S. M. Characterization of photodamage to *Escherichia coli* in optical traps. *Biophys. J.* **77**, 2856–2863 (1999).
4. Pilát, Z. *et al.* Optical trapping of microalgae at 735-1064 nm: photodamage assessment. *J. Photochem. Photobiol. B Biol.* **121**, 27–31 (2013).
5. Yuan, X. *et al.* Effect of laser irradiation on cell function and its implications in Raman spectroscopy. *Appl. Environ. Microbiol.* **84**, e02508-17 (2018).
6. Fu, Y., Wang, H., Shi, R. & Cheng, J.-X. Characterization of photodamage in coherent anti-Stokes Raman scattering microscopy. *Opt. Express* **14**, 3942–3951 (2006).
7. Schreiber, U. & Klughammer, C. Wavelength-dependent photodamage to *Chlorella* investigated with a new type of multi-color PAM chlorophyll fluorometer. *Photosynth. Res.* **114**, 165–177 (2013).
8. Xie, C., Dinno, M. A. & Li, Y. Near-infrared Raman spectroscopy of single optically trapped biological cells. *Opt. Lett.* **27**, 249–251 (2002).
9. Nelson, W. H., Manoharan, R. & Sperry, J. F. UV resonance Raman studies of bacteria. *Appl. Spectrosc. Rev.* **27**, 67–124 (1992).
10. Sapers, H. M. *et al.* The cell and the sum of its parts: patterns of complexity in biosignatures as revealed by deep UV Raman spectroscopy. *Front. Microbiol.* **10**, 679 (2019).
11. Manoharan, R. *et al.* UV resonance Raman spectra of bacteria, bacterial spores, protoplasts and calcium dipicolinate. *J. Microbiol. Methods* **11**, 1–15 (1990).
12. Žukovskaja, O. *et al.* UV-Raman spectroscopic identification of fungal spores important for respiratory diseases. *Anal. Chem.* **90**, 8912–8918 (2018).
13. Jarvis, R. M. & Goodacre, R. Ultra-violet resonance Raman spectroscopy for the rapid discrimination of urinary tract infection bacteria. *FEMS Microbiol. Lett.* **232**, 127–132 (2004).
14. Frank, H. A. & Cogdell, R. J. Carotenoids in photosynthesis. *Photochem. Photobiol.* **63**, 257–264 (1996).
15. Takano, H. The regulatory mechanism underlying light-inducible production of carotenoids in nonphototrophic bacteria. *Biosci. Biotechnol. Biochem.* **80**, 1264–1273 (2016).
16. Huang, W. E. *et al.* Raman-FISH: combining stable-isotope Raman spectroscopy and fluorescence in situ hybridization for the single cell analysis of identity and function. *Environ. Microbiol.* **9**, 1878–1889 (2007).
17. Yakubovskaya, E., Zaliznyak, T., Martínez Martínez, J. & Taylor, G. T. Tear down the fluorescent curtain: a new fluorescence suppression method for Raman microspectroscopic analyses. *Sci. Rep.* **9**, 15785 (2019).
18. Howard, A. A., Tschumper, G. S. & Hammer, N. I. Effects of hydrogen bonding on vibrational normal modes of pyrimidine. *J. Phys. Chem. A* **114**, 6803–6810 (2010).
19. Cals, F. L. J. *et al.* Raman spectroscopic analysis of the molecular composition of oral cavity squamous cell carcinoma and healthy tongue tissue. *Analyst* **143**, 4090–4102 (2018).
20. Jamieson, L. E., Li, A., Faulds, K. & Graham, D. Ratiometric analysis using Raman spectroscopy as a powerful predictor of structural properties of fatty acids. *R. Soc. Open Sci.* **5**, 181483 (2018).
21. Ji, Y. *et al.* Raman spectroscopy provides a rapid, non-invasive method for quantitation of starch in live, unicellular microalgae. *Biotechnol. J.* **9**, 1512–1518 (2014).
22. Czamara, K. *et al.* Raman spectroscopy of lipids: a review. *J. Raman Spectrosc.* **46**, 4–20 (2015).
23. Deng, H., Bloomfield, V. A., Benevides, J. M. & Thomas, G. J. Dependence of the raman signature of genomic B-DNA on nucleotide base sequence. *Biopolymers* **50**, 656–666 (1999).
24. Mojzeš, P. *et al.* Guanine, a high-capacity and rapid-turnover nitrogen reserve in microalgal cells. *Proc. Natl. Acad. Sci. U. S. A.* **117**, 32722–32730 (2020).
25. De Gelder, J., De Gussem, K., Vandenabeele, P. & Moens, L. Reference database of Raman spectra of biological molecules. *J. Raman Spectrosc.* **38**, 1133–1147 (2007).

26. Chan, J. W. *et al.* Monitoring dynamic protein expression in living E. coli. Bacterial cells by laser tweezers Raman spectroscopy. *Cytom. Part A* **71**, 468–474 (2007).
27. Overman, S. A. & Thomas, G. J. Raman markers of nonaromatic side chains in an α-helix assembly: Ala, Asp, Glu, Gly, Ile, Leu, Lys, Ser, and Val residues of phage fd subunits. *Biochemistry* **38**, 4018–4027 (1999).
28. Chao, H.-J. *et al.* HipH catalyzes the hydroxylation of 4-hydroxyisophthalate to protocatechuate in 2,4-xylenol catabolism by *Pseudomonas* putida NCIMB 9866. *Appl. Environ. Microbiol.* **82**, 724–731 (2016).
29. Jehlička, J., Edwards, H. G. M. & Oren, A. Raman spectroscopy of microbial pigments. *Appl. Environ. Microbiol.* **80**, 3286–3295 (2014).
30. Li, M. *et al.* Rapid resonance Raman microspectroscopy to probe carbon dioxide fixation by single cells in microbial communities. *ISME J.* **6**, 875–885 (2012).
31. Robert, B. Resonance Raman spectroscopy. *Photosynth. Res.* **101**, 147–155 (2009).
32. Rösch, P. *et al.* Chemotaxonomic identification of single bacteria by micro-Raman spectroscopy: application to clean-room-relevant biological contaminations. *Appl. Environ. Microbiol.* **71**, 1626–1637 (2005).
33. Kong, L. *et al.* Characterization of bacterial spore germination using phase-contrast and fluorescence microscopy, Raman spectroscopy and optical tweezers. *Nat. Protoc.* **6**, 625–639 (2011).
34. Xu, J., Webb, I., Poole, P. & Huang, W. E. Label-free discrimination of rhizobial bacteroids and mutants by single-cell Raman microspectroscopy. *Anal. Chem.* **89**, 6336–6340 (2017).
35. Ng, C. K. *et al.* Elevated intracellular cyclic-di-GMP level in Shewanella oneidensis increases expression of *c*-type cytochromes. *Microb. Biotechnol.* **13**, 1904–1916 (2020).
36. Pätzold, R. *et al.* In situ mapping of nitrifiers and anammox bacteria in microbial aggregates by means of confocal resonance Raman microscopy. *J. Microbiol. Methods* **72**, 241–248 (2008).
37. Hermelink, A., Brauer, A., Lasch, P. & Naumann, D. Phenotypic heterogeneity within microbial populations at the single-cell level investigated by confocal Raman microspectroscopy. *Analyst* **134**, 1149–1153 (2009).
38. Majed, N. & Gu, A. Z. Application of Raman microscopy for simultaneous and quantitative evaluation of multiple intracellular polymers dynamics functionally relevant to enhanced biological phosphorus removal processes. *Environ. Sci. Technol.* **44**, 8601–8608 (2010).
39. Larsen, K. L. & Barsberg, S. Theoretical and Raman spectroscopic studies of phenolic lignin model monomers. *J. Phys. Chem. B* **114**, 8009–8021 (2010).
40. Majed, N., Matthäus, C., Diem, M. & Gu, A. Z. Evaluation of intracellular polyphosphate dynamics in enhanced biological phosphorus removal process using Raman microscopy. *Environ. Sci. Technol.* **43**, 5436–5442 (2009).
41. Berg, J. S., Schwedt, A., Kreutzmann, A.-C., Kuypers, M. M. M. & Milucka, J. Polysulfides as intermediates in the oxidation of sulfide to sulfate by *Beggiatoa* spp. *Appl. Environ. Microbiol.* **80**, 629–636 (2014).
42. Song, Y. *et al.* Proteorhodopsin overproduction enhances the long-term viability of *Escherichia coli*. **86**, e02087-19 (2020).
43. Wang, T. *et al.* Quantitative dynamics of triacylglycerol accumulation in microalgae populations at single-cell resolution revealed by Raman microspectroscopy. *Biotechnol. Biofuels* **7**, 58 (2014).